

F. W. Klaiber, R. A. Lohnes, L. W. Zachary, T. A. Austin,
B. T. Havens, B. T. McCurnin

Design Methodology for Corrugated Metal Pipe Tiedowns: Phase I

February 1993

Sponsored by the
Iowa Department of Transportation and the
Iowa Highway Research Board



**Iowa Department
of Transportation**

Iowa DOT Project HR-332
ISU-ERI-Ames-93409

report

**College of
Engineering
Iowa State University**

F. W. Klaiber, R. A. Lohnes, L. W. Zachary, T. A. Austin,
B. T. Havens, B. T. McCurnin

Design Methodology for Corrugated Metal Pipe Tiedowns: Phase I

Sponsored by the
Iowa Department of Transportation and the
Iowa Highway Research Board

Iowa DOT Project HR-332
ISU-ERI-Ames-93409



**engineering
research institute**
iowa state university

The opinions, findings, and conclusions expressed in this publication are those of the authors and not necessarily those of the Highway Division of the Iowa Department of Transportation.

ABSTRACT

Questionnaires were sent to transportation agencies in all 50 states in the U.S., to Puerto Rico, and all provinces in Canada asking about their experiences with uplift problems of corrugated metal pipe (CMP). Responses were received from 52 agencies who reported 9 failures within the last 5 years. Some agencies also provided design standards for tiedowns to resist uplift. There was a wide variety in restraining forces used; for example for a pipe 6 feet in diameter, the resisting force ranged from 10 kips to 66 kips. These responses verified the earlier conclusion based on responses from Iowa county engineers that a potential uplift danger exists when end restraint is not provided for CMP and that existing designs have an unclear theoretical or experimental basis.

In an effort to develop more rational design standards, the longitudinal stiffness of three CMP ranging from 4 to 8 feet in diameter were measured in the laboratory. Because only three tests were conducted, a theoretical model to evaluate the stiffness of pipes of a variety of gages and corrugation geometries was also developed. The experimental results indicated a "stiffness" EI in the range of 9.11×10^5 k-in² to 34.43×10^5 k-in² for the three pipes with the larger diameter pipes having greater stiffness. The theoretical model developed conservatively estimates these stiffnesses.

Recognizing that soil over and around CMP's will contribute to their stiffness, one field test was conducted on a pipe 10

feet in diameter. The test was conducted with 2 feet of soil cover and a foreslope of 2:1. This test indicated that the soil cover significantly increased the stiffness of the pipe.

Future plans include development of a finite element analysis to better describe the soil structure interaction. With those relationships and the data from additional field tests, design standards based on a rational design procedure will be developed. The soil-structure analysis and the development of design standards for CMP tiedowns will comprise the final phase of this study.

TABLE OF CONTENTS

| | <u>Page</u> |
|----------------------------------------------------------------------|-------------|
| LIST OF TABLES | ix |
| LIST OF FIGURES | xi |
| 1. THE PROBLEM AND OBJECTIVES | 1 |
| 1.1 The Problem | 1 |
| 1.2 Objectives | 1 |
| 2. LITERATURE REVIEW | 3 |
| 2.1 Types of CMP | 3 |
| 2.2 Potential Failure Modes | 3 |
| 2.3 Design Methods for CMP Subjected to Soil Loads | 6 |
| 2.4 Numerical Analysis Methods for CMP-Soil Interaction | 9 |
| 2.5 Laboratory Testing | 10 |
| 2.6 Field Testing | 11 |
| 2.7 Large Span CMP Considerations | 12 |
| 2.8 Generalizations of Literature Cited | 12 |
| 3. SURVEY OF TRANSPORTATION AGENCIES ON CMP TIEDOWNS | 15 |
| 3.1 Overview | 15 |
| 3.2 Summary of Uplift Problems | 15 |
| 3.3 Types of End Restraints | 16 |
| 3.4 Force Comparison of Various Restraints | 19 |
| 3.5 Conclusions from Survey of Agencies | 22 |
| 4. TESTING | 23 |
| 4.1 Overview of Testing Program | 23 |
| 4.2 Test Frame | 23 |

| | <u>Page</u> |
|---------------------------------------------------------------------|-------------|
| 4.3 CMP Diaphragms | 34 |
| 4.4 Test Loading | 34 |
| 4.5 Test Instrumentation | 35 |
| 4.6 Uniaxial Tensile Tests | 48 |
| 5. EXPERIMENTAL RESULTS | 49 |
| 5.1 Scope of Reported Results | 49 |
| 5.2 Moment vs. Vertical Deflection | 53 |
| 5.3 Moment vs. Corrugation Strain | 62 |
| 5.4 Uniaxial Tensile Test Results | 62 |
| 5.5 Ratios of Hoop Strain to Longitudinal Strain | 68 |
| 6. THEORY FOR GENERAL APPLICATION TO OTHER LARGE CMP | 71 |
| 6.1 Longitudinal Moment Capacity | 71 |
| 6.2 Longitudinal Ultimate Moment Capacity | 80 |
| 6.3 Theoretical CMP EI Factor | 91 |
| 6.4 Large Deflection Considerations | 104 |
| 6.5 Diameter Change Effects | 104 |
| 6.6 Helix Angle Effects | 108 |
| 6.7 Comparison of Experimental and Theoretical Results | 109 |
| 7. FIELD TEST | 113 |
| 7.1 Objective | 113 |
| 7.2 Description of Test Specimen | 113 |
| 7.3 Excavation and Bedding Preparation | 113 |
| 7.4 Placing Pipe Sections | 115 |

| | <u>Page</u> |
|---------------------------------------------------------------------------|-------------|
| 7.5 Instrumentation | 117 |
| 7.6 Load Frame Description | 120 |
| 7.7 Backfilling | 124 |
| 7.8 Backfill Data | 127 |
| 7.9 Backfill Results | 130 |
| 7.10 Uplift Data | 140 |
| 7.11 Uplift Results | 141 |
| 7.12 Method of Analysis | 155 |
| 8. CONCLUSIONS | 157 |
| 9. RECOMMENDED RESEARCH | 161 |
| 10. ACKNOWLEDGMENTS | 163 |
| 11. REFERENCES | 165 |
| Appendix A: Method to Account for Non-Uniform Loading of CMP | 169 |

LIST OF TABLES

| | <u>Page</u> |
|----------------------------------------------------------------------------------------------------------------------------|-------------|
| Table 3.1 Summary of CMP uplift problems | 16 |
| Table 4.1 Flexural test specimens and instrumentation | 24 |
| Table 4.2 Test loading - ISU1SL | 36 |
| Table 4.3 Test loading - ISU1F | 37 |
| Table 4.4 Test loading - ISU2SL | 38 |
| Table 4.5 Test loading - ISU2F | 38 |
| Table 4.6 Test loading - ISU3SL | 39 |
| Table 4.7 Test loading - ISU3F | 40 |
| Table 5.1 Summary of flexural test results | 57 |
| Table 5.2 Tensile test results | 67 |
| Table 5.3 Yield stress values calculated from yield strain measurements | 69 |
| Table 5.4 Ratios of measured hoop strains to measured longitudinal strains | 69 |
| Table 6.1 Numerical values K_1 for 3x1 CMP | 77 |
| Table 6.2 Numerical values of K_6 for 3x1 CMP | 101 |
| Table 6.3 Comparison of yield moment values: theoretical vs. experimental | 110 |
| Table 6.4 Comparison of ultimate moment values (assuming $\theta_{ep}=90$ degrees): theoretical vs. experimental | 111 |
| Table 6.5 Comparison of EI factor values: theoretical vs. experimental | 112 |

LIST OF FIGURES

| | <u>Page</u> |
|------------------------------------------------------------------------------------------------------------------------------|-------------|
| Fig. 2.1 Potential failure modes | 4 |
| Fig. 3.1 Types of headwalls described by agencies responding to survey | 17 |
| Fig. 3.2 Relationship (linear) between resisting force and pipe diameter according to various standards | 20 |
| Fig. 3.3 Relationship (exponential) between resisting force and pipe diameter according to various standards | 21 |
| Fig. 4.1 Plan view of load frame | 26 |
| Fig. 4.2 End view of typical load frame | 27 |
| Fig. 4.3 Side view of typical load frame | 28 |
| Fig. 4.4 Photograph of load frame with ISU1 being tested | 29 |
| Fig. 4.5 CMP rotational restraint | 30 |
| Fig. 4.6 CMP longitudinal restraint | 31 |
| Fig. 4.7 CMP diaphragm details | 32 |
| Fig. 4.8 Sand loading on CMP | 33 |
| Fig. 4.9 Typical location of strain gages at mid-span | 42 |
| Fig. 4.10 Typical location of strain gages at quarter-spans | 43 |
| Fig. 4.11 Installation of DCDT's at CMP mid-span | 44 |
| Fig. 4.12 Interior view of diaphragm form and rod used to measure relative wall movement | 46 |
| Fig. 4.13 Dial gages to measure CMP deflection due to cable elongations | 47 |
| Fig. 5.1 CMP element subjected to the highest stress . . . | 51 |
| Fig. 5.2 Idealized corrugation collapse | 52 |

| | <u>Page</u> |
|---------------------------------------------------------------------------|-------------|
| Fig. 5.3 Moment vs. mid-span deflection (ISU1) | 54 |
| Fig. 5.4 Moment vs. mid-span deflection (ISU2) | 54 |
| Fig. 5.5 Moment vs. mid-span deflection (ISU3) | 55 |
| Fig. 5.6 ISU1 after collapse | 59 |
| Fig. 5.7 ISU2 after collapse | 59 |
| Fig. 5.8 ISU3 after collapse | 60 |
| Fig. 5.9 Locations of corrugation collapse | 61 |
| Fig. 5.10 Moment vs. strain (ISU1) | 63 |
| Fig. 5.11 Moment vs. strain (ISU2) | 64 |
| Fig. 5.12 Moment vs. strain (ISU3) | 65 |
| Fig. 5.13 Corrugation reference points | 66 |
| Fig. 6.1 CMP moment capacity assumptions | 72 |
| Fig. 6.2 Definitions of the tangent point ratio (R_{tp}) | 74 |
| Fig. 6.3 CMP cross-section views | 79 |
| Fig. 6.4 CMP plastic-hinge assumptions | 81 |
| Fig. 6.5 Assumed distribution of hoop stress | 85 |
| Fig. 6.6 CMP cross-section views | 86 |
| Fig. 6.7 FBD of linear segment from 1/4 corrugation style | 89 |
| Fig. 6.8 Comparison between smooth-wall pipe and CMP | 92 |
| Fig. 6.9 EI factor assumptions | 95 |
| Fig. 6.10 EI factor assumptions | 96 |
| Fig. 6.11 1/4 cycle length of CMP | 99 |

| | <u>Page</u> |
|---------------------------------------------------------------------------------------------------------|-------------|
| Fig. 6.12 Corrugation pitch decrease as measured by DCDT#1 (DCDT is shown in Figure 4.11b) | 105 |
| Fig. 6.13 Moment vs. CMP diameter increase | 106 |
| Fig. 6.14 Moment vs. CMP diameter decrease | 107 |
| Fig. 7.1 Longitudinal profile of test specimen | 114 |
| Fig. 7.2 Excavation-bedding preparation (Class "C") | 116 |
| Fig. 7.3 Joint Details | 118 |
| Fig. 7.4 Placement of strain gages | 119 |
| Fig. 7.5 Instrumentation to measure diameter changes | 121 |
| Fig. 7.6 Soil pressure cell locations | 122 |
| Fig. 7.7 Vertical deflection rods | 123 |
| Fig. 7.8 Load frame description | 125 |
| Fig. 7.9 Backfill details: cross section | 128 |
| Fig. 7.10 Backfill details: longitudinal | 129 |
| Fig. 7.11 Stages of backfill where instrumentation readings were taken | 131 |
| Fig. 7.12 Cross sectional deformations during backfilling | 132 |
| Fig. 7.13 Backfill strain data: Section 3 | 135 |
| Fig. 7.14 Backfill strain data | 136 |
| Fig. 7.15 Backfill soil pressure cell data | 139 |
| Fig. 7.16 Uplift - loading sequence | 143 |
| Fig. 7.17 Vertical deflections along top of pipe during uplift test | 144 |
| Fig. 7.18 Uplift strain data: Section 3 | 146 |
| Fig. 7.19 Uplift strain data: Sections 1 and 4 | 147 |

| | <u>Page</u> |
|---------------------------------------------------------------------------------------------|-------------|
| Fig. 7.20 Pressures developed within soil during uplift test: Sections A and B | 149 |
| Fig. 7.21 Pressure developed within soil during uplift test: Section C | 151 |
| Fig. 7.22 Pressures developed within soil above CMP during uplift test | 152 |
| Fig. 7.23 Cross sectional deformations during uplift test | 154 |
| Fig. A.1 Assumptions used to model CMP deflected shape under load | 172 |
| Fig. A.2 CMP filled partially with water. | 178 |
| Fig. A.3 Shear diagram for CMP specimens. | 180 |

1. THE PROBLEM AND OBJECTIVES

1.1. The Problem

In the mid 1970's Iowa Department of Transportation (Iowa DOT) and Federal Highway Administration (FHWA) recognized that corrugated metal pipe (CMP) were experiencing an unsuitable number of uplift failures. Iowa DOT and FHWA recommended that, for pipes over 4 ft in diameter, provision should be made for tiedowns at inlets. In spite of these warnings, uplift failures continued to occur; and in 1988, a survey of Iowa county engineers revealed 12% of the 68 counties that responded experienced uplift failures of CMP (Austin et al, 1990). Although this frequency of failure is down from the 16% reported in a 1975 Iowa DOT survey, the number of failures still is unacceptably high.

1.2. Objectives

The goal of this research is to develop a rational method for the design of tiedowns for CMP and to provide standard designs. Because of the formidable scope of this project, the study is divided into two phases with specific objectives in each phase. The objectives of Phase 1 are: a) synthesize design standards from state DOTs around the nation, b) determine longitudinal stiffness of corrugated metal pipe and c) begin to obtain experimental data on soil-CMP interaction. This report addresses the objectives of Phase 1.

The objectives of Phase 2 are: a) Complete collection of data on soil-structure interaction, b) incorporate the water depth computations of Austin et al (1990) into an integrated

program, c) synthesize all of the data into a rational design procedure and develop software for use on microcomputers and d) develop design standards for corrugated metal pipe tiedowns. These objectives will be addressed at a later date.

2. LITERATURE REVIEW

2.1. Types of CMP

Different methods used to fabricate CMP result in four types of pipe. Helical pipes with mechanical seams are corrugated sheets joined with a continuous interlocking helical seam. Helical, welded-seam CMP is similar to helical lock-seam except that the pipe is welded continuously along the helical seam as it is fabricated. Annular pipes with spot-welded seams consist of curved corrugated plates spot-welded to form rings two feet in length. These rings are joined by spot-welds to create CMP of practical lengths. Annular, riveted seam pipes are similar to annular spot-welded except that rivets are used as fasteners instead of welds.

2.2. Potential Failure Modes

There are many possible failure modes for CMP. They are discussed in detail by Watkins (1960) and Kennedy and Laba (1989) and are summarized here:

- 1) Excessive deflection happens if the foundation soil is highly compressible or the side fill has not been properly compacted as shown in Figure 2.1a.

- 2) Yielding of the wall section occurs when the soil has considerable passive resistance and the CMP wall thickness is insufficient to resist the superimposed loads. This is shown in Figure 2.1b.

- 3) Rather than yield in compression, the pipe wall may buckle under high load with inadequate passive resistance from



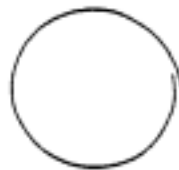
(a) excessive deflection



(b) yielding of the wall section



(c) elastic ring buckling



(d) seam failure

Figure 2.1 Potential failure modes.

the soil. See Figure 2.1c.

4) Seam failure includes shear of bolts, rivets, or welds at seams and occurs if the pipe is adequate to carry the loads but the fasteners are either substandard or spaced incorrectly. This is illustrated in Figure 2.1d.

5) Corrosion may create holes which prevent the CMP from remaining watertight.

Longitudinal flexural failure is often overlooked in design and may be as important as consideration of CMP ring bending failure. Possible causes of longitudinal bending, and thus the potential for failure include: pore water uplift below the pipe, differential settlement beneath the pipe, non-uniform bedding support beneath the pipe, frost heave, expansive soils, and earthquakes.

Several uplift failures which were most likely caused by pore water uplift under structural plate culverts are documented by Edgerton (1960) and Austin et al. (1990).

Watkins (1960) discusses the relationship of longitudinal bending stresses which act perpendicular to ring bending stresses in the corrugations. High longitudinal stresses are avoided by the relative compressibility of the corrugations as compared with smooth wall pipe; therefore, biaxial interaction is considered insignificant and longitudinal bending of CMP is analyzed separately from ring bending.

Trautmann et al (1985) employed laboratory test results on scale models to determine the longitudinal force displacement

relationships for the models subjected to vertical ground movement. Kennedy and Laba (1989) discuss lifting of the invert which may be caused by soil settlement under the CMP haunches or from increased water level under the steel structure which creates an uplift on the bottom plates. Moser (1990) quantifies the moment induced in pipes due to settlement and attempts to relate it to deflection of the pipe cross section.

Mayberry and Goodman (1989) discuss a new method of structural plate pipe installation which attempts to minimize the effects of longitudinal bending. The plates are manufactured with yielding seams which are designed to slip during bending and to minimize any potential longitudinal stresses.

Bakht (book in progress) discusses cross-sectional uplift failure of the inlet due to settlement under the haunches and longitudinal uplift failure of the entire pipe end due to bending moments induced by longitudinal settlement and buoyancy effects.

No information was found in the open literature describing methods to estimate the longitudinal strength and stiffness of CMP.

2.3. Design Methods for CMP Subjected to Soil Loads

An equation for estimating the soil load on underground conduits was developed at Iowa State University (Marston, 1930) and as applied to positive projecting conduits (Spangler, 1951)

is:

$$V = \gamma B_c^2 \frac{e^{K\mu'(H/B_c)} - 1}{2K\mu'} \quad (1)$$

where:

V = load per longitudinal length of pipe
H = height of fill above conduit
 γ = unit weight of embankment soil
K = Rankine's lateral pressure ratio
 μ' = coefficient of friction of fill material
 B_c = outside width of conduit
e = base of natural logarithms

Spangler (1941) extended Marston's work by developing a method to relate the vertical load on the CMP to the horizontal and vertical deflections. This equation, based on a deflection criterion rather than a strength criterion, follows:

$$\Delta X = D_1 \frac{KVr^3}{EI + 0.061E'R^3} \quad (2)$$

where:

ΔX = horizontal deflection of CMP (approximately equal to the vertical deflection)
K = bedding constant
V = vertical load per length of pipe
r = nominal pipe radius
E = modulus of elasticity of pipe steel
I = moment of inertia per unit length of cross section of pipe wall
E' = modulus of soil reaction
 D_1 = deflection lag factor

The deflection lag factor varies from 1 to 2 and is intended to account for yielding of soil on the sides of the CMP which may occur after maximum vertical load has been exerted on the CMP.

Because reverse curvature at the top of the CMP often occurs when vertical deflections exceed 20% of the original vertical diameter (American Iron and Steel Institute, 1967), a factor of safety (FOS) of 4 is applied to this method to limit the deflection to 5% vertically.

White and Layer (1960) describe a design procedure based on the ring compression strength of the pipe wall. This method assumes that the entire prism of soil above the pipe is supported by the walls of the pipe. The relationship is shown as follows:

$$C = P \times \frac{S}{2} \quad (3)$$

where: C = ring compression, lb/ft
 P = soil pressure on top of the pipe, lb/ft²
 S = span or diameter of pipe, ft

In this method, a FOS of 4 is used to limit the compressive stress in the pipe walls to a hydrostatic soil pressure which is equivalent to the overburden pressure divided by the FOS. No deflection criterion is used.

The ring buckling phenomenon as it pertains to the pipe-soil system has been studied by many researchers (Luscher, 1966; Chelapati and Allgood, 1972; Abdel-Sayed, 1978). A typical buckling

formula developed for CMP is:

$$p^* = 1.73 \sqrt{\frac{EI B M_s}{r^3}} \quad (4)$$

where:

- p^* = uniform applied pressure causing elastic buckling
- EI = ring bending stiffness of CMP
- B = coefficient of elastic support
- M_s = constrained modulus of soil
- r = nominal radius of tube

Krizek, et al. (1971) found that many of the design methods based on elastic buckling provide similar results except under high fills.

Circumferential loads on the CMP itself are probably highest during the handling and installation process. At that time, the CMP has no support from the lateral resistance of the soil and must depend entirely on the ring bending strength until the CMP is in place, back-filled, and the backfill compacted. With the passage of time, soil arching increases and the vertical load on the pipe decreases. Lefebvre et al. (1976) measured arching effects in an embankment over a large span CMP and concluded that 12 days after construction, the pressure on the pipe was only 25% of the calculated overburden pressure.

2.4. Numerical Analysis Methods for CMP-Soil Interaction

CANDE (Culvert analysis and design) is a finite element computer program developed specifically for the analysis of CMP and soil interaction (Katona et al., 1976). CANDE incorporates

Duncan's constitutive soil model (Duncan et al., 1980). Although advances have been made using finite element modelling for design of CMP installations, the accuracy of modelling is limited primarily by the variations of soil strength and stiffness. Poulos (1974) uses finite difference methods to estimate deflections associated with longitudinal bending.

2.5. Laboratory testing

Laboratory tests of CMP have been conducted by loading pipes to ring failure while attempting to replicate in-situ soil-structure interaction. This includes work done by Meyerhof and Baikie (1963) to evaluate the strength of corrugated sheets under circumferential load which are supported laterally by compacted sand. From these tests, the soil stiffness limit is quantified thus making it possible to determine if the CMP wall will fail by yielding or by elastic buckling. The results of these tests can be combined with the ring compression theory and various buckling theories to form a comprehensive design process.

McVay and Papadopoulos (1986) tested scaled-down pipe-arch models within a soil-filled plexiglass box and measured pore pressures in the back-fill and deflection of the model under loads. Watkins and Spangler (1958) investigated the modulus of passive resistance of the soil and its effect on CMP deflections using similitude techniques. Similitude was also used as a tool to study the effects of loads on underground structures by Young and Murphy (1964) and by Nielson and Statish (1972) and Nielson (1972) to study the soil-culvert system.

Testing to determine CMP longitudinal stiffness was conducted at Ohio State University (Lane, 1965) on 23 specimens including helical lock-seam, annular riveted, and annular spot welded. These tests included pipes up to 3 feet maximum in diameter.

2.6. Field Testing

Full-scale field testing of CMP under soil loads has been performed on a variety of CMP products starting with the tests of Marston and his associates in the 1930's. Those tests validated the theory described in Section 2.3. More recently, Watkins and Moser (1971) describe a testing procedure where loads on the pipes in an embankment are simulated by hydraulic rams which exert a downward force from load beams above the pipe. In other studies, loads on the pipes are exerted by heavily weighted test vehicles with high axle loads (Valentine, 1964; Kay and Flint, 1982; Potter and Ulery, 1989).

Special design considerations are needed for CMP under high fills. This has been studied by Spannagel, et al. (1974) and by Brown, et al. (1968) where various CMP were instrumented and monitored to better understand the effects of large loads on CMP.

Another common field condition arises when culverts under minimum cover (1 to 2 feet in some cases) are not adequately protected from high surface loads. Duncan (1978) analyzed minimum cover situations using finite element analyses to develop a "soil-culvert interaction method" for culvert design. Ahlvin (1960) studied the effects of minimum cover on a small diameter

pipe which was covered with 16 inches of material. Loads on the pipe were created by a vehicle which simulated the axle loads of large aircraft.

2.7. Large Span CMP Considerations

Large diameter CMP require special considerations because of the difficulty in determining the stress distributions around these structures (Selig, 1974). Instrumentation, monitoring, and analysis of these larger structures is detailed by several researchers (Selig et al., 1979; Duncan, 1979; McVay and Selig, 1982; Kay and Flint, 1982).

Longitudinal pipe attachments known as "compaction wings" and "thrust beams" are designed to minimize problems during the pipe installation. These problems may include (Selig et al., 1978): inadequate compaction of soil against the CMP side walls, peaking of the CMP crown and distortion of the shape during backfilling, buckling of the structure from loads imposed by construction equipment, and flattening of the CMP as fill is placed above the crown.

Studies have been conducted to determine the feasibility of using steel-reinforced earth (Kennedy et al., 1988; Kennedy and Laba, 1989) where the reinforcement is placed in horizontal layers throughout the embankment and tied to the pipe to provide support to the CMP.

2.8 Generalizations of Literature Cited

Although considerable attention has been given to the ring strength of CMP and to forces associated with overburden

pressures and live loads, very few studies have addressed longitudinal stiffness and uplift forces. More specifically, only the analytical work of Poulos (1974), the model studies of Trautmann et al (1985), and the laboratory testing of Lane (1965) provide some insight into the longitudinal response of CMP.

3. SURVEY OF TRANSPORTATION AGENCIES ON CMP TIEDOWNS

3.1 Overview

In order to synthesize design standards for corrugated metal pipe (CMP) culvert inlet restraints used by various transportation agencies, Iowa DOT and ISU sent questionnaires to each of the 50 states, Washington D.C., Puerto Rico and eight provinces of Canada, requesting information on the use of restraints and any uplift problems that may have been encountered in the last five years. The data reported here do not include data for Iowa which are presented elsewhere (Austin et al, 1990).

Fifty two (87%) of 60 agencies responded to the questionnaires. Of those responding, nine agencies report uplift problems in the past five years, and 26 of the 52 regions incorporate some type of an uplift restraint. Eighteen of those 26 agencies developed the restraints in response to earlier problems and twenty-two agencies provided copies of their design standards for end restraints for this survey.

3.2 Summary of Uplift Problems

In lieu of specifically identifying the various transportation authorities that responded, the agencies are identified by number. Table 3.1. summarizes data from seven of the reported uplift problems in some cases incomplete data were available and are indicated by "nd" in the table. Two agencies that experienced uplift problems provided no specific data on the nature of their problems. In all cases, except for Agency 1, the pipes were circular with diameters ranging from 36 to 114 inches.

For the agencies who reported soil cover depths, the cover ranged from 5 to 10 feet with the deepest cover of 10 feet over the largest diameter pipe of 114 inches reported by Agency 6. All problematic pipes were square ended except for Agency 1 with a CMP that had a step beveled inlet and Agency 6 with a beveled inlet on their CMP. In all cases, the damaged pipes were replaced with new CMP and in most situations end restraint was added.

Table 3.1. Summary of CMP Uplift Problems.

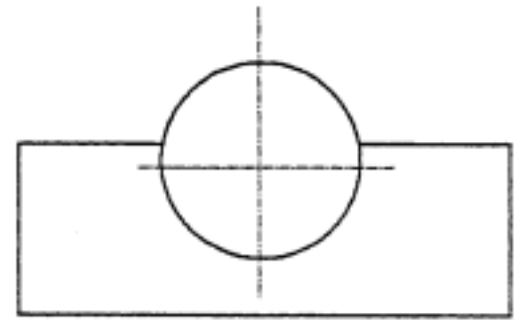
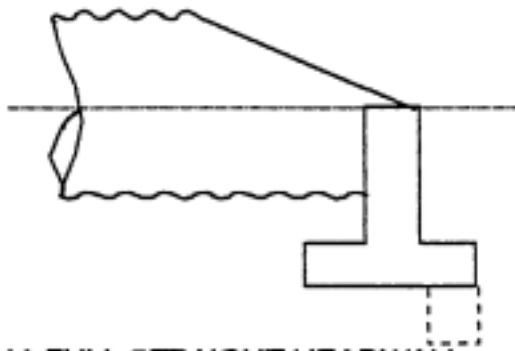
| Agency | Diameter or span/rise (in.) | Length (ft) | Skew (deg) | Cover depth (ft) |
|--------|--------------------------------|----------------|---------------|---------------------|
| 1 | 180/108 | nd | nd | nd |
| 2 | 72 | nd | 90 | 5 |
| | 96 | nd | 90 | 8 |
| 3 | 60 | 52 | nd | nd |
| 4 | 36 | 40 | 10 | "very little" |
| 5 | 60 | nd | nd | 5 |
| 6 | 114 | 164 | 30 | 10 |
| 7 | 96 | 90 | 0 | 6 |

3.3. Types of End Restraints

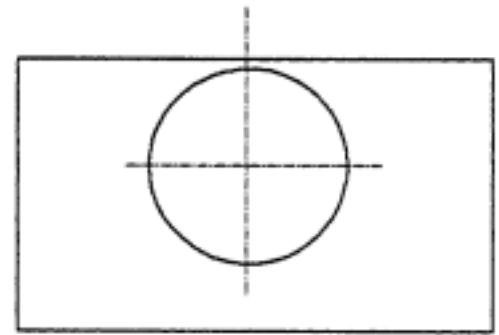
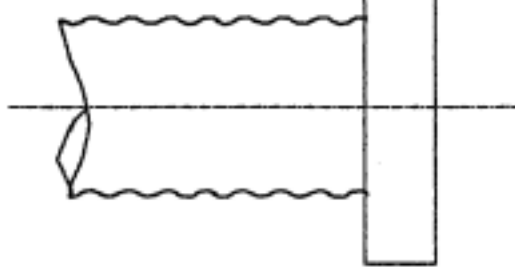
The variety of end restraints can be classified as anchors, head walls, wing walls, and slope collars. Figure 3.1 shows schematic drawings of each type.

Anchors consist of vertical concrete walls, perpendicular to the axis of the pipe, that extend to mid height of the culvert, and are bolted to the pipe with a large mass of concrete below ground. The pipe ends are beveled above the top of the concrete. In some situations, cutoff walls extend below the concrete anchors.

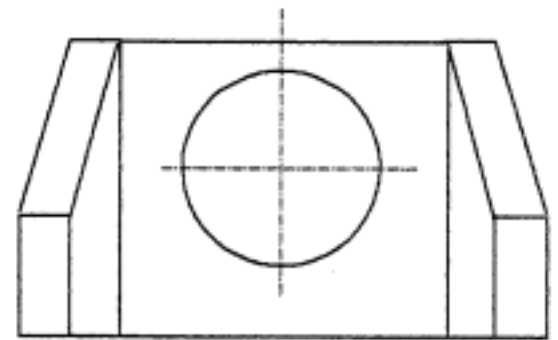
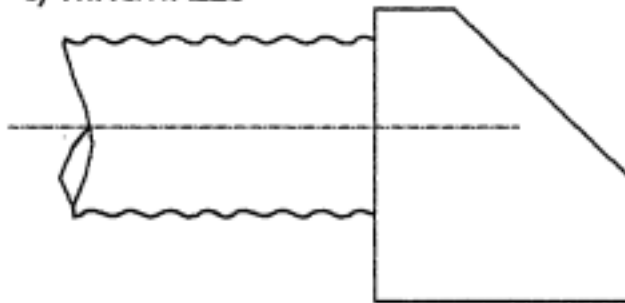
a) ANCHOR



b) FULL STRAIGHT HEADWALL



c) WINGWALLS



d) SLOPE COLLAR

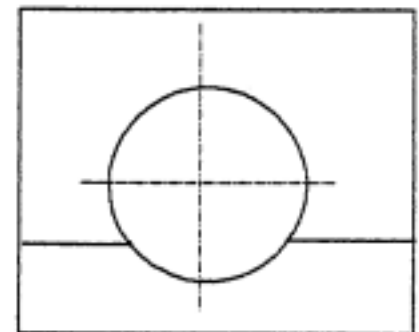
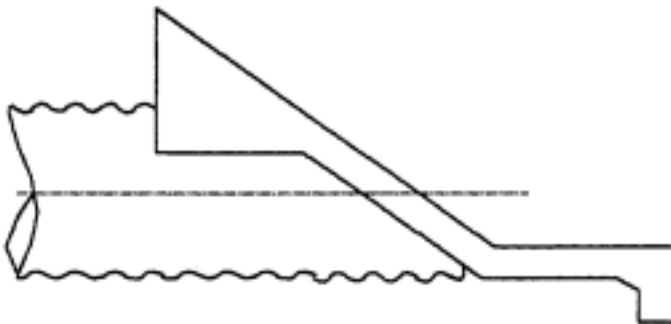


Figure 3.1 Types of headwalls described by agencies responding to survey.

Head walls are vertical concrete walls, perpendicular to the axis of the pipe, that extend above the top of square ended pipe.

Wing walls are similar to head walls but incorporate vertical walls on both sides at an angle to the to the axis of the pipes. The angled wing walls serve to direct flow into the pipe, avoid erosion or piping adjacent to the inlet, and add mass to resist uplift.

Slope collars may be either concrete or metal. The collars surround the culvert inlet, perpendicular to the pipe axis, and are parallel to soil slope of the embankment above the culvert.

Three agencies avoid the uplift problem by not using CMP and six others limit the maximum diameter of CMP. The maximum diameters range from 54 to 84 inches.

Anchor walls are used by 8 agencies, headwalls by 6, wing walls by 4, concrete slope collars by 5, and metal slope collars by 3. One agency uses anchor walls for CMP less than 48 inches in diameter and either slope collars or wing walls for pipe larger than 48 inches in diameter. A northern agency uses anchor walls on pipes 12 to 54 inches in diameter with the latter as the maximum diameter they will use. An agency from eastern United States uses wing walls on CMP between 36 and 72 inches diameter and headwalls on pipes 48 inches in diameter. The maximum diameter CMP that the eastern state uses is 72 inches. One north-central agency uses a system of longitudinal stiffeners.

3.4. Force Comparison of Various Restraints

In order to compare the various restraints, for each standard, the resisting force of the restraint was computed for a range of pipe diameters and with a constant cover depth of 2 feet. When the data are compared, it is apparent that the relationships between the resisting forces and pipe diameters can be classified as either linear or exponential shaped curves. The following graphs, Figs. 3.2 and 3.3, show the relationship between resisting force and pipe diameter according to various standards. In all cases but one, the end of the curve represents the maximum diameter CMP that the agency recommends. Also shown is the relationship resulting from the rational analysis of Austin et al (1990).

All of the agencies with standards having a linear relationship between force and diameter, shown in Fig 3.2, have standards that result in much lower forces than those calculated by Austin et al (1990). Agency 2 with the lowest forces in its standards is also the only one which had an uplift failure when restraint was used.

Agencies with standards that have an exponential relationship between resisting force and pipe diameter are shown in Fig. 3.3. Although the exponential curve of Austin et al (1990) was acknowledged to be extremely conservative; only one agency, with an exponential relationship between pipe diameter and resisting force, has standards with lower forces. The other three agencies have standards with resisting forces that are

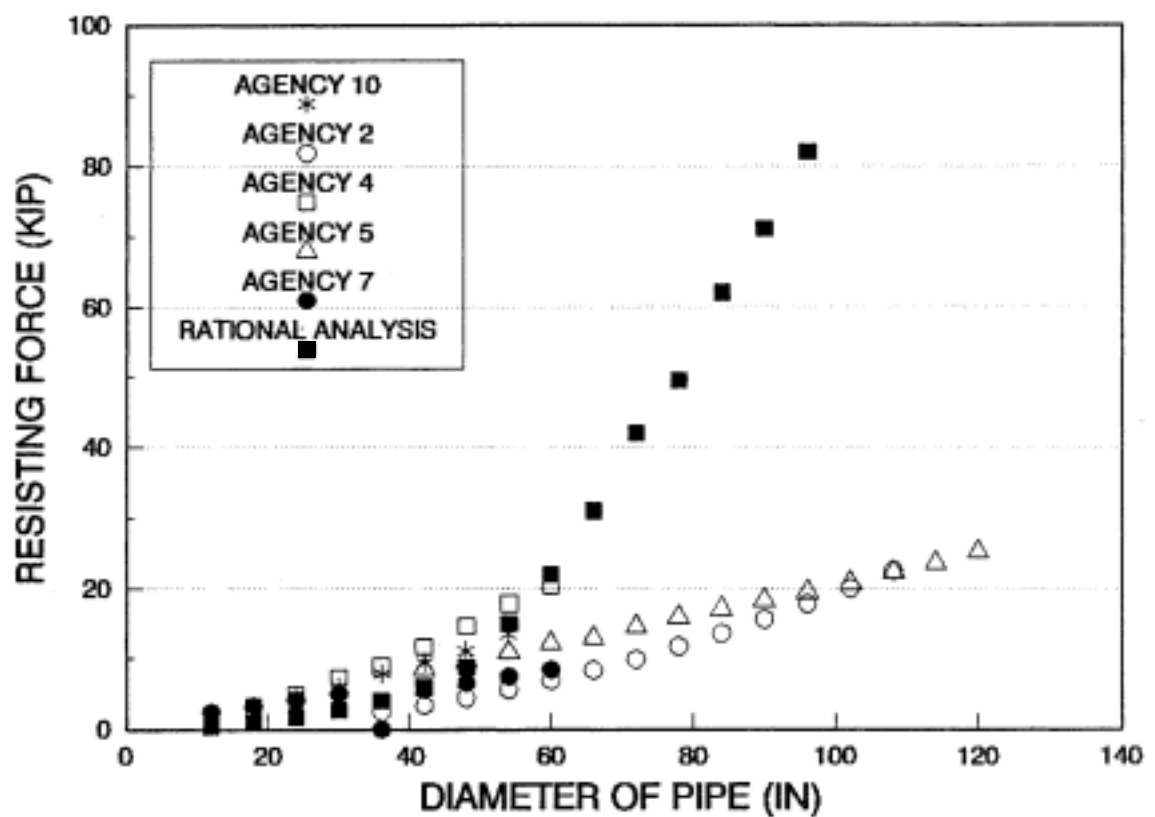


Figure 3.2 Relationship (Linear) between resisting force and pipe diameter according to various standards.

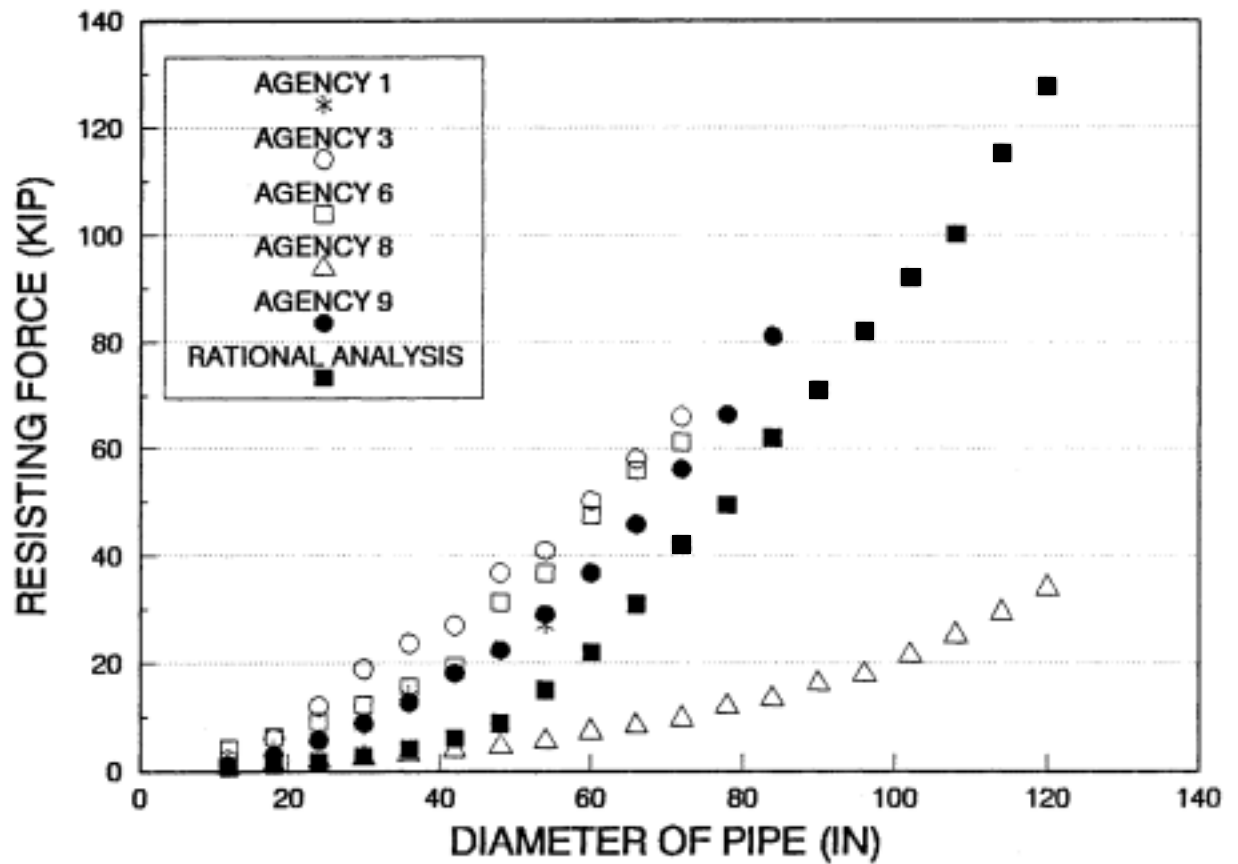


Figure 3.3 Relationship (Exponential) between resisting force and pipe diameter according to various standards.

equal or exceed those of Austin et al.

3.5 Conclusions from Survey of Agencies

In general, uplift failures of CMP throughout North America and Puerto Rico are fairly rare with only 17% of the agencies reporting failures within the last five years. Of those reporting failures, only one agency had used end restraint standards. Twenty six of 52 agencies have standards and three other agencies do not use CMP. Of those agencies that provided data to compare end restraint force as a function of CMP diameter, five have lower resisting forces than those computed by Austin et al (1990) and three have forces approximately equal or slightly greater. The large range in these standards and the continuation of uplift failures suggest that experimental work including the determination of pipe longitudinal stiffness and soil-pipe interaction is appropriate to develop a rational set of standards for end restraint.

4. TESTING

4.1. Overview of Testing Program

Because no longitudinal stiffness data for large diameter CMP are available in the literature, a program of flexural tests on larger diameter CMP was initiated. Three specimens, 4 feet, 6 feet, and 8 feet in diameter, were selected for testing. The specimens are identified as ISU1, ISU2, and ISU3 respectively and are described in Table 4.1.

4.2. Test Frame

In order to test each CMP in flexure, specimens were simply supported and distributed loads were applied in increments. As shown in plan view in Figure 4.1, independent frames support each end of the test specimen. A side view, an end view, and photograph of the test set-up are shown in Figures 4.2, 4.3, and 4.4, respectively.

Wire rope of 5/8 inch diameter suspended between columns of the frames provided end support for the CMP. The wire rope support permitted testing of CMP up to 9.5 feet in diameter with no modifications and allowed end rotation of the CMP. The CMP deflections were corrected for wire rope elongation.

The test frame was designed to resist the loads associated with the testing of the largest test specimen. The geometry of the wire ropes under load was determined so that rope tensions and corresponding loads on the frame could be calculated for each test specimen. The test frame was designed with sufficient stiffness to minimize column movements and limit rotation in the

Table 4.1 Flexural test specimens and instrumentation.

| Parameter | Specimen | | |
|------------------------------------------------------|-----------------------|---------------------|---------------------|
| | ISU1 | ISU2 | ISU3 |
| Diameter (in.) | 48 | 72 | 96 |
| Corrugation style | 3 x 1 | 3 x 1 | 3 x 1 |
| Fabrication style | Helical welded seam | Helical welded seam | Helical welded seam |
| Nominal length (ft) | 20 | 25 | 24 |
| Effective length (in.) | 236.5 | 293.5 | 286.0 |
| Gage | 12 | 14 | 14 |
| Nominal uncoated thickness (in.) | 0.1046 | 0.0747 | 0.0747 |
| Weight (lb/ft) | 50 | 75 | 100 |
| Dial gage @ free end (Fig. 4.13) | Yes | No | No |
| Dial gage @ horizontally restrained end (Fig. 4.13) | Yes | Yes | Yes |
| DCDT's around circumference @ mid-span (Fig. 4.11) | Yes | Yes | Yes |
| Mid-span strains on compression side (Fig. 4.9) | Yes | Yes | Yes |
| Mid-span strains on tension side (Fig. 4.9) | Yes | Yes | Yes |
| Quarter-span strains on compression side (Fig. 4.10) | Yes | Yes | Yes |
| Quarter-span strains on tension side (Fig. 4.10) | DCDT (no strain gage) | Yes | Yes |

Table 4.1 Continued.

| Parameter | ISU1 | ISU2 | ISU3 |
|-------------------------------------------------------|------|------|------------------------------------------|
| Mid-span horizontal deflection (Fig. 4.12) | Yes | Yes | Yes-SL ¹ No-F ² |
| Mid-span vertical deflection (top) (Fig. A.1) | Yes | Yes | Yes |
| Mid-span vertical deflection (bottom) (Fig. A.1) | Yes | Yes | Yes |
| Quarter-span vertical deflections (bottom) (Fig. A.1) | Yes | Yes | Yes |

¹ service load test² failure test

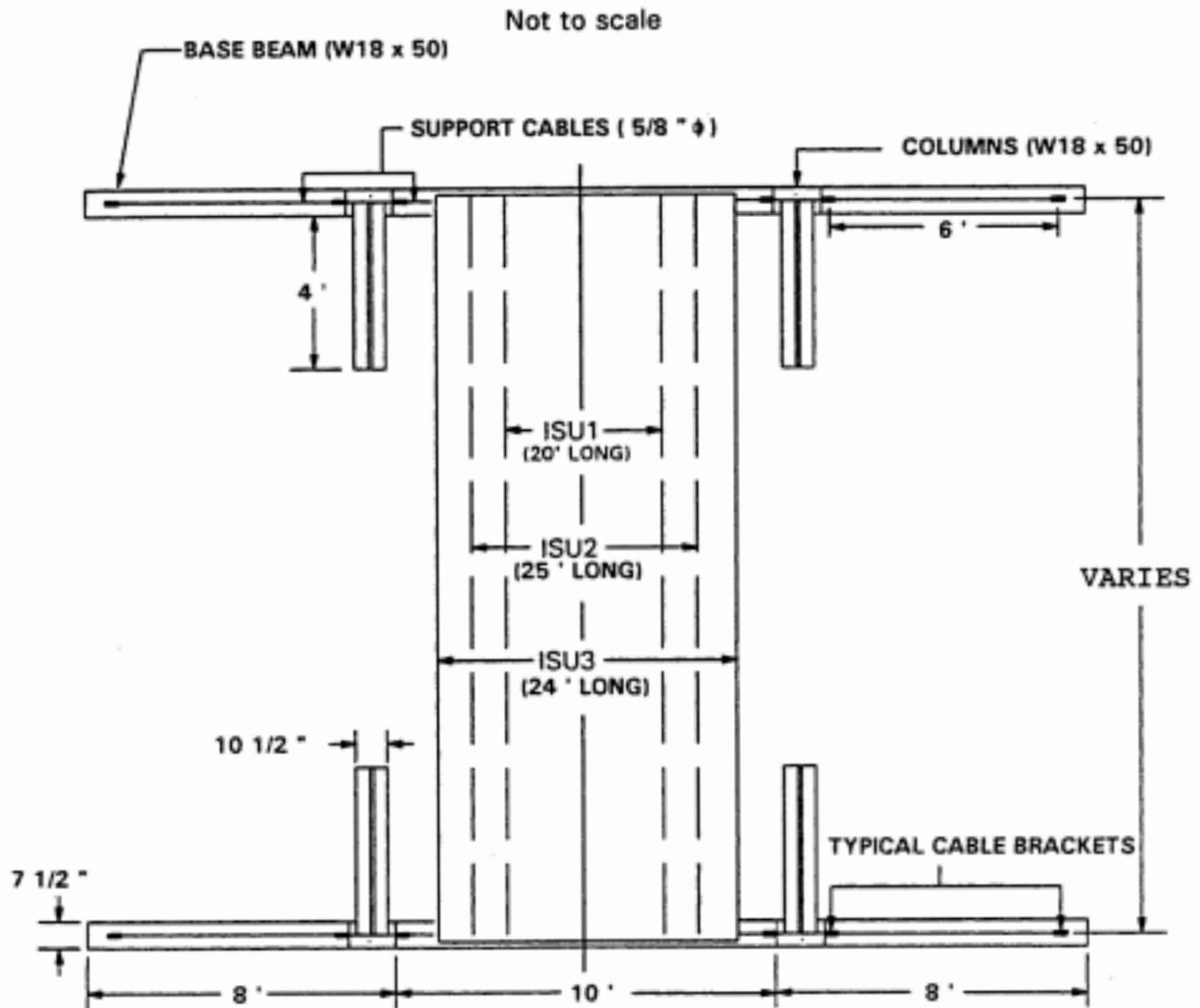


Figure 4.1 Plan view of load frames.

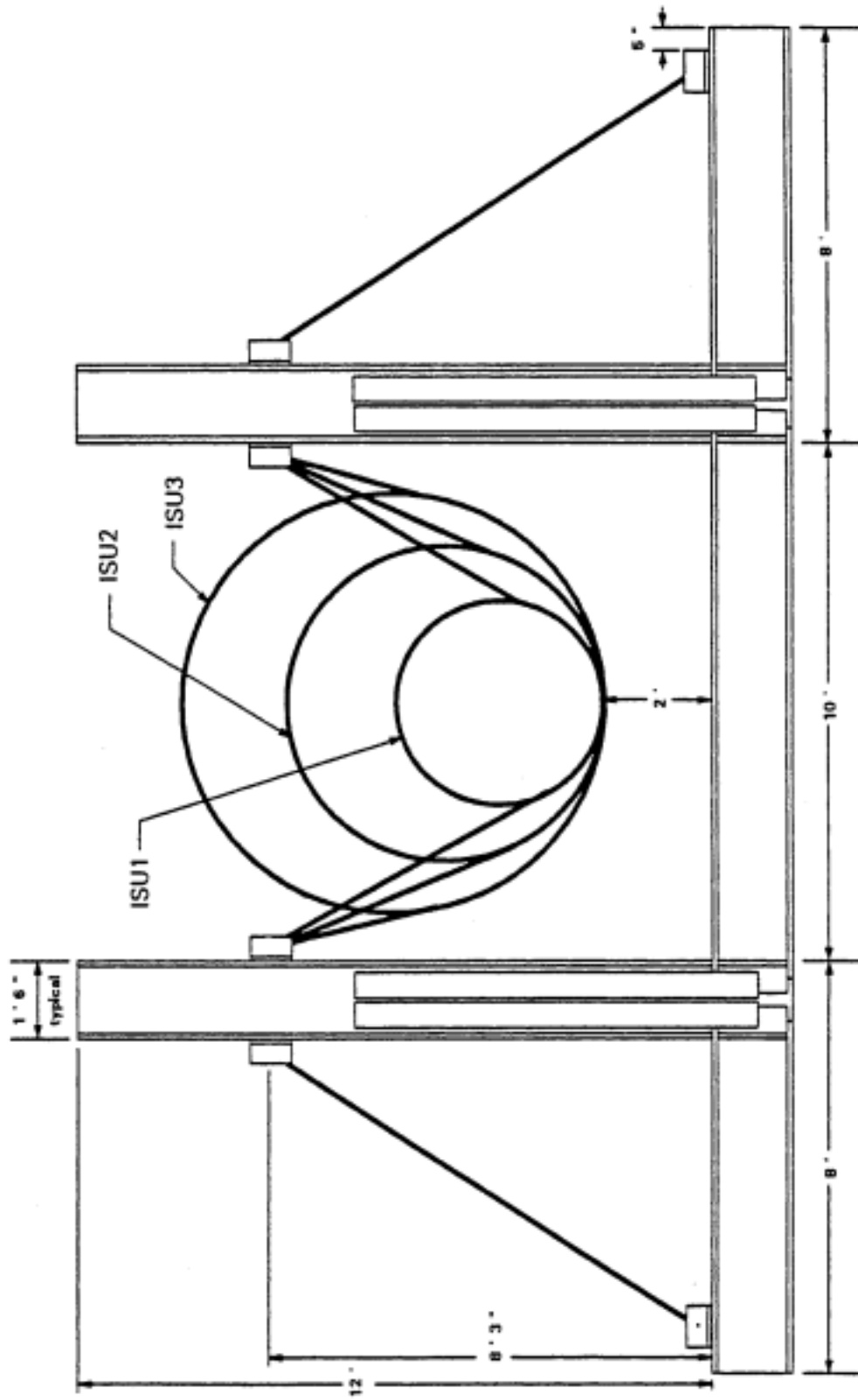


Figure 4.2 End view of typical load frame.

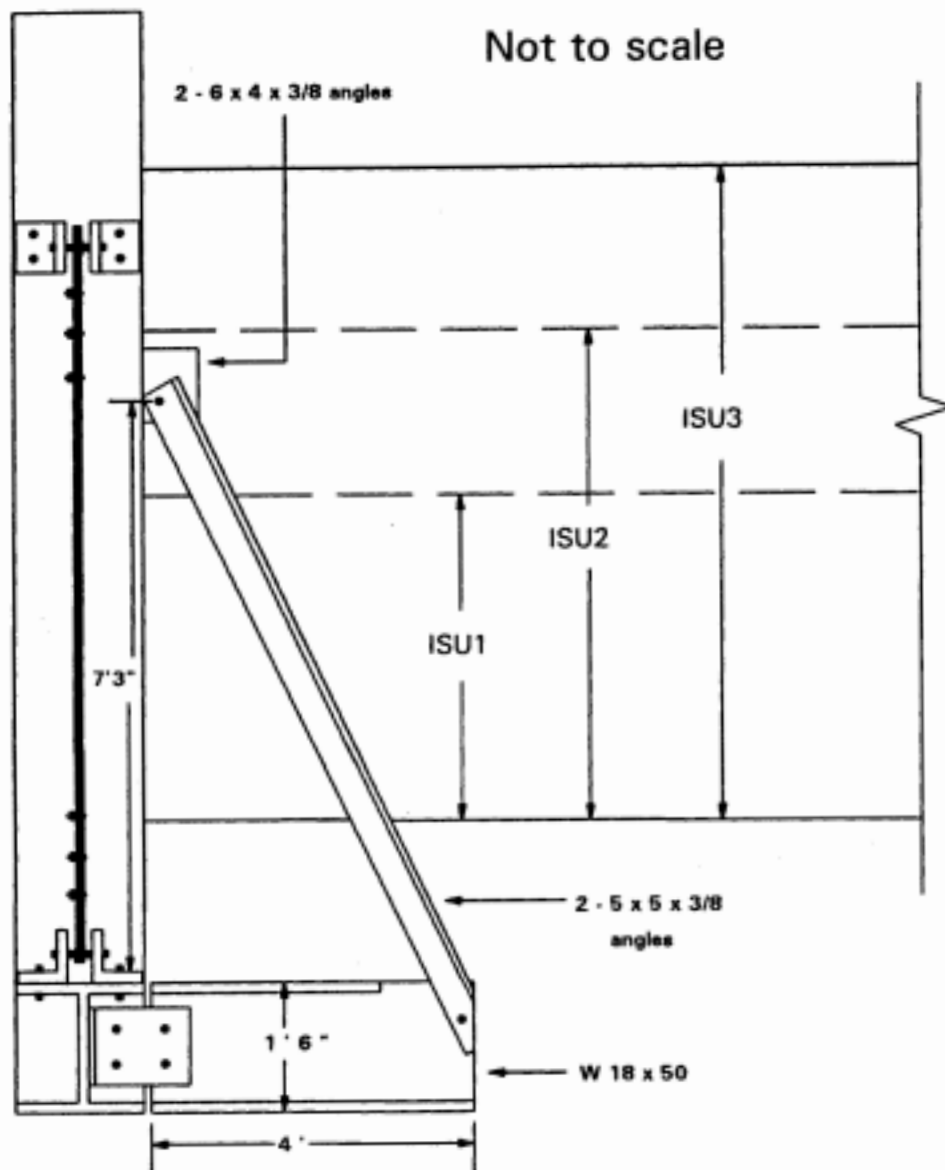
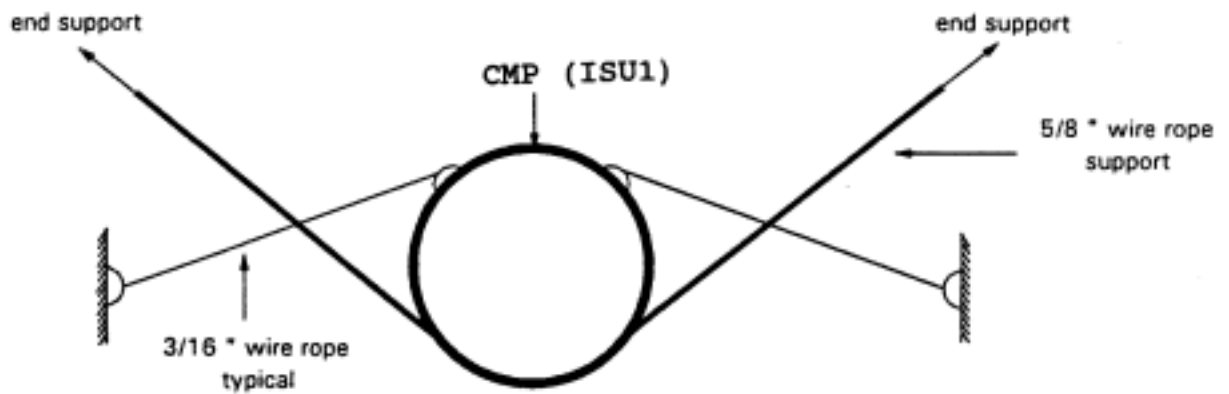


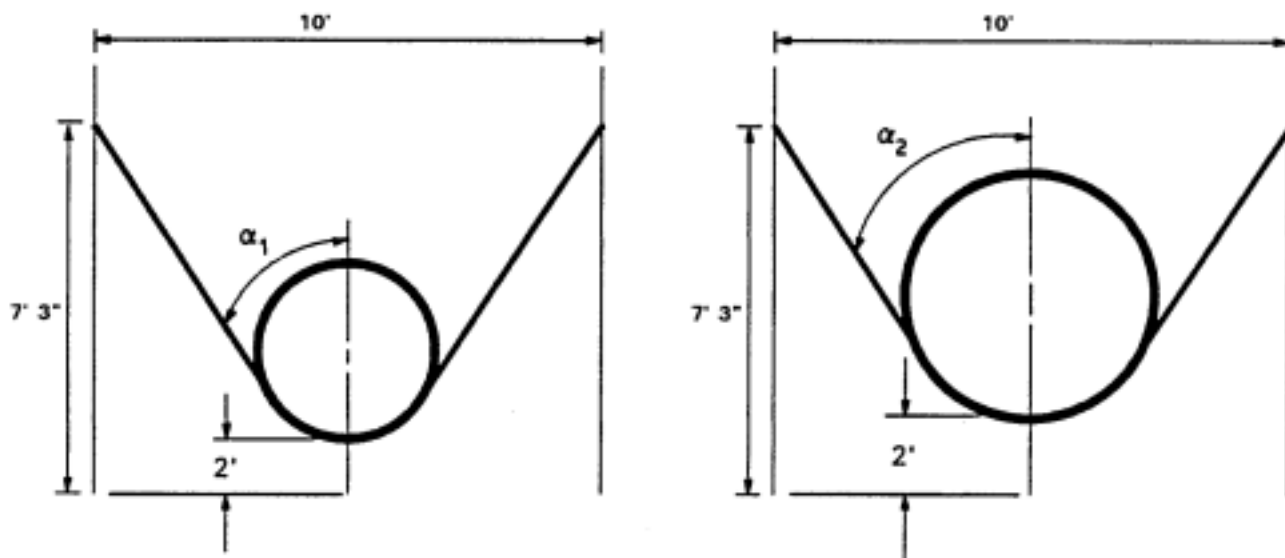
Figure 4.3 Side view of typical load frame.



Figure 4.4 Photograph of load frame with ISU1 being tested.



(a) restraint with tie-cables



(b) inherent restraint due to upward angle of end support wire rope

Figure 4.5 CMP rotational restraint.

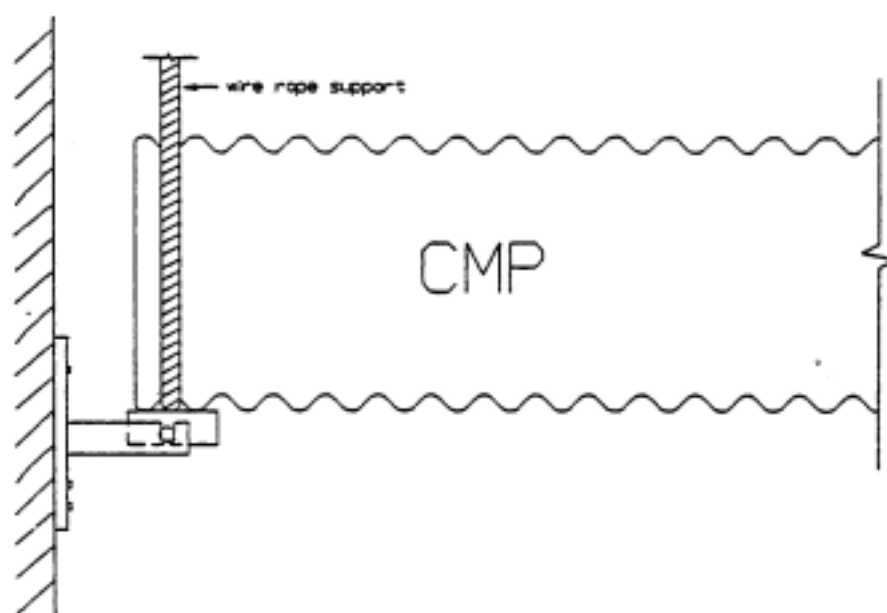
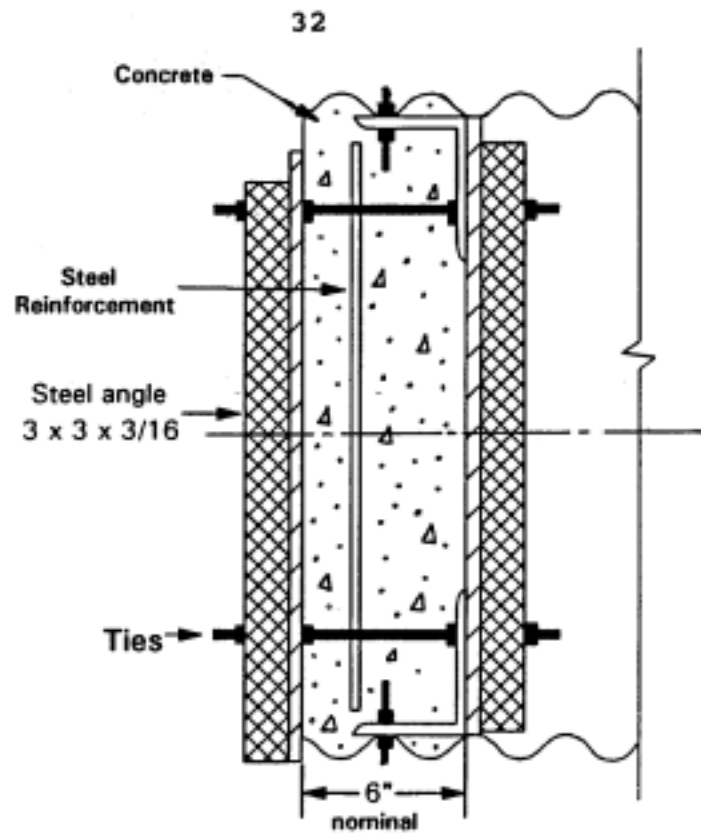
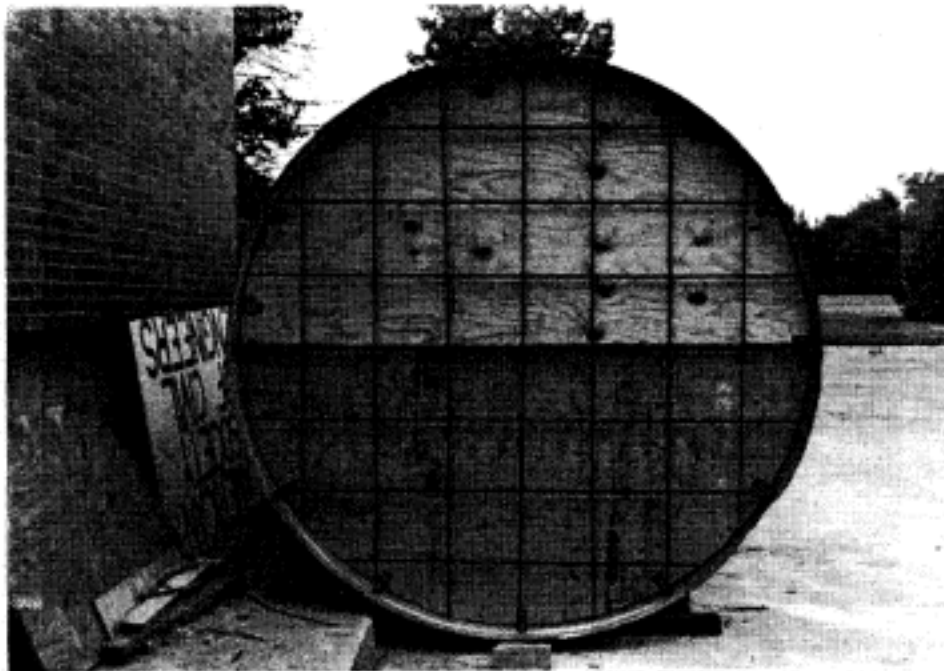


Figure 4.6 CMP longitudinal restraint.

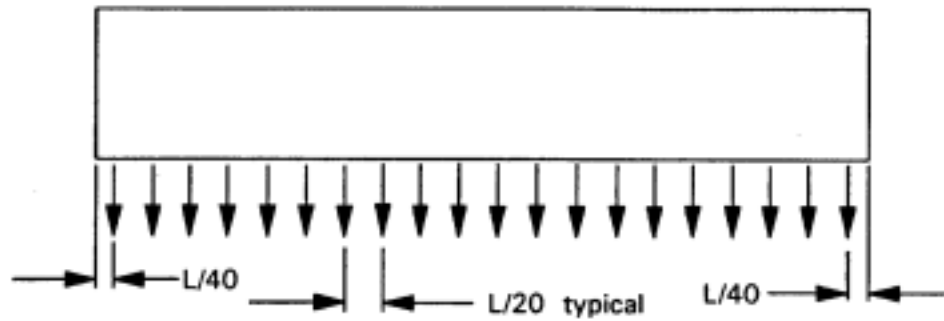


(a) longitudinal section view through typical CMP diaphragm

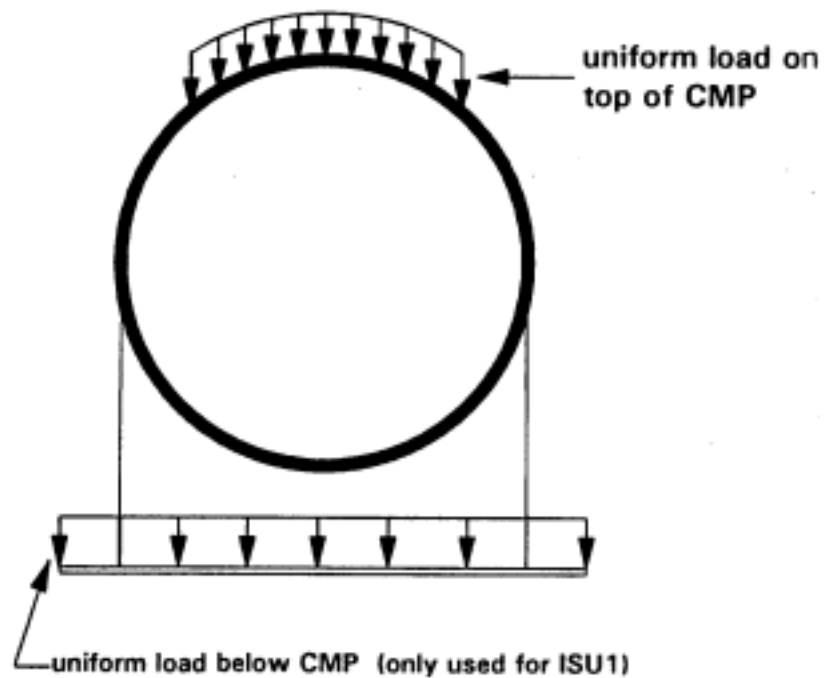


(b) end view of typical CMP diaphragm showing steel reinforcement

Figure 4.7 CMP diaphragm details.



(a) longitudinal view of CMP specimen
with locations of "distributed" loads
suspended below specimen



(b) transverse view of CMP specimen

Figure 4.8 Sand loading on CMP.

longitudinal direction during testing.

For the specimen 4 feet in diameter, it was necessary to provide restraint to prevent the CMP from rotating about its longitudinal axis if loading was placed slightly off center (see Figure 4.5a). For larger specimens, the possibility of rotation was limited as the angle of the wire rope end support decreased (i.e. in Figure 4.5b $\alpha_2 < \alpha_1$).

Horizontal restraint on one end of the CMP prevented longitudinal pipe movement as shown in Figure 4.6. These brackets, while limiting longitudinal movement, allowed end rotation of the CMP and elongation of the wire rope end supports.

4.3. CMP Diaphragms

Reinforced concrete diaphragms in both ends of the CMP specimens contained the water used as load inside of the pipes and also prevented potential distortion of the CMP cross section at the ends. A longitudinal section through the diaphragms in Figure 4.7a illustrates how the diaphragms are connected to the CMP. Reinforcement for the diaphragms is shown in Figure 4.7b.

4.4. Test Loading

Sandbags and water provided the loads on and in the pipes. The sandbags were used in the elastic range of each test and usually were stacked symmetrically about the centerline on the top of the CMP as shown in Figure 4.8. When testing Specimen ISU1 to failure, sandbags were also suspended from the CMP on platforms supported by 3/16 inch wire rope as shown in Figure 4.8b. Water load inside the pipes was combined with sand load to

provide enough load to collapse the specimens. As the CMP deflected vertically, the water load was no longer uniform along the CMP length therefore moments rather than loads are used to characterize the response of the pipes.

The testing program included a service load test and a failure load test for each specimen. Service loads were assumed to induce a moment in the CMP which resulted only in elastic deformations and included both loading and unloading. Loading in the service load tests was limited so that the maximum was applied in the elastic range, approximately 1/2 of the ultimate moment capacity of the CMP. The ultimate moment capacity was estimated using limited information provided by a manufacturer of CMP. In the failure load tests, the CMP was loaded until a corrugation collapsed on the compression side of the CMP. It was assumed that data from the elastic range of the failure test would replicate the data from the service load test. Tables 4.2 through 4.7 present loadings and longitudinal mid-span moments on the three specimens. Service load tests are referred to as ISU1SL, ISU2SL, and ISU3SL; similarly, failure load tests are referred to as ISU1F, ISU2F, and ISU3F.

4.5. Test Instrumentation

Test specimens were instrumented with six types of instrumentation including: electrical resistance strain gages, direct current displacement transducers (DCDT), vertical deflection gages, horizontal deflection gages, dial gages to monitor wire rope elongation, and a water level monitor.

Table 4.2 Test loading - ISU1SL.

| Load point | Uniform distributed load (lb/ft) | Non-uniform distributed load (lb/ft) | Mid-span moment (k-ft) |
|------------|----------------------------------|--------------------------------------|------------------------|
| 1 | 0 | 0 | 2.43 |
| 2 | 70 | " | 5.83 |
| 3 | 140 | " | 9.24 |
| 4 | 210 | " | 12.6 |
| 5 | 315 | " | 17.8 |
| 6 | " | 56 | 22.6 |
| 7 | " | 106 | 25.5 |
| 8 | " | 158 | 28.4 |
| 9 | " | 214 | 31.6 |
| 10 | " | 269 | 34.7 |
| 11 | " | 320 | 37.6 |
| 12 | " | 371 | 40.5 |
| 13 | " | 423 | 43.4 |
| 14 | " | 480 | 46.5 |
| 15 | " | 536 | 49.5 |
| 16 | " | 584 | 52.1 |

Table 4.3 Test loading - ISU1F.

| Load point | Uniform distributed load (lb/ft) | Non-uniform distributed load (lb/ft) | Mid-span moment (k-ft) |
|------------|----------------------------------|--------------------------------------|------------------------|
| 1 | 0 | 0 | 5.83 |
| 2 | 175 | " | 11.0 |
| 3 | 350 | " | 19.5 |
| 4 | 467 | " | 25.2 |
| 5 | 642 | " | 33.7 |
| 6 | 712 | " | 37.1 |
| 7 | 782 | " | 40.5 |
| 8 | 852 | " | 43.9 |
| 9 | 957 | " | 49.0 |
| 10 | 1062 | " | 54.1 |
| 11 | 1062 | 56 | 57.0 |
| 12 | Non-uniform * | 56 | 30.9 |
| 13 | 782 | 299 | 67.5 |

* Irregular arrangement of sand load on specimen due to load failure as discussed in section 4.1

Table 4.4 Test loading - ISU2SL.

| Load point | Uniform distributed load (lb/ft) | Non-uniform distributed load (lb/ft) | Mid-span moment (k-ft) |
|------------|----------------------------------|--------------------------------------|------------------------|
| 1 | 0 | 0 | 5.61 |
| 2 | " | 54 | 10.5 |
| 3 | " | 107 | 15.4 |
| 4 | " | 165 | 20.7 |
| 5 | " | 223 | 27.5 |
| 6 | " | 280 | 33.2 |
| 7 | " | 332 | 37.3 |

Table 4.5 Test loading - ISU2F.

| Load point | Uniform distributed load (lb/ft) | Non-uniform distributed load (lb/ft) | Mid-span moment (k-ft) |
|------------|----------------------------------|--------------------------------------|------------------------|
| 1 | 0 | 0 | 5.61 |
| 2 | " | 107 | 15.8 |
| 3 | " | 165 | 21.3 |
| 4 | " | 223 | 28.1 |
| 5 | " | 273 | 32.9 |
| 6 | " | 332 | 37.4 |
| 7 | " | 386 | 43.0 |
| 8 | " | 442 | 49.3 |
| 9 | " | 493 | 56.2 |
| 10 | " | 552 | 66.1 |
| 11 | " | 582 | 72 |

Table 4.6 Test loading - ISU3SL.

| Load point | Uniform distributed load (lb/ft) | Non-uniform distributed load (lb/ft) | Mid-span moment (k-ft) |
|------------|----------------------------------|--------------------------------------|------------------------|
| 1 | 0 | 0 | 7.81 |
| 2 | " | 62 | 12.2 |
| 3 | " | 125 | 17.1 |
| 4 | " | 186 | 21.9 |
| 5 | " | 247 | 26.9 |
| 6 | " | 313 | 32.3 |
| 7 | " | 375 | 37.4 |
| 8 | " | 440 | 42.7 |
| 9 | " | 499 | 47.7 |
| 10 | " | 560 | 52.7 |
| 11 | " | 622 | 58.0 |
| 12 | " | 686 | 63.4 |
| 13 | " | 752 | 68.9 |
| 14 | " | 809 | 73.8 |
| 15 | " | 876 | 79.7 |
| 16 | " | 935 | 84.9 |
| 17 | " | 994 | 90.1 |
| 18 | " | 1064 | 96.7 |
| 19 | " | 1125 | 102 |
| 20 | " | 1186 | 109 |

Table 4.7 Test loading - ISU3F.

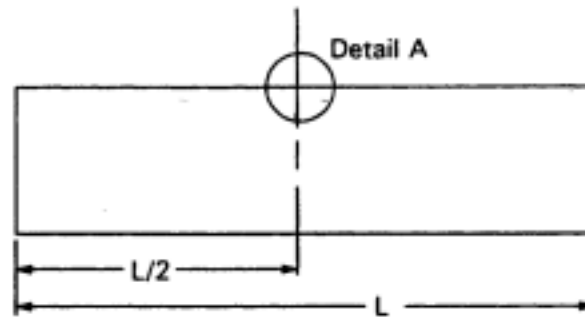
| Load point | Uniform distributed load (lb/ft) | Non-uniform distributed load (lb/ft) | Mid-span moment (k-ft) |
|------------|----------------------------------|--------------------------------------|------------------------|
| 1 | 0 | 0 | 7.81 |
| 2 | 70 | " | 12.1 |
| 3 | 130 | " | 16.3 |
| 4 | 190 | " | 20.6 |
| 5 | 250 | " | 24.9 |

Strain gages were attached to the CMP surface and coated with polyurethane as a moisture barrier. These 120 ohm gages with three-wire leads were wired in a quarter-bridge configuration. Strain gages are on the CMP centerline as shown in Figure 4.9; a diagram of a typical corrugation (both on the tension and compression sides of the pipe) with strain gage locations is shown in Figure 4.9. Strain gages were also mounted, as shown in Figure 4.10, at the quarter-point locations on the CMP to determine if the pipe was bending symmetrically.

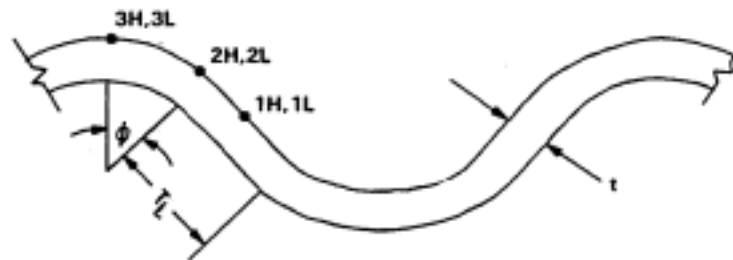
DCDT's were used to measure the movements between the corrugation peaks and were oriented around the circumference of the pipe at the longitudinal mid-point as shown in Figure 4.11

Vertical deflections were determined by reading CMP elevations on engineering scales suspended from the bottom of the CMP at the quarter points and at the mid-span as well as a scale attached to the top of the CMP at the mid-span. The scales were read with surveying transits. Engineering scales were used because large deflections were expected. Deflections as large as 21 inches could be measured with reasonable accuracy as the scales were accurate to the nearest 0.005 of a foot. Vertical deflections were used to calculate the flexural stiffness of the CMP, to quantify the deflected shape of the CMP, and to determine changes in the CMP vertical diameter.

The deflected shape was used to account for the non-uniform depth of water along the length of the CMP as discussed in the Section 4.4. Variations in the water depth along the CMP were



(a) CMP specimen



| Gauge | Location | Orientation |
|-------|------------------|--------------|
| 1H | Inflection Point | Hoop |
| 1L | Inflection Point | Longitudinal |
| 2H | Tangent Point | Hoop |
| 2L | Tangent Point | Longitudinal |
| 3H | Crest | Hoop |
| 3L | Crest | Longitudinal |

(b) Detail A; strain gages are at mid-span

Figure 4.9 Typical location of strain gages at mid-span.

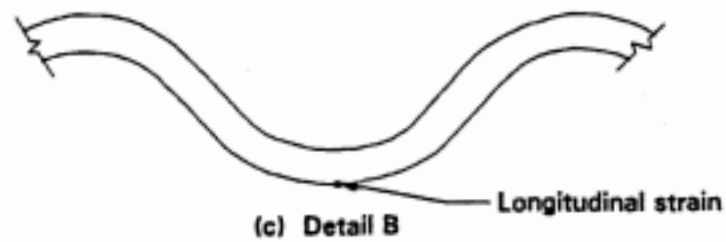
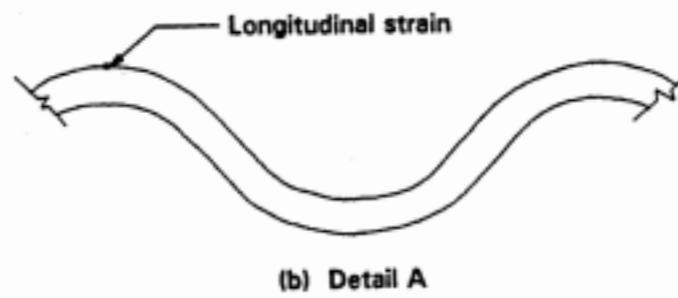
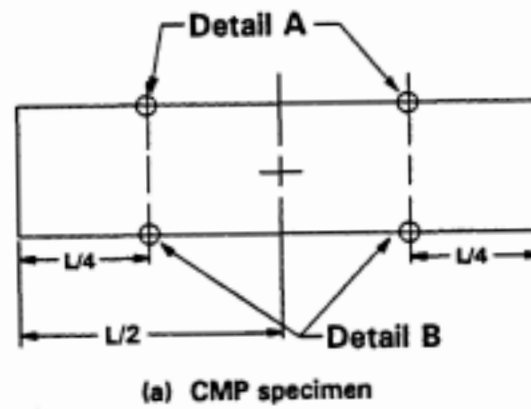
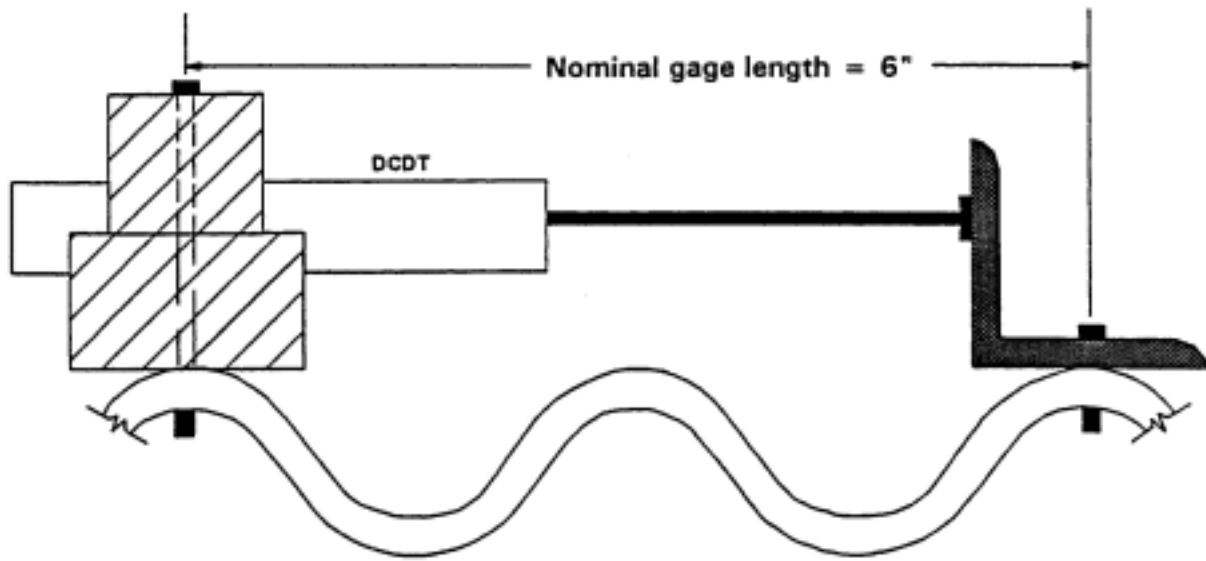
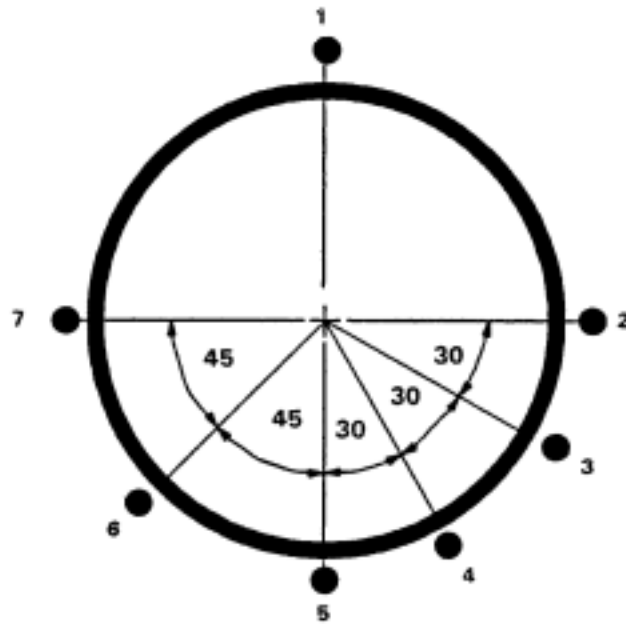


Figure 4.10 Typical location of strain gages at quarter-spans.



(a) attachment of DCDT to corrugation



(b) locations of DCDT installations around the transverse section view

Figure 4.11 Installation of DCDT's at CMP mid-span.

used to calculate the moment caused by the non-uniform load. Vertical deflections of the top and bottom of the CMP were subtracted to determine changes in diameter of the CMP at the centerline.

A steel rod and DCDT were placed horizontally between adjacent walls of each test specimen to measure changes in the horizontal CMP diameter (see Figure 4.12). This allows the measuring system to move with the CMP during testing.

Dial gages were used to measure vertical deflection due to wire rope elongation at the end support locations as shown in Figure 4.13. Vertical deflections were needed to determine actual CMP vertical deflection as noted in Section 4.2.

To determine the depth of water in the CMP at any time, three flexible tubes were attached to the bottom of the test specimens and positioned vertically on a calibrated board. The water level in the tubes was the same as the water level in the CMP. Although this system was simple, it was quite accurate. The only problem occurred with test Specimen ISU2 which deflected to such an extent that the top of the CMP at the middle came in contact with the water surface during the failure test. The CMP then became pressurized and the water depth readings were not accurate.

Water depth data and vertical deflection data were recorded manually after each load increment. Data from all strain gages and DCDT's were recorded with a Hewlett-Packard data acquisition system (DAS).

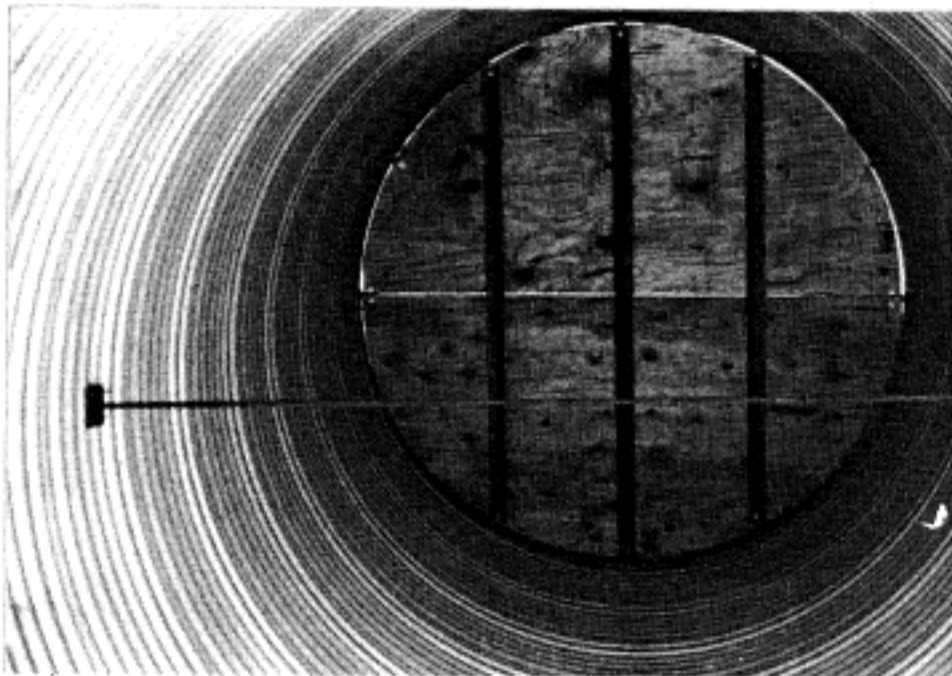


Figure 4.12 Interior view of diaphragm form and rod used to measure relative wall movement.

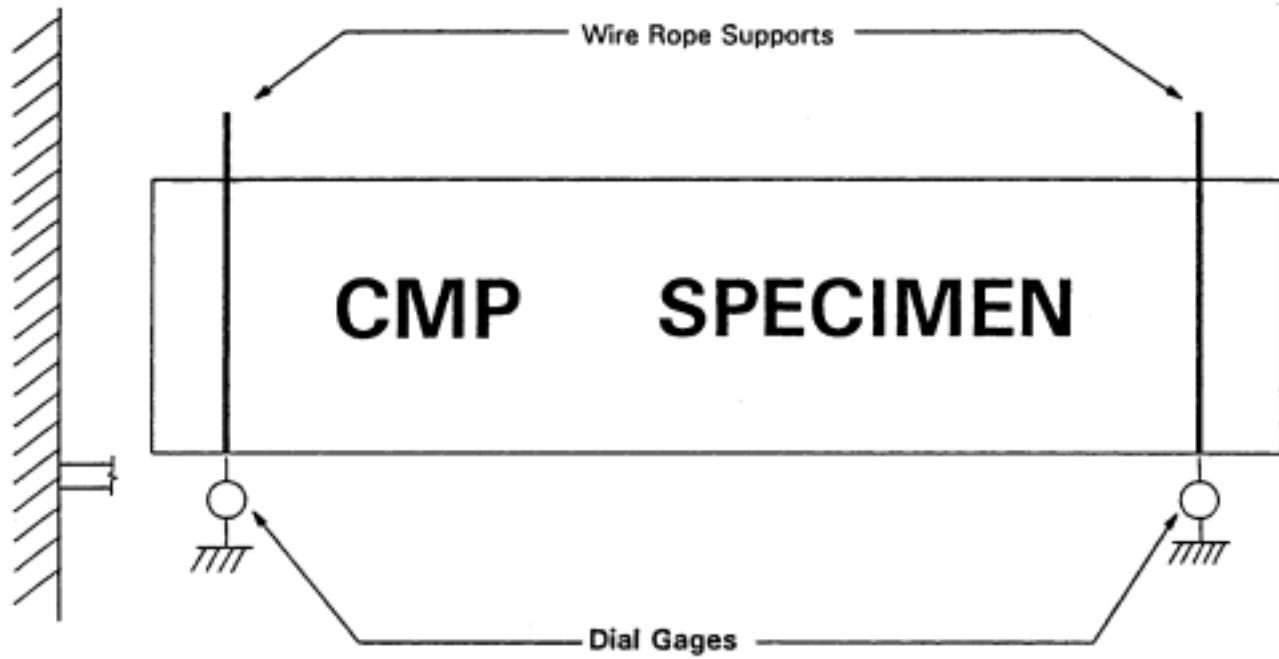


Figure 4.13 Dial gages to measure CMP deflection due to cable elongation.

4.6. Uniaxial Tensile Tests

Two CMP wall sections were removed from Specimen ISU3 and tested in uniaxial tension according to ASTM standard E-8 (ASTM, 1991). Because of the curvature of the specimens, strain gages were utilized to measure biaxial strains on both sides of the specimens. The strains from both sides were averaged to account for the bending that occurred as the specimens straightened during the tension test.

5. EXPERIMENTAL RESULTS

5.1 Scope of Reported Results

Results from the tests performed on Specimens ISU1, ISU2, and ISU3 are presented in this section. Applied moments, mid-span vertical deflections and steel surface strains, on the compression sides of the pipes are reported here. Strains on the tension side of the specimens were generally smaller than strains measured at corresponding corrugation positions on the compression side and therefore are not reported. Strain data from the quarter point locations on the specimens indicated symmetrical behavior; as their magnitude was significantly smaller than the midspan strains they have been omitted from this report.

DCDT data were recorded to evaluate the speculation that horizontal corrugation crest displacements would be proportional to the vertical distance from the CMP neutral axis of longitudinal flexure. Although this was found to be generally true, there are a few exceptions. Also, horizontal crest displacements at the top and bottom of the CMP were not always similar values. This difference between top and bottom displacements may be related to a shift of the CMP neutral axis in flexure.

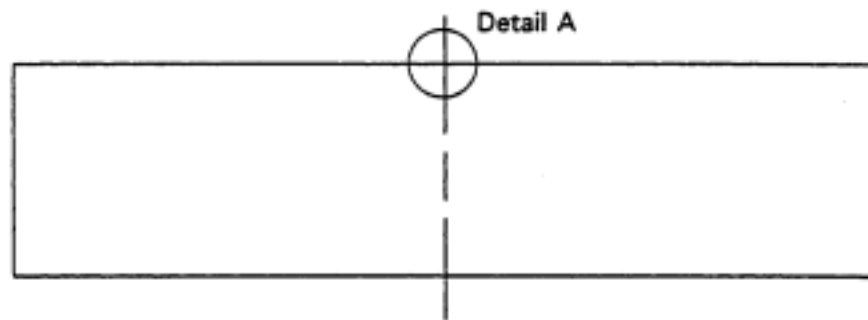
Horizontal diameter change data are not shown, but indicate that significant cross-sectional distortions occurred due to placement of the load on different parts of the cross-section. As a result, all deflection data used for calculation of the CMP

flexural EI factors were obtained from the location on the CMP where the load was not placed during the test. Longitudinal moment capacity, stiffness, and mid-span deflections measured or calculated from test measurements are summarized and discussed here.

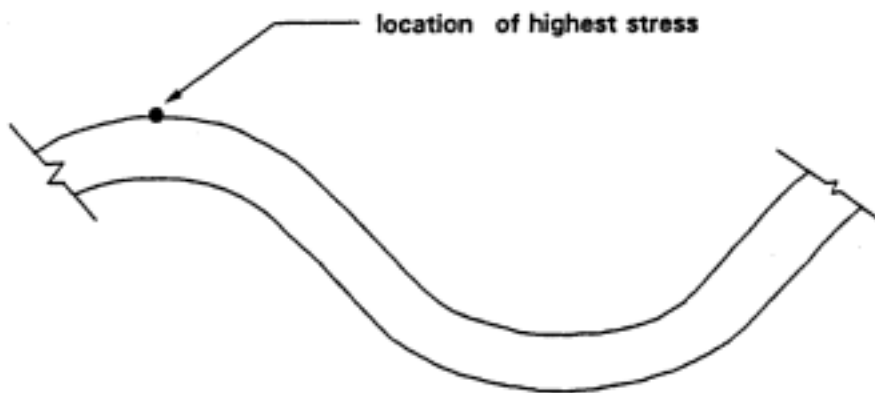
Yield moments are defined as those moments which cause the element under the highest stress on the CMP (see Figure 5.1) to reach a yield stress state. The yield stress state is identified by the point at which the relationship between longitudinal strain at the corrugation crest and applied moment becomes non-linear. Ultimate moments are reached when the corrugation under the greatest stress collapses, as shown in Figure 5.2, and deflections become excessive and unpredictable. Maximum deflection values are reported at incipient collapse, just prior to the large deflection associated with corrugation collapse.

As noted in Chapter 4, water load was used in many of the tests. The determination of the moments from this load is presented in Appendix A. Because wire rope elongation was part of the vertical deflection measurements, CMP deflections were measured at both ends of the CMP. They were then averaged and subtracted from the vertical deflection measurements to determine the CMP deflections due to flexure.

Stiffness values were calculated from the service load tests assuming that the simple-span CMP is a small beam subjected to uniform distributed loads. It is recognized that this approach is a broad extension of the original intent of the following



(a) CMP specimen



(b) Detail A

Figure 5.1 CMP element subjected to the highest stress.

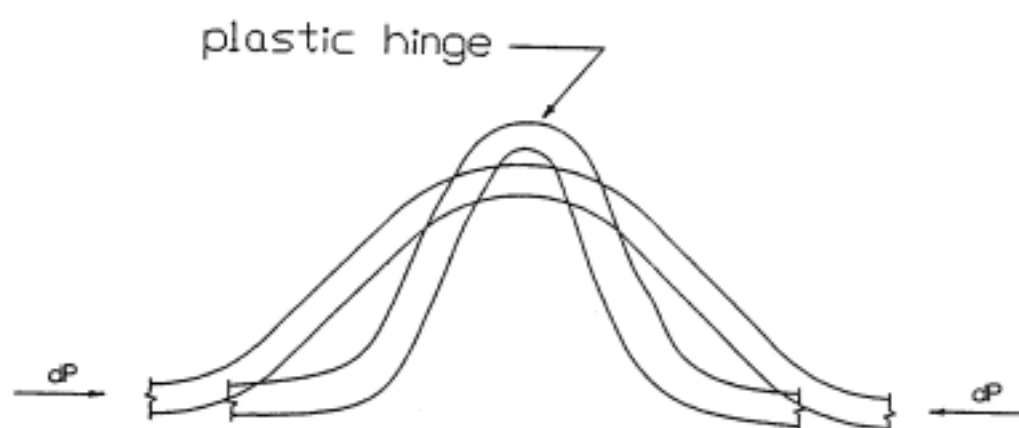


Figure 5.2 Idealized corrugation collapse.

equations. Secondary effects in the behavior of large diameter CMP, including a shift in the neutral axis, may make these equations subject to question; however, a similar approach was employed by Lane (1965), so these equations may be viewed as a first approximation solution to the problem of determining EI for CMP.

The equation for deflection is:

$$\Delta_v = \frac{5wL^4}{384EI} \quad (6)$$

and the equation for moment is:

$$M_{MS} = \frac{wl^2}{8} \quad (7)$$

where:

- Δ_v = vertical deflection at midpoint of CMP
- w = uniform distributed load
- L = length of CMP between supports
- EI = longitudinal stiffness factor for CMP
- M_{MS} = mid-span moment applied to CMP

Combining equations, EI can now be calculated:

$$EI = \frac{5M_{MS}L^2}{48\Delta_v} \quad (8)$$

5.2. Moment vs. Vertical Deflection

Figures 5.3 through 5.5 show the results of moment vs. midpoint deflection for each CMP specimen tested under both service loading and failure loading. Service load tests are shown as dashed lines and failure tests as solid lines. Each

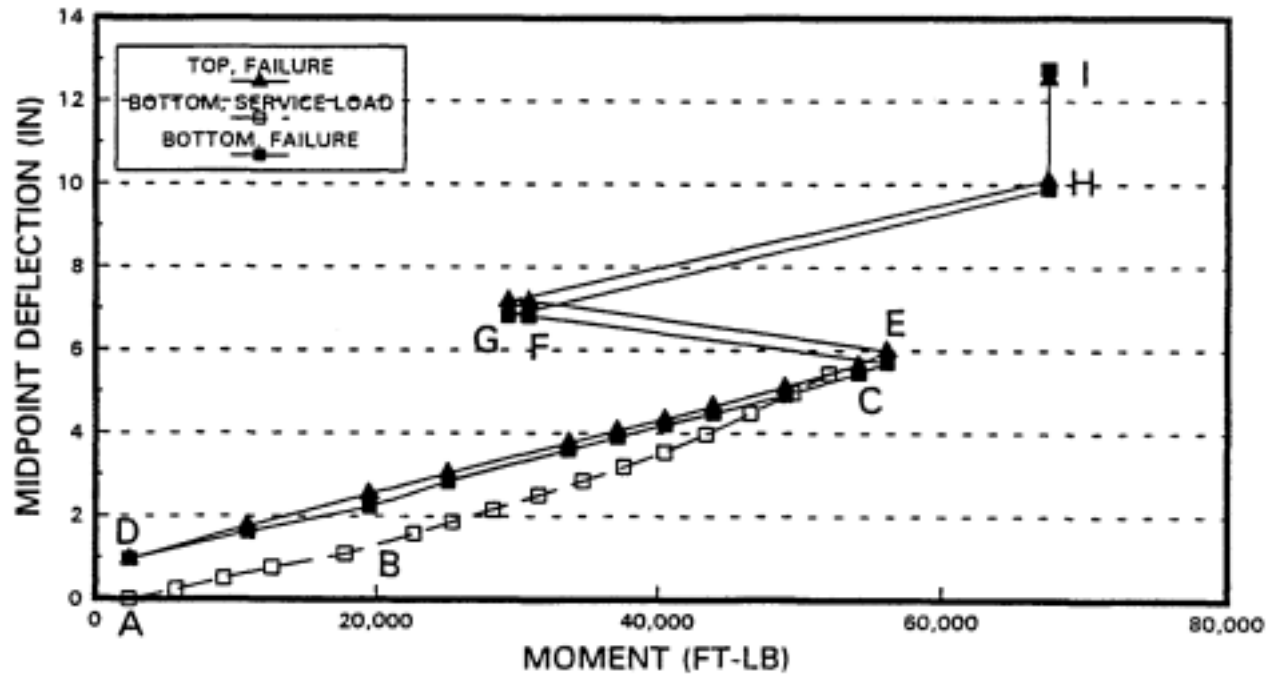


Figure 5.3 Moment vs. mid-span deflection (ISU1).

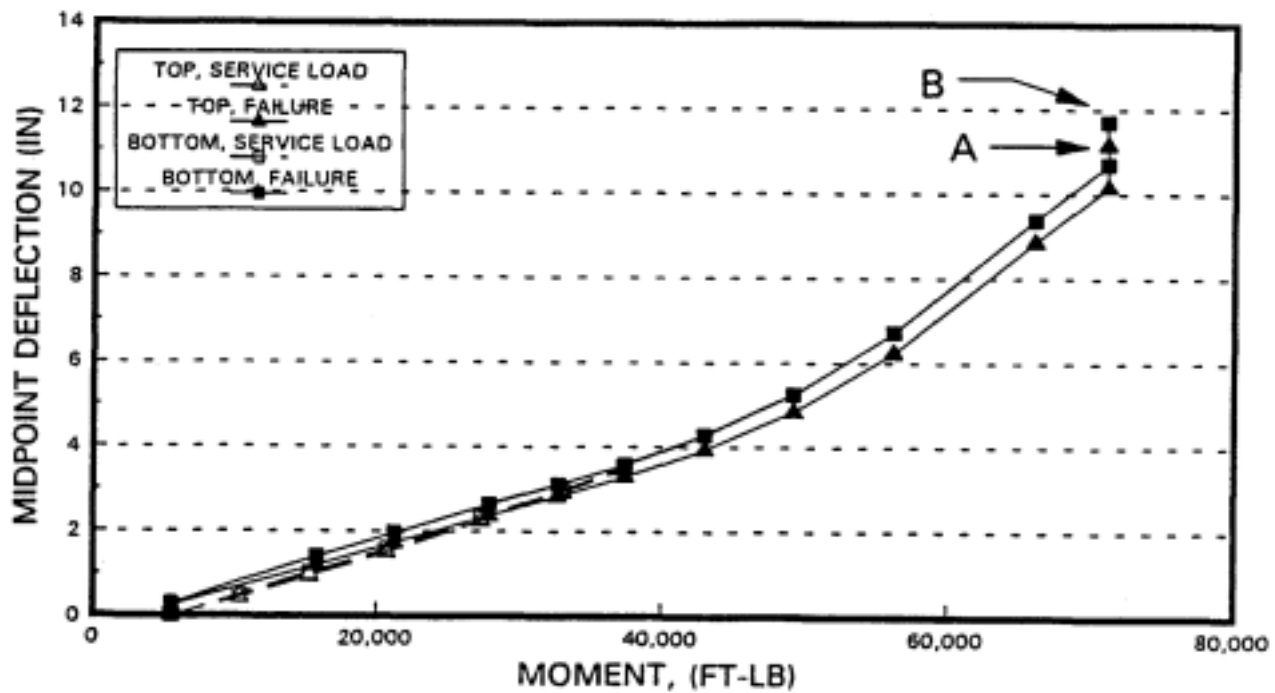


Figure 5.4 Moment vs. mid-span deflection (ISU2).

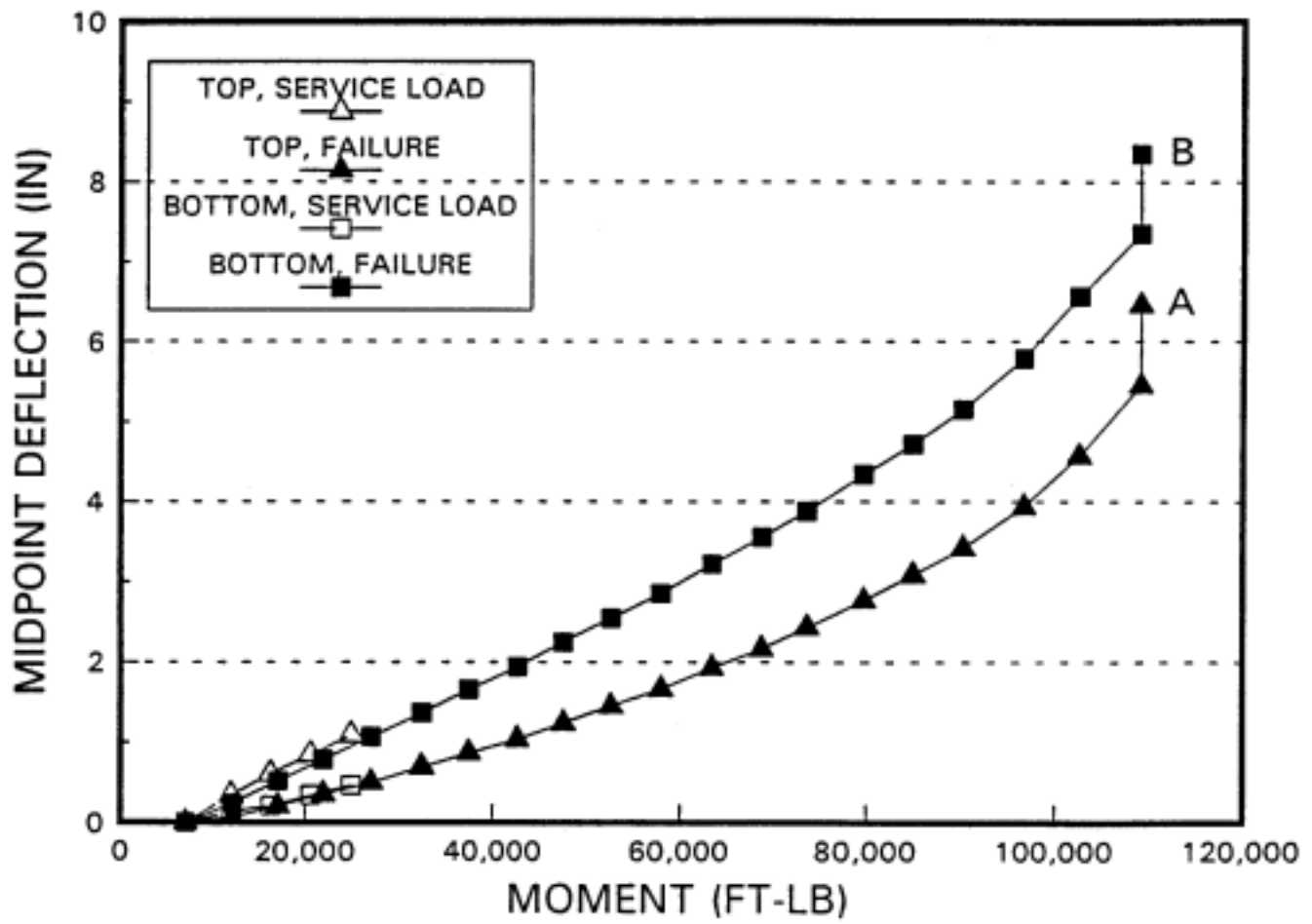


Figure 5.5 Moment vs. mid-span deflection (ISU3).

graph shows an initial moment due to the CMP self-weight at zero deflection. The vertical lines at the end of each curve represent the sudden deflections which occur when the specimens reach an ultimate moment. Moment values and EI factors derived from the graphs are shown in Table 5.1.

Test results on Specimen ISU1 are shown in Figure 5.3 where significant points on the curve are identified by letters. Figure 5.3 shows a linear load-deflection curve between A and B due to sand loading. The curve becomes non-linear between B and C due to the water loading which is vertically elongating the CMP cross-section. Thus, the deflection is due partly to flexure and partly to localized cross-section deformations. The failure test shows a linear curve from D to C where the loading is all sand. It appears that the top and bottom deflections in this region are similar because the wire ropes which support the hanging sand may be providing lateral resistance on the sides of the CMP which resist cross-sectional distortions. The loading between D and E is water. At E, a load shift occurred and a portion of the sand load fell from the CMP. Although the mid-span moment on the CMP decreased, the CMP deflection did not significantly decrease and appears to have actually increased; this may be evidence of plastic deformations of the CMP which occurred at or before the instant when the sand fell from the specimen. F and G represent the mid-span moments due to sand remaining on the pipe immediately after the load shift and due to the sand which has been leveled and re-stacked on the CMP. H is the deflection at

Table 5.1 Summary of flexural test results.

| Parameter | Specimen | | |
|-------------------------------------------|-------------------|------------------------|------------------------|
| | ISU1 | ISU2 | ISU3 |
| Diameter (In.) | 48 | 72 | 96 |
| Corrug. Sty. | 3x1 | 3x1 | 3x1 |
| Fabric. Style | Continuous Weld | Continuous Weld | Continuous Weld |
| Nominal Length (ft) | 20 | 25 | 24 |
| Eff. Length (in.) | 236.5 | 293.5 | 286 |
| Gage | 12 | 14 | 14 |
| Weight (lb/ft) | 50 | 75 | 100 |
| Yield Moment (10^3 k-ft) | 22.6 | 20.7-27.5 ^a | 32.3-42.7 ^a |
| Ultimate Moment (10^3 k-ft) | 67.5 | 71.0 | 109.1 |
| EI (1×10^6 lb-in ²) | 911 | 1060 | 3443 |
| Mid-span Defl. (In) @ yield moment | 1.5 | 1.5-2.3 ^b | 0.7-1.0 ^b |
| Mid-span Defl. (In) @ ultimate moment | <5.4 ^c | >10.7 ^c | 7.25 |

^a difficult to interpret a single value for location of non-linear behavior; range is used

^b deflections in the range of interpreted yield moment

^c unable to measure deflection at instant of incipient collapse

which the ultimate CMP moment was reached and I is the deflection that occurred after the specimen collapse.

Figure 5.4 contains data for Specimen ISU2 and shows fairly uniform behavior throughout both tests; this uniformity may be a result of loading only with water during both the service load and failure tests. A and B are the mid-span, post-collapse deflections that were estimated.

Figure 5.5 shows a significant difference in top and bottom deflection throughout the loading ranges. This diameter change may be larger than the changes for the other specimens because Specimen ISU3 has the largest radius; and vertical diameter changes are known to be a function of the CMP radius cubed (Young, 1989). The vertical diameter decreases during the service load test with sand loading and increases during the failure test with water loading. This response is expected when the loading system of sand on the top and water inside the pipe is considered.

Figures 5.6 through 5.8 show test specimens after loading to flexural failure. Specimen ISU2, shown in Figure 5.7, has a large vertical deflection which is due partly to the loading which was still applied to the CMP when the picture was taken. Specimens ISU1, Figure 5.6, and ISU3, Figure 5.8, show permanent deflection only. Figure 5.9 shows the specific locations of the collapsed corrugations in each of the three test specimens. Specimens ISU1 and ISU3 collapsed at locations near the mid-span which carries the maximum moment whereas Specimen ISU2 collapsed

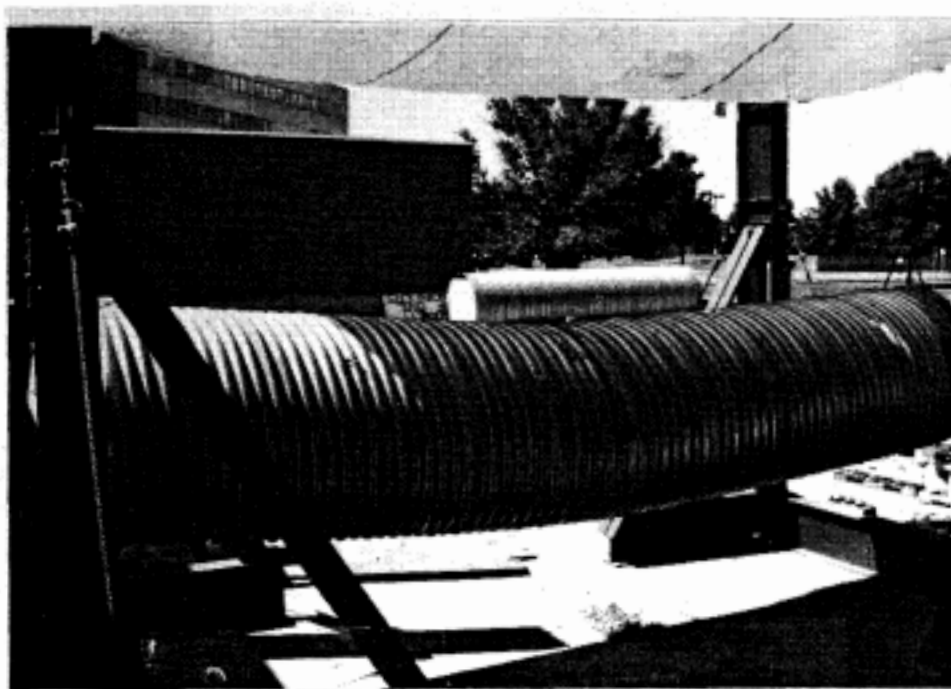


Figure 5.6 ISU1 after collapse.

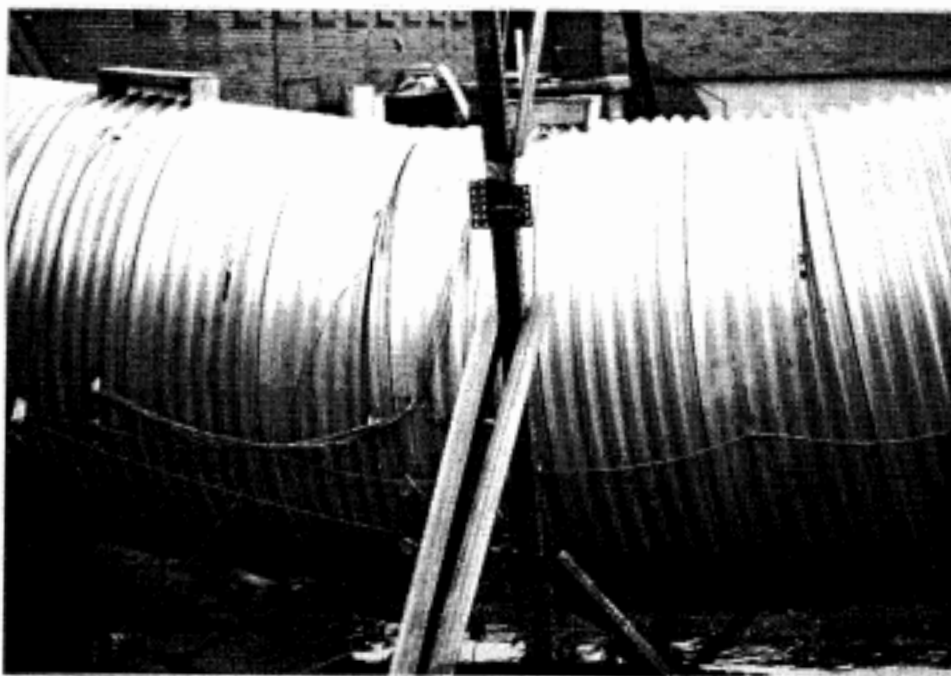


Figure 5.7 ISU2 after collapse.

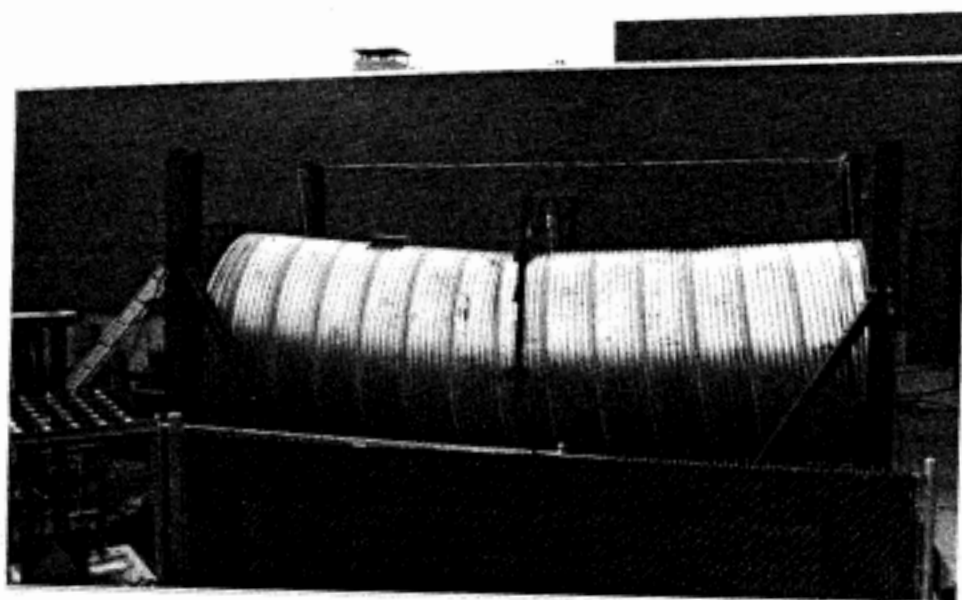
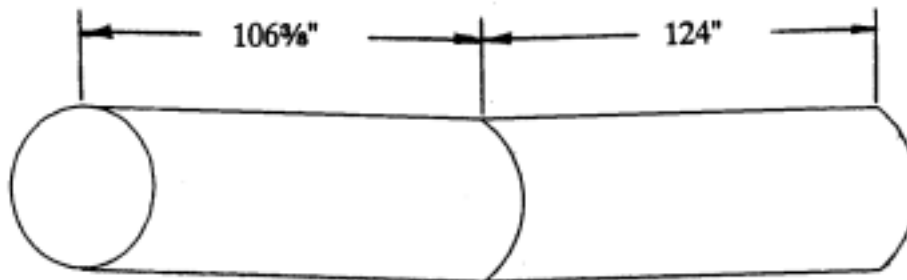
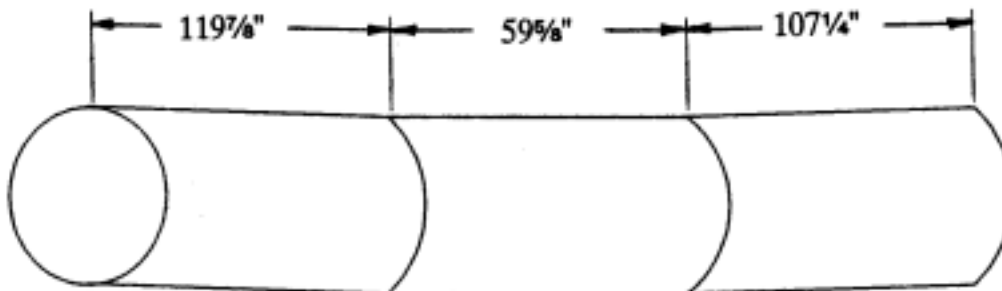


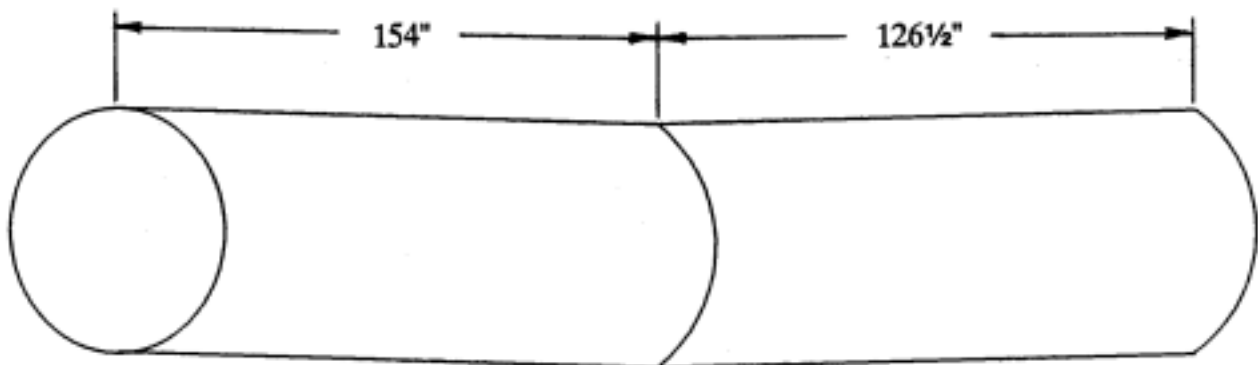
Figure 5.8 ISU3 after collapse.



(a) ISU1



(b) ISU2



(c) ISU3

Figure 5.9 Locations of corrugation collapse.

at two locations that were not under the greatest moment. The reason for this anomaly is not clear.

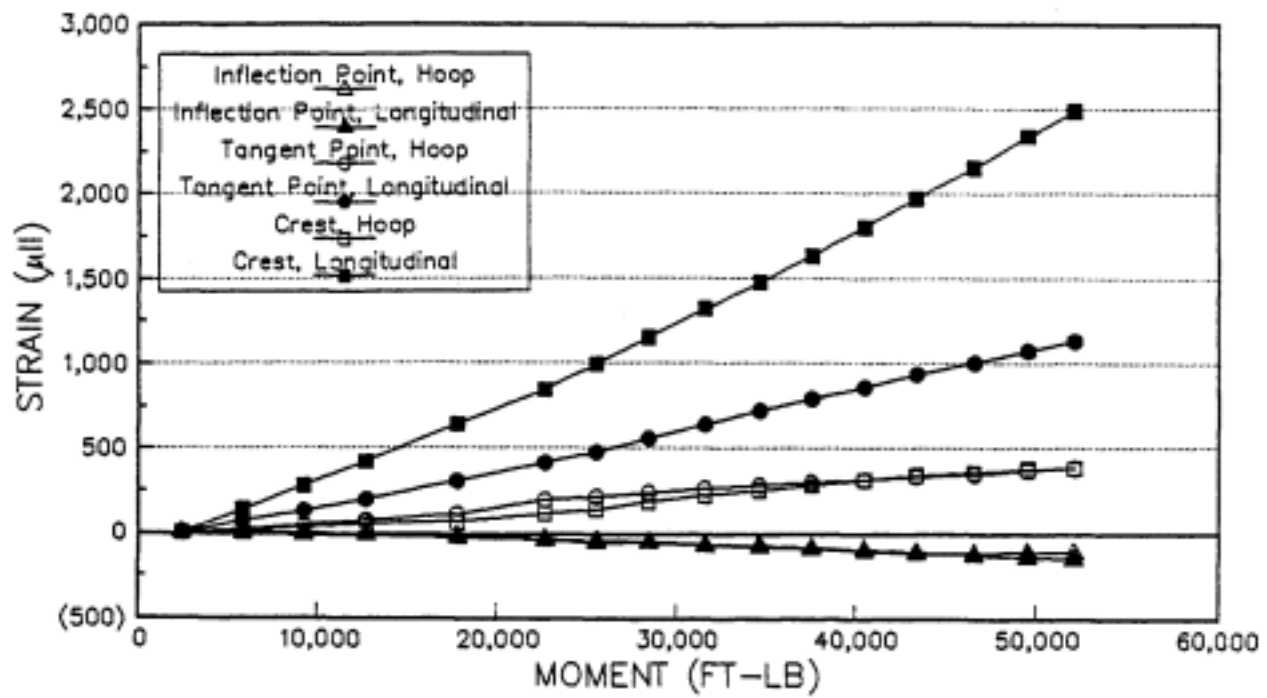
5.3. Moment vs. Corrugation Strain

Figures 5.10 through 5.12 show strains on the CMP near the element subject to the greatest stress. Tensile strains are shown as positive values. Each figure shows either a point or a range where non-linear crest strains begin; and these moments or range of moments are defined as failure for each specimen. All the graphs show an initial moment at zero strain due to the CMP self-weight.

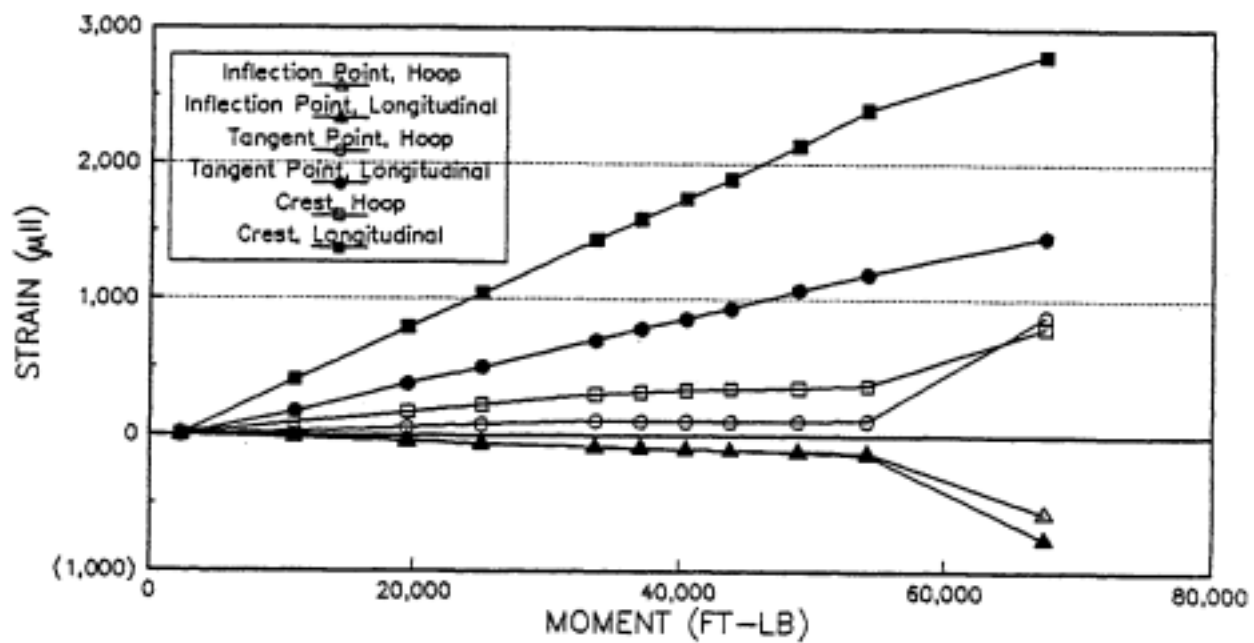
In general, longitudinal and hoop strains at the inflection points, shown in Figure 5.13, have small positive and negative values indicating the presence of small stresses. These longitudinal stresses may result from inaccurate placement of strain gages on the inflection point or from axial shortening which occurs in addition to the flexural effects. Longitudinal strains at the tangent point and crest, as shown in Figure 5.13, are typically greater than hoop strains at the same locations. Figure 5.12, for Specimen ISU3, shows tangent point strains which are compressive rather than the typical tensile strains at this location. This is probably caused by the sand loading on top of the pipe.

5.4 Uniaxial Tensile Test Results

Results from the tensile tests include yield stress, ultimate stress, and modulus of elasticity of the specimens as shown in Table 5.2. The average yield stress from the two tests

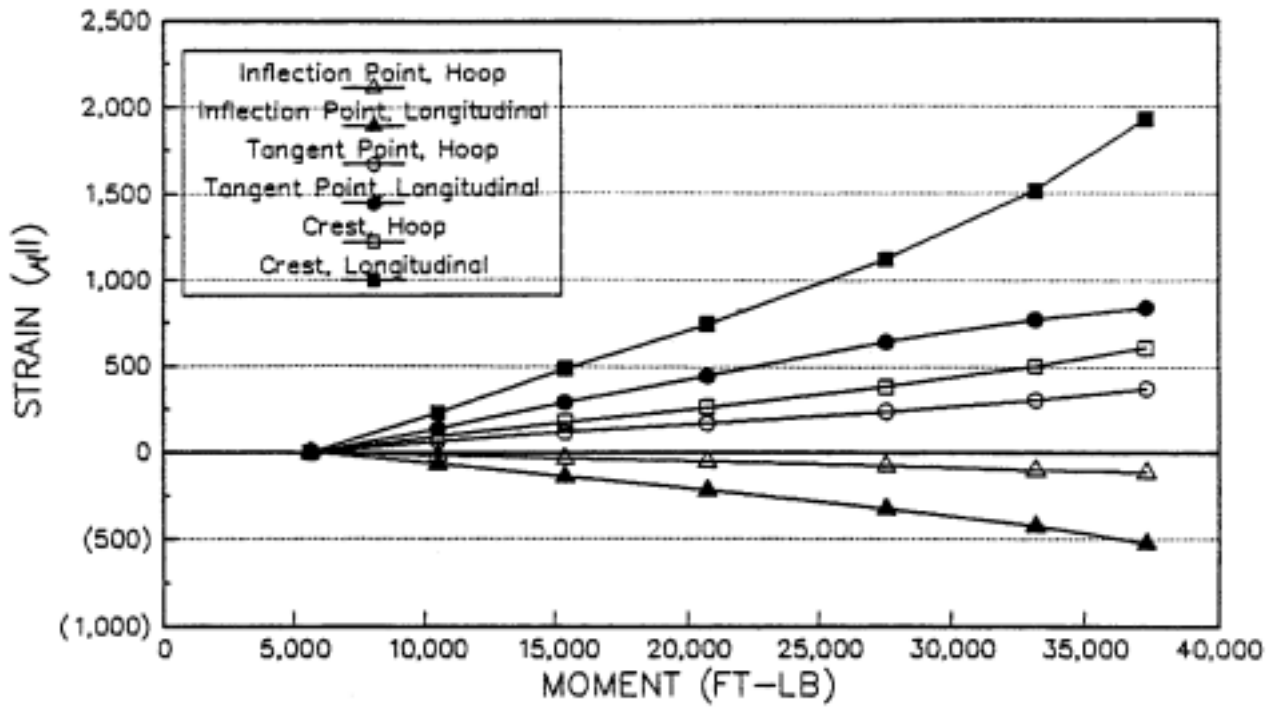


(a) service load test

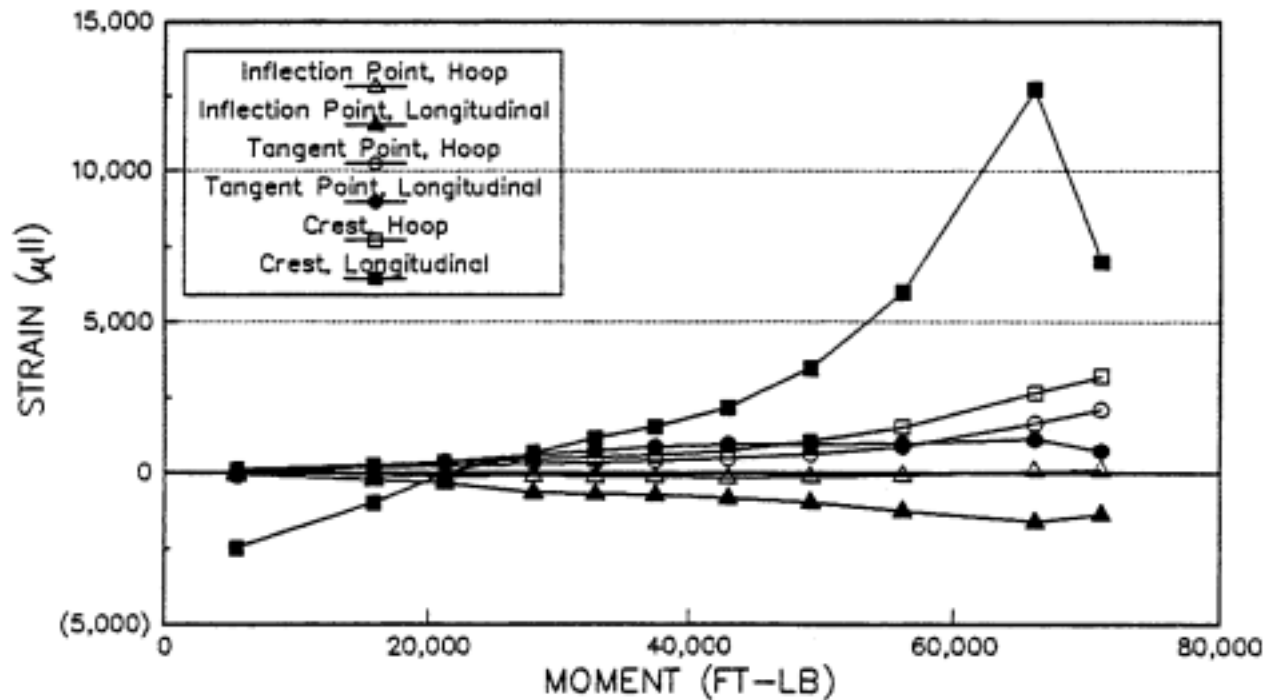


(b) failure test

Figure 5.10 Moment vs. strain (ISU1).

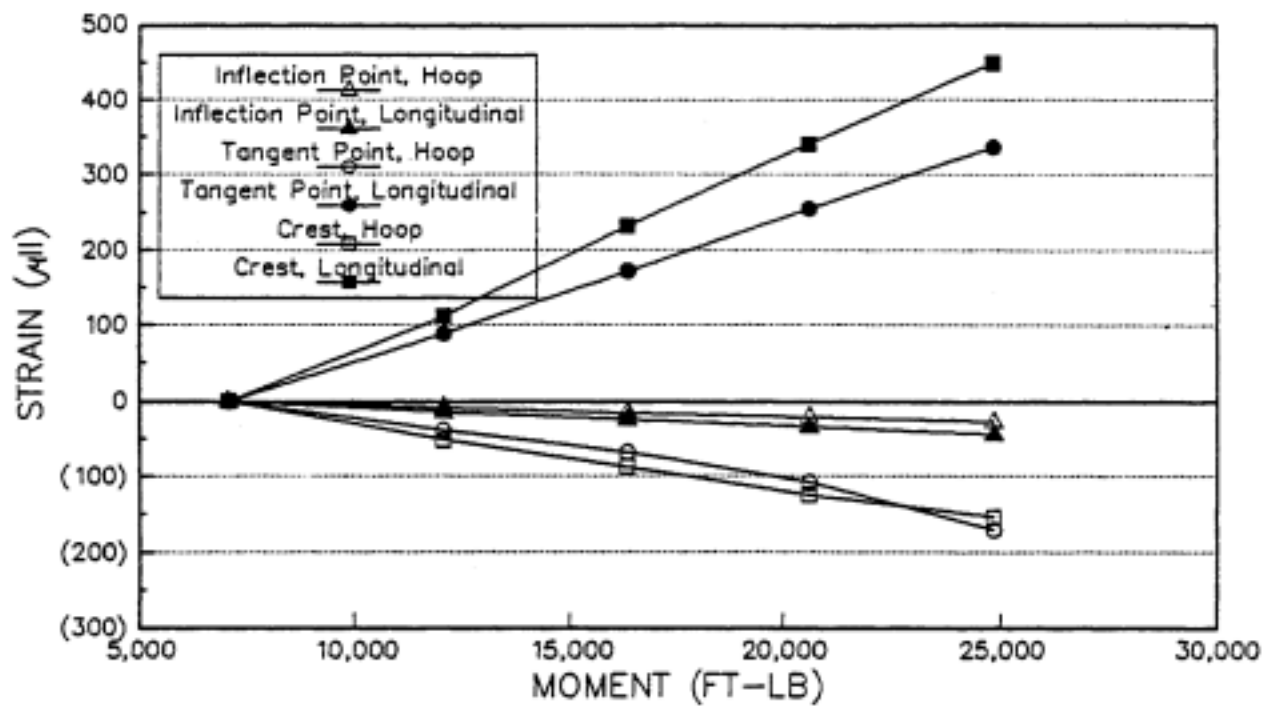


(a) service load test

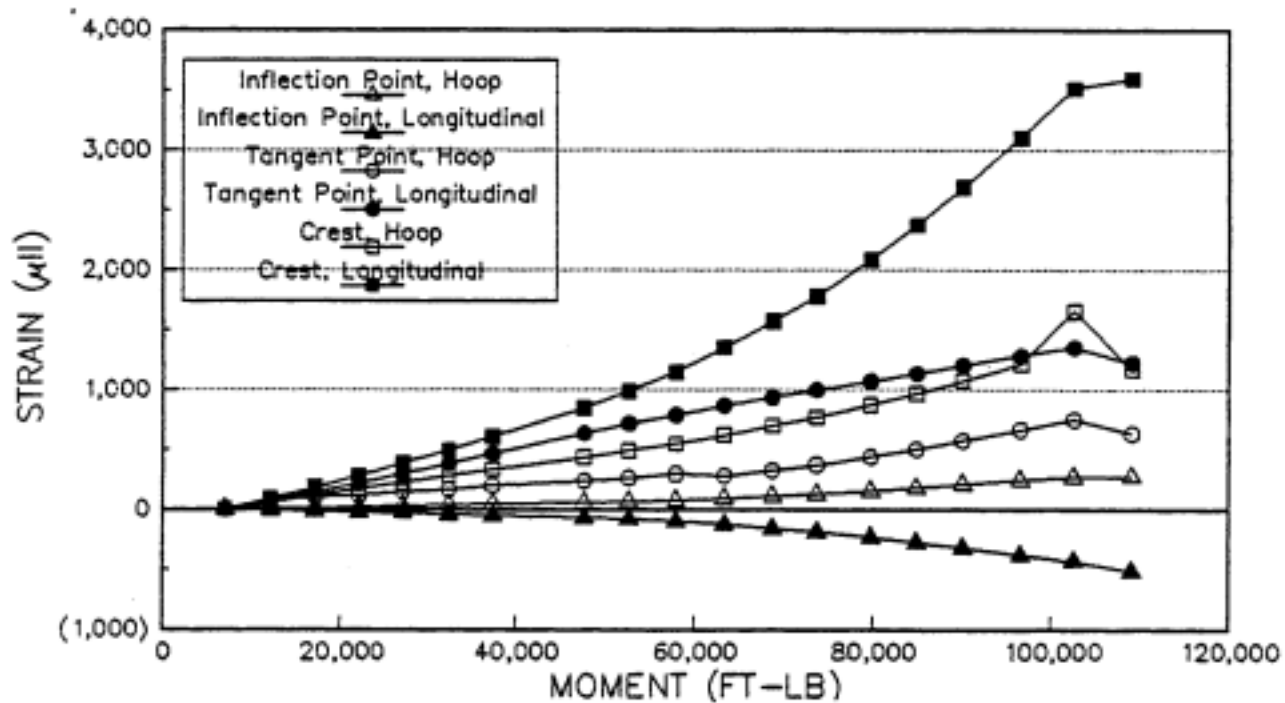


(b) failure test

Figure 5.11 Moment vs. strain (ISU2).

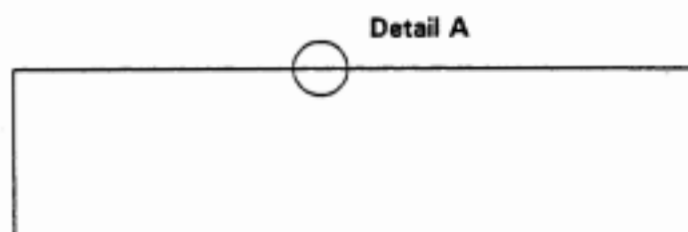


(a) service load test

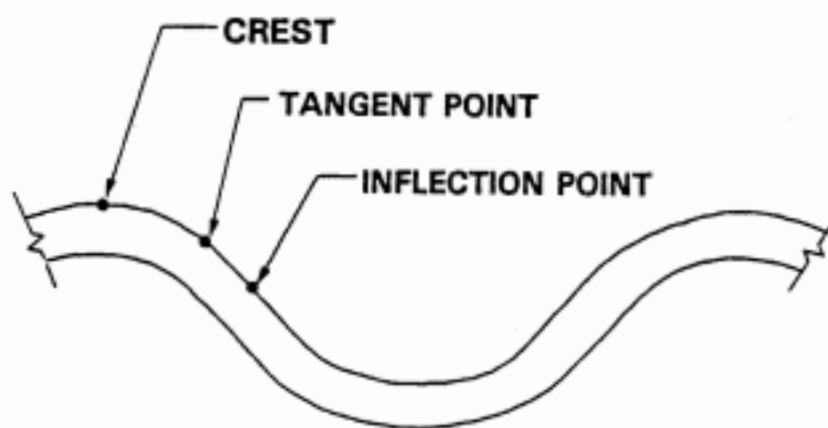


(b) failure test

Figure 5.12 Moment vs. strain (ISU3).



(a) CMP specimen



(b) Detail A

Figure 5.13 Corrugation reference points.

Table 5.2 Tensile test results.

| Material Property | Wall Section 1 | Wall Section 2 | Average Value |
|------------------------------|--------------------|--------------------|--------------------|
| Yield Strength (psi) | 62,000 | 76,400 | 69,200 |
| Ultimate Strength (psi) | 69,170 | 83,400 | 76,300 |
| Young's Modulus (psi) | 34.2×10^6 | 37.3×10^6 | 35.8×10^6 |
| Base metal thickness (in) | 0.075 | 0.076 | 0.0755 |

is 69,200 psi and the average modulus of elasticity is 36.5×10^6 psi. These values are considerably higher than the nominal values for steel, so they are not used for further analysis.

Yield stresses are calculated for each flexural specimen based on measured strains within the CMP wall. Poisson's ratio for steel is taken as 0.3, and modulus of elasticity, E , as 29×10^6 psi, which are accepted values by ASTM. The yield stresses are shown in Table 5.3. Yield stresses for a specific element on the CMP surface are characterized by two values; hoop stress at yield and longitudinal stress at yield.

5.5 Ratios of Hoop Strain to Longitudinal Strain

Strain ratios, K_ϵ , are tabulated in Table 5.4 for each test at both the tangent point and the crest locations on the tops of the pipes. The measured strains appear to be influenced by external factors such as localized load placement; therefore, many of the strain ratios are not used for further analysis. Strain ratios for the tangent point and crest are typically averaged. The strain ratios are used to calculate ratios of hoop stress to longitudinal stress with the Poisson's ratio and modulus of elasticity. The resulting stress ratios are 0.61 for Specimens ISU1 and ISU2 and 0.66 for ISU3. When theoretical formulas are applied to other CMP specimens, an average value of 0.63 is used.

Table 5.3 Yield stress values calculated from yield strain measurements.

| Test | Longitudinal yield stress (psi) | Hoop yield stress (psi) |
|------|---------------------------------|-------------------------|
| ISU1 | 30,900 | 18,850 |
| ISU2 | 35,900-49,100 | 21,900-30,000 |
| ISU3 | 23,500-31,800 | 15,500-21,000 |

Table 5.4 Ratios of measured hoop strains to measured longitudinal strains.

| Strain Ratio | Inflection Point | Crest |
|--------------|---------------------|---------------------|
| ISU1SL | 0.38 ^{a,b} | 0.15 ^{a,b} |
| ISU1F | 0.16 ^{a,b} | 0.22 ^{a,b} |
| ISU2SL | 0.39 | 0.37 |
| ISU2F | 0.50 ^a | 0.40 ^a |
| ISU3SL | -0.42 ^b | -0.40 ^b |
| ISU3F | 0.40 ^{a,c} | 0.50 ^{a,c} |

^a variable; average value shown

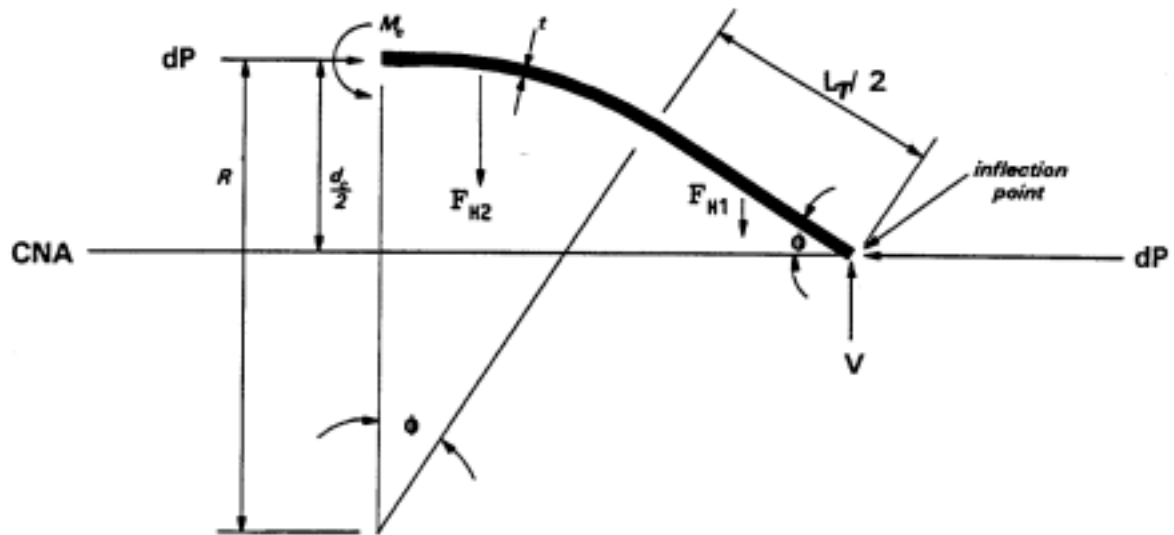
^b possibly influenced by local load effects

6. THEORY FOR GENERAL APPLICATION TO OTHER LARGE CMP

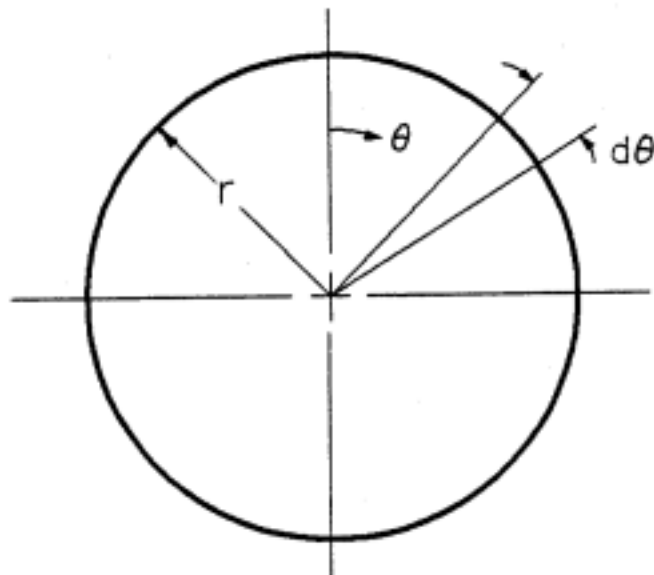
6.1. Longitudinal Moment Capacity

The measurements of longitudinal moment capacity were limited to three large diameter pipes by budget constraints; however for this study to have broader applications, an equation is needed to relate the influence of pipe diameter, steel gage, and corrugation geometry to CMP longitudinal moment capacity. To meet this need, a general equation to calculate longitudinal moment capacity for any CMP is developed based on mechanics principles and on observations from the flexural tests.

To calculate CMP moment capacity, assumptions are made about the position of load and moment acting on a section taken from the CMP corrugation. This quarter cycle is shown in the free body diagram (FBD) of Figure 6.1 and is located at the critically stressed location of the transverse section. The differential compressive forces acting on each end of the corrugation are dP and $dP + d(dP)/dx$. dP represents the differential force which, when summed around the upper one-half of the transverse cross-section, represents the strength of the compression side of the CMP. $d(dP)/dx$ is the change of force with distance along the longitudinal axis; but because $d(dP)/dx$ is small, it is not used further in the derivation. Therefore, compressive forces on both ends of the corrugation are shown as dP . M_c represents the local corrugation moment at which the outer material fibers are under the highest stress. F_{H1} and F_{H2} are downward force components on front and back sides of this longitudinal section view resulting



(a) FBD of 1/4 corrugation cycle from longitudinal section



(b) transverse cross-section view of CMP

Figure 6.1 CMP moment capacity assumptions.

from hoop stress which is resisted by the force V . M_c is calculated with the standard flexural formula:

$$M_c = \frac{\sigma I}{c} \quad (1)$$

where σ is a specified limiting stress in the longitudinal direction, c is the distance to the extreme fiber in bending ($1/2$ of the steel thickness t), and the moment of inertia (I) is equal to $st^3/12$. The arc length s is alternatively expressed as $rd\theta$ where r is the CMP radius and $d\theta$ is a differential angle of the transverse cross-section as shown in Figure 6.1b. Putting this all together:

$$M_c = \frac{\sigma \left(\frac{1}{12} r d\theta \right) t^3}{\frac{t}{2}} \quad (2)$$

Two limiting assumptions are made before calculating the vertical force components (F_{H1} and F_{H2}) due to the hoop stress. The inflection point hoop strains typically are small; however, they are assumed to be zero to simplify the computations. Also, the hoop and longitudinal strains are assumed to vary linearly with the vertical distance from the corrugation neutral axis shown in Figure 6.2b. Based on the strain assumptions, the hoop stress is zero at the inflection point and the hoop and longitudinal stresses vary linearly with distance from the corrugation neutral axis. R_{Tp} is defined as the distance from

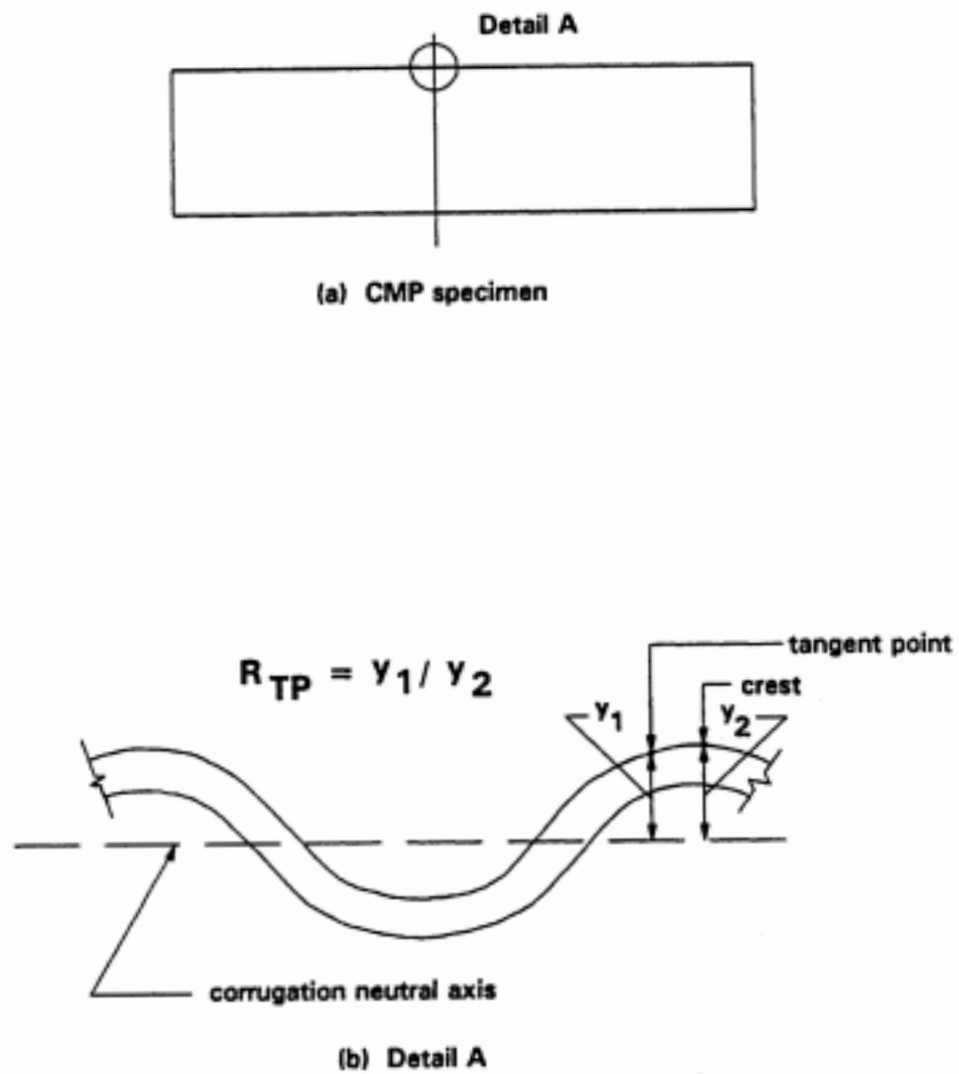


Figure 6.2 Definition of the tangent point ratio (R_{TP}).

the corrugation neutral axis (CNA) to the tangent point divided by the distance from the CNA to the crest shown in Figure 6.2b. R_{TP} is used to calculate stress at the tangent point as a function of stress at the crest. F_{H1} acts at a distance of one third of the tangent length from the inflection point times the cosine of the tangent angle, ϕ , and is expressed as:

$$F_{H1} = \frac{R_{TP} \sigma_H t L_T}{4} \left(\frac{d\theta}{2} \right) \quad (3)$$

where σ_H is the limiting hoop stress. F_{H2} is expressed as:

$$F_{H2} = \left[\int_0^\phi \sigma_{H2} t R d\alpha \right] \frac{d\theta}{2} \quad (4)$$

where $d\alpha$ is the differential angle of the longitudinal cross section, and σ_{H2} is the hoop stress acting over the curved section of the quarter cycle. σ_{H2} is :

$$\sigma_{H2} = R_{TP} \sigma_H + \frac{\sigma_H (1 - R_{TP}) R}{R(1 - \cos \phi)} [\cos(\phi - \alpha) - \cos \phi] \quad (5)$$

The moment of F_{H2} about the inflection point is as follows:

$$M_{F_{H2}} = \left[\int_0^\phi \left[\frac{s_c}{4} - R \sin(\phi - \alpha) \right] \left[R_{TP} \sigma_H + \sigma_H \frac{(1 - R_{TP})}{(1 - \cos \phi)} (\cos(\phi - \alpha) - \cos \phi) \right] t R d\alpha \right] \frac{c}{2} \quad (6)$$

where s_c is the corrugation spacing (pitch).

After integration:

$$M_{F_{H2}} = \sigma_H t R K_\lambda \frac{c\phi}{2} \quad (7)$$

where:

$$K_\lambda = \frac{s_c R_{TP} \phi}{4} + \frac{s_c \sin \phi K_0}{4} - \frac{s_c \phi \cos \phi K_0}{4} - R_{TP} R (1 - \cos \phi) - \frac{R \sin^2 \phi K_0}{2} \quad (8)$$

$$+ R \cos \phi K_0 - R \cos^2 \phi K_0 \quad (8)$$

where:

$$K_0 = \frac{1 - R_{TP}}{1 - \cos \phi} \quad (9)$$

Numerical values for K_λ of 3x1 CMP are shown in Table 6.1 with an average value of 0.3828. These values are theoretically derived as shown above and vary slightly between CMP of differing wall thickness.

With the forces and moments which act on the FBD developed,

Table 6.1 Numerical values of K_A for 3x1 CMP.

| Gage | K_A |
|------|--------|
| 20 | 0.3808 |
| 18 | 0.3812 |
| 16 | 0.3817 |
| 14 | 0.3823 |
| 12 | 0.3834 |
| 10 | 0.3846 |
| 8 | 0.3858 |

summation of moments around the inflection point yields the following expression:

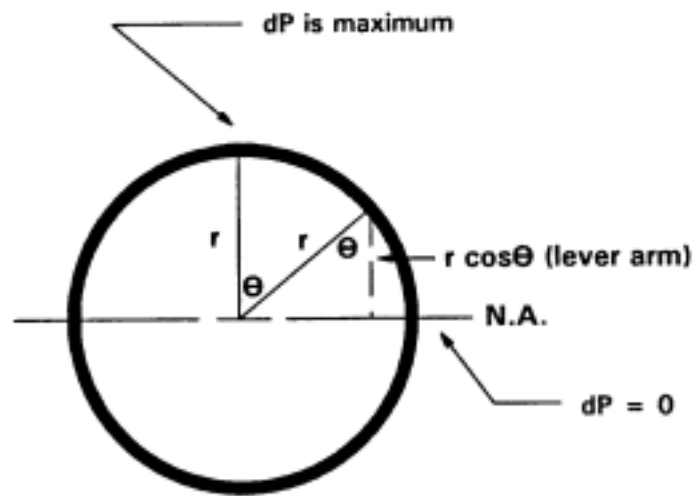
$$\sum M_{IP} = M_c - dP \left(\frac{d_c}{2} \right) + 2F_{H1} \frac{L_T \cos \phi}{3} + 2M_{F_{H2}} = 0 \quad (10)$$

Solving for dP:

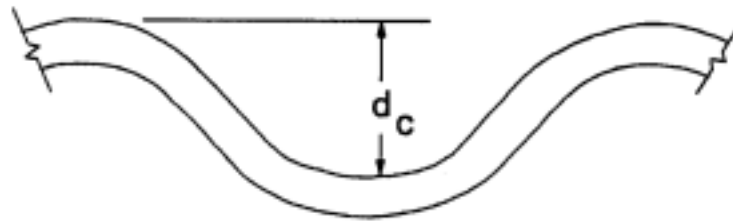
$$dP = \frac{2}{d_c} \left[M_c + 2F_{H1} \frac{L_T \cos \phi}{3} + 2M_{F_{H2}} \right] \quad (11)$$

dP is assumed to vary linearly from a maximum at the top of the CMP to a minimum at the CMP neutral axis as shown in Figure 6.3a. Therefore, the contribution of each element to the resisting moment capacity includes the term dP multiplied by its moment arm and by $\cos \theta$ to account for the linear variation of element strength which is assumed to increase with distance from the CMP neutral axis. Because the transverse cross section is symmetrical and the strength contributions of each 1/4 of the cross section are equal, the CMP differential resisting moments are integrated over 1/4 of the CMP cross section and multiplied by 4 to account for each section as shown:

$$M = 4 \int_0^{\pi/2} (r \cos \theta) (\cos \theta) (dP) \quad (12)$$



(a) transverse section view



(b) longitudinal section view of corrugation

Figure 6.3 CMP cross-section views.

The CMP moment due to a specified limiting stress, M_e , is then expressed as:

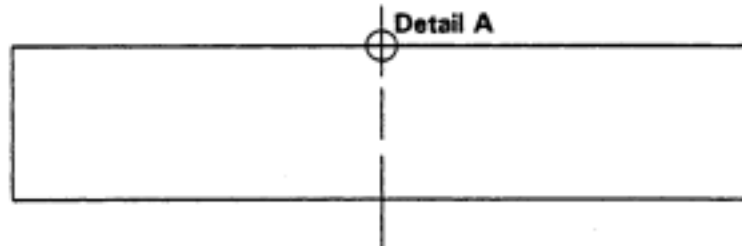
$$M_e = \frac{2\pi r t \sigma_L}{d_c} \left[\frac{r t}{6} + K_o \left(\frac{L_T^2 \cos \phi}{12} R_{TP} + K_\lambda R \right) \right] \quad (13)$$

σ_L is any limiting longitudinal stress within the elastic range which may be specified for use with this formula; yield stress has been defined as failure for the purposes of this study. K_o is the ratio of hoop stress to longitudinal stress for any CMP element and d_c is the corrugation depth as shown in Figure 6.3b.

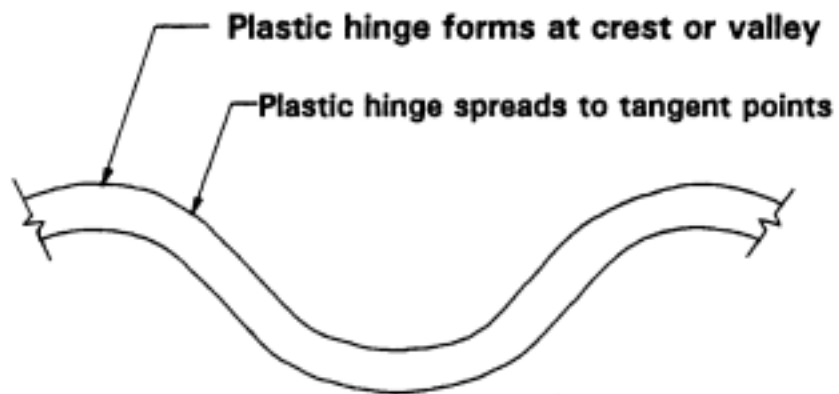
6.2. Longitudinal Ultimate Moment Capacity

Flexural failure of CMP has been defined at a limiting biaxial yield stress on the critical compression-side element; however, considerable moment capacity may exist prior to the onset of severe corrugation deflections and severe vertical deflection of the CMP. A formula is developed to calculate this ultimate moment capacity that is based in part on the previous formula to predict the longitudinal moment capacity at a limiting stress.

To estimate the ultimate moment capacity, it is inferred from the measured strains that the critically stressed element on the compression side of the CMP has yielded and formed a plastic hinge as more load is applied. This plastic hinge initiates at the crest and extends down to the tangent point at incipient collapse as shown in Figure 6.4b. Outside the region of the CMP yielding, other portions of the CMP cross-section are below yield

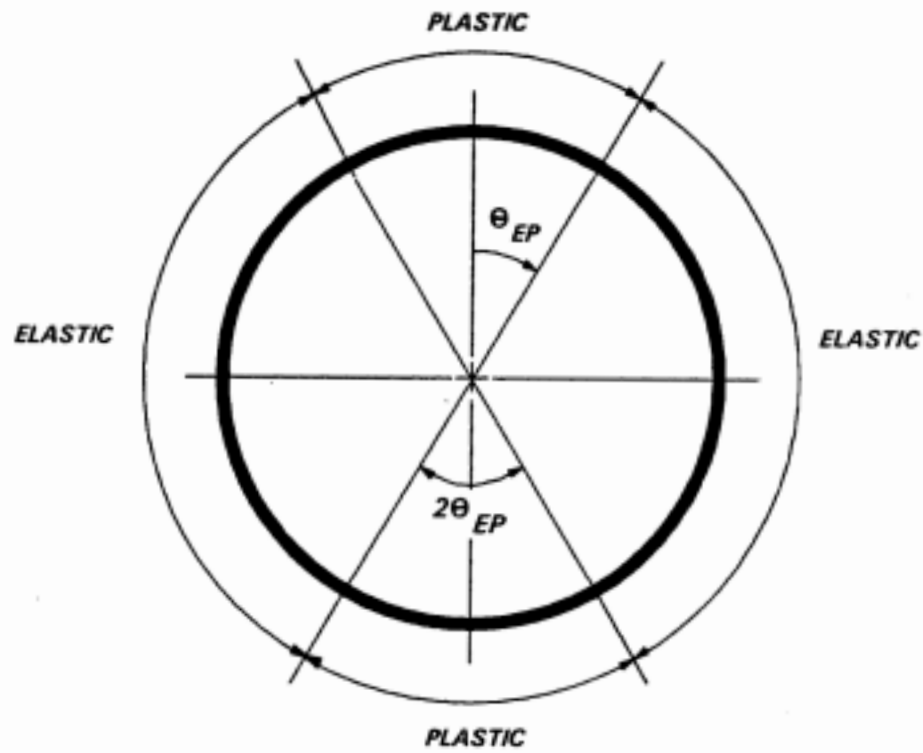


(a) CMP specimen



(b) Detail A

Figure 6.4 CMP plastic-hinge assumptions.



c) transverse section view

and behave elastically. An angle designated as θ_{EP} divides the two regions of elastic plastic behavior, as shown in Figure 6.4c. The equation for calculating the resisting moment capacity of the elastic region is a modification of the formula used in determining the limiting stress moment capacity. The resisting moment capacities of the plastic and elastic regions are developed in the following paragraphs.

Elastic Moment Contribution

As developed earlier:

$$dP = \frac{2}{d_c} [M_c + F_{H1} \frac{2 L_T \cos \phi}{3} + 2 M_{F_{H2}}] \quad (14)$$

The differential moment contribution for any element varies linearly from zero at the neutral axis to the maximum at θ_{EP} as shown in Figure 6.4c. Therefore, each differential moment term ($r \cos \theta dP$) should be multiplied by a ratio of its lever arm to the maximum lever arm ($r \cos \theta / r \cos \theta_{EP}$) prior to integration:

$$M_{E(\theta_{EP})} = 4 \int_{\theta_{EP}}^{\frac{\pi}{2}} r \cos \theta dP \frac{r \cos \theta}{r \cos \theta_{EP}} \quad (15)$$

where $M_{E(\theta EP)}$ is the elastic region moment contribution to the ultimate moment. After simplifying, $M_{E(\theta EP)}$ is expressed as:

$$M_{E(\theta EP)} = \frac{8rt\sigma_L}{d_c \cos \theta_{EP}} \left[\frac{rt}{6} + K_\sigma \left(\frac{L_T^2 \cos \phi}{12} R_{TP} + K_1 R \right) \right] \left[\frac{\pi}{4} - \frac{\theta_{EP}}{2} - \frac{\sin 2\theta_{EP}}{4} \right] \quad (16)$$

Plastic Moment Contribution

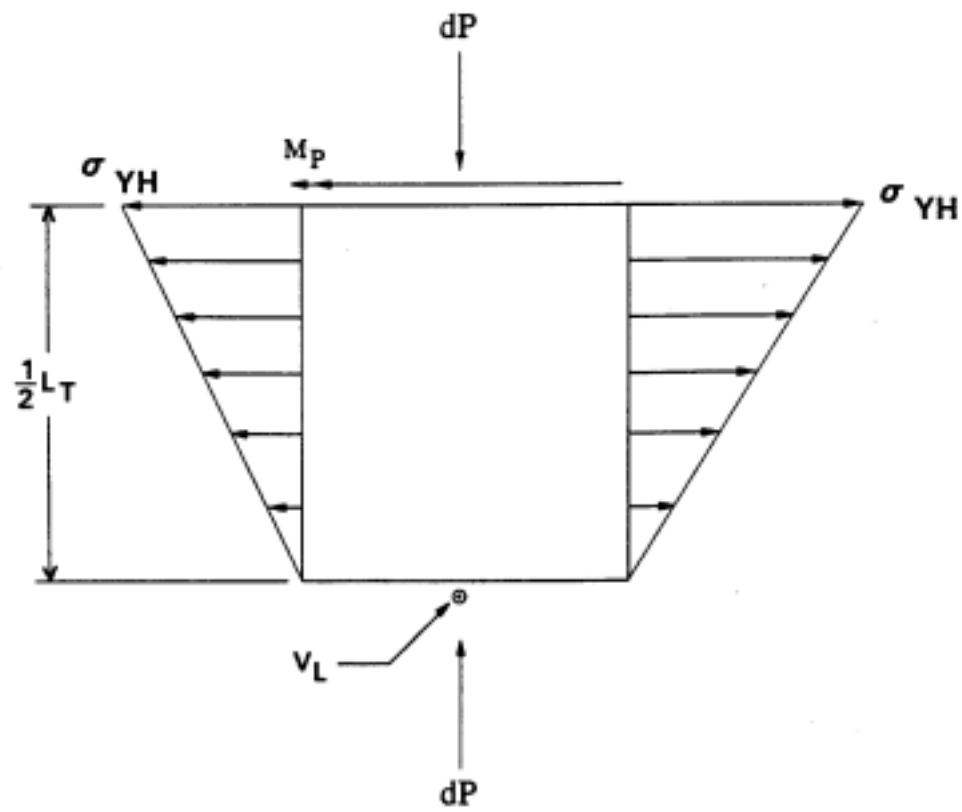
Figure 6.5a shows the assumed distribution of hoop stress in a section of the corrugation between the tangent point and the inflection point (1/2 of the tangent length). It is assumed that a plastic hinge is formed at the tangent point and that the hoop stress is at yield from the tangent point to the crest. Figure 6.6a shows the FBD's used to develop an expression for M_p in terms of σ_{YL} . M_p is the plastic hinge resisting moment within the corrugation as shown in Figure 6.5a.

$$F = \sigma_{YL} \frac{t}{2} ds = \sigma_{YL} \frac{t}{2} r d\theta \quad (17)$$

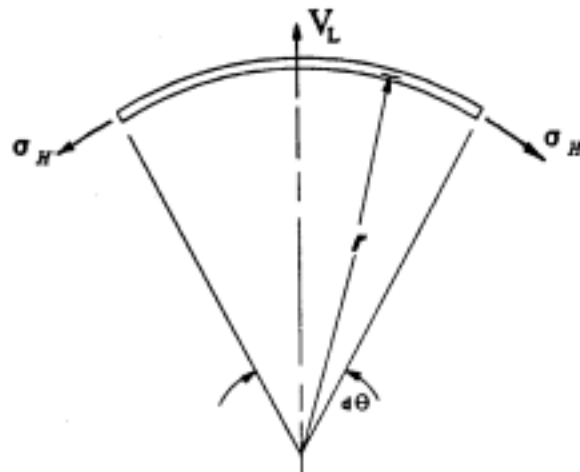
where F runs longitudinally as shown in Figure 6.6a.

$$M_p = \frac{t}{2} F = \frac{\sigma_{YL} t^2}{4} r d\theta \quad (18)$$

Before dP can be determined, F_H and V_L are related by the FBD in Figure 6.6b where it is assumed that, for equilibrium, the sum of all vertical forces is zero. F_H is the vertical force component of the hoop stress within the curved portion of the 1/4 corrugation cycle as shown in Figure 6.6c. V_L is the upward

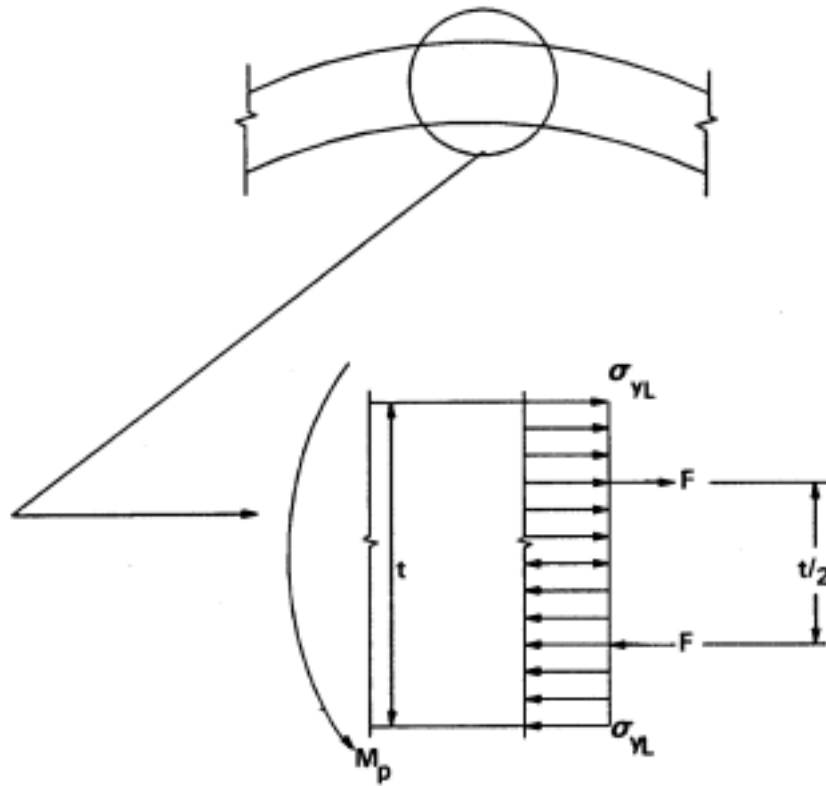


(a) plan view of linear corrugation segment

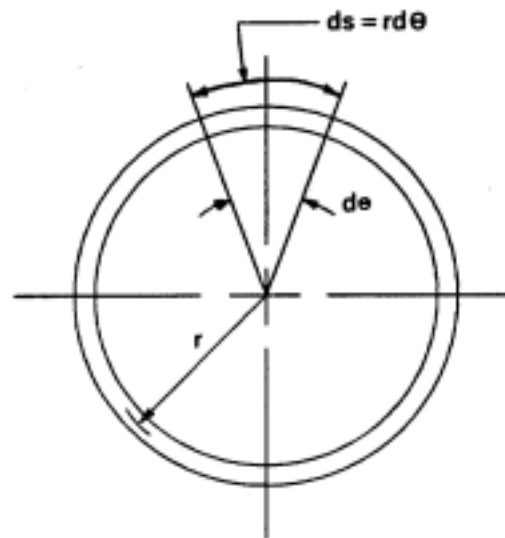


(b) end view of linear corrugation segment

Figure 6.5 Assumed distribution of hoop stress.

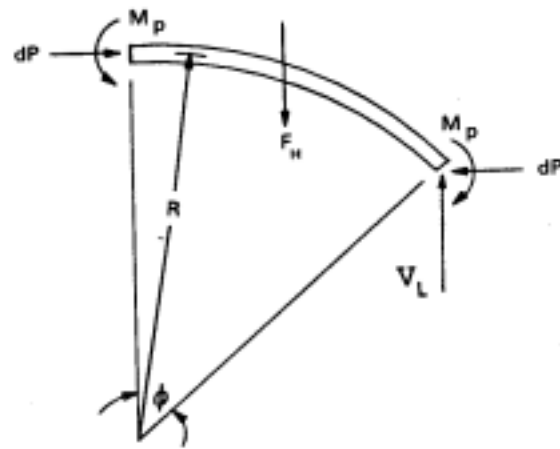


(a) FBD of plastic hinge
(longitudinal section view)

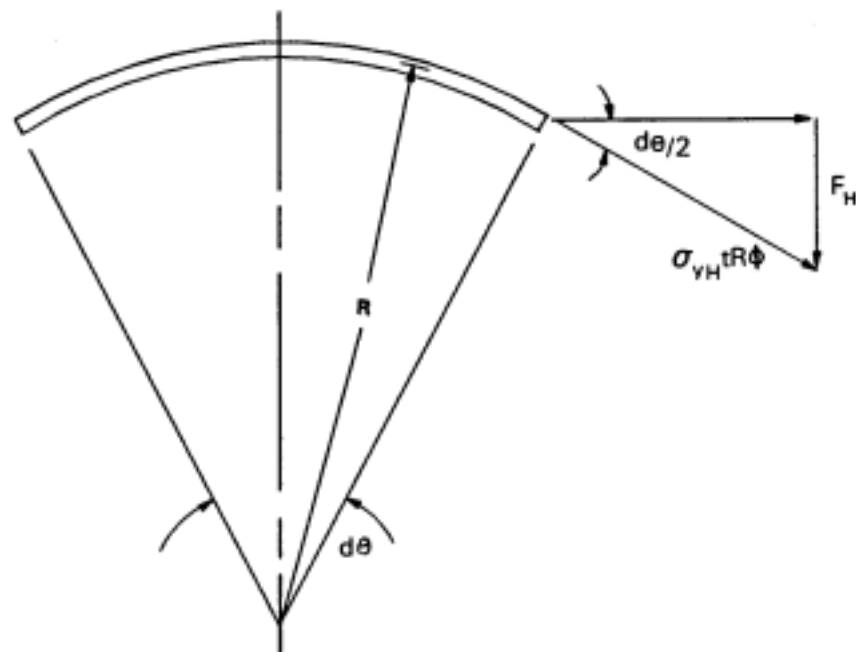


(b) relationship of arc length to transverse section angle

Figure 6.6 CMP cross-section views.



(c) longitudinal section view



(d) transverse section view

Figure 6.6 Continued.

vertical force acting at the tangent point which reacts F_H .

$$F_H = (\sigma_{YH} t R \phi) \frac{d\theta}{2} \quad (19)$$

$$V_L = 2F_H = \sigma_{YH} t R \phi d\theta \quad (20)$$

From Figure 6.7:

$$\sum M_{IP} = 0 = dP \frac{L_T}{2} \sin \phi - \sigma_{YH} t R \phi \frac{L_T}{2} \cos \phi d\theta - \frac{\sigma_{YH} t L_T}{4} \frac{L_T}{3} \cos \phi d\theta - \frac{\sigma_{YL} t^2 r}{4} d\theta \quad (21)$$

The resulting differential resisting force is:

$$dP = \frac{\sigma_{YL} t d\theta}{\sin \phi} \left[K_0 \left(R \phi + \frac{L_T}{6} \right) \cos \phi + \frac{t r}{2 L_T} \right] \quad (22)$$

The longitudinal resisting force (dP) is multiplied by its lever arm and this product is integrated from the top of the CMP down to the elasto-plastic angle (θ_{EP}). Because the transverse cross section is symmetrical and the strength contributions of each 1/4 of the cross section are equal, the CMP differential resisting moments are integrated over 1/4 of the CMP cross

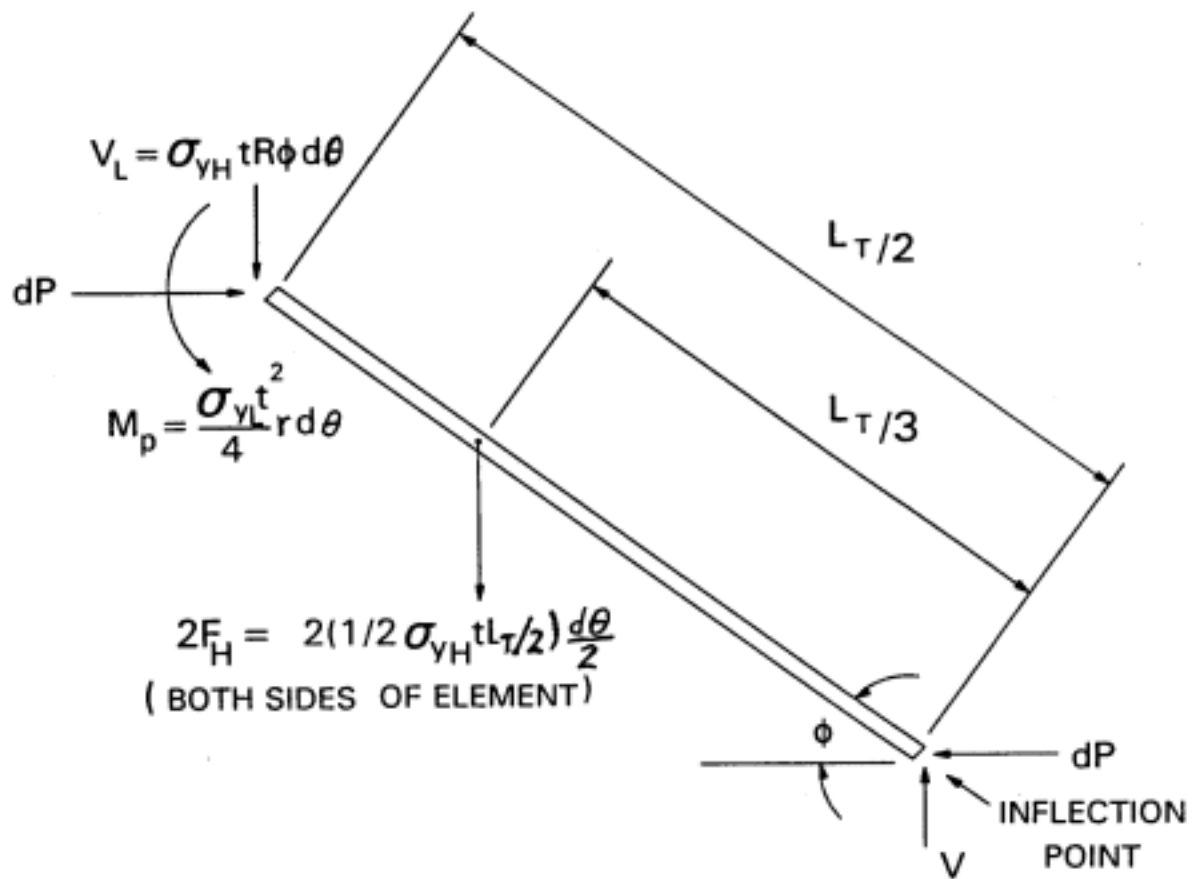


Figure 6.7 FBD of linear segment from 1/4 corrugation cycle.

section and multiplied by 4 for each section as shown:

$$M_{P(\theta_{EP})} = 4 \int_0^{\theta_{EP}} r \cos \theta dp \quad (23)$$

$$M_{P(\theta_{EP})} = \frac{4\sigma_{YL}tr}{\sin\phi} \left[K_\phi \left(R\phi + \frac{L_T}{6} \right) \cos\phi + \frac{tr}{2L_T} \right] \sin\theta_{EP} \quad (24)$$

where $M_{P(\theta_{EP})}$ is the ultimate moment contribution from the plastic region. The ultimate moment based on θ_{EP} is the sum of the resisting moments from the elastic (Equation 16) and plastic (Equation 24) parts of the CMP cross section.

$$M_{U(\theta_{EP})} = M_{P(\theta_{EP})} + M_{E(\theta_{EP})} \quad (25)$$

Using the ultimate moments obtained from the three ISU tests and setting K_ϕ equal to 0.64, θ_{EP} is calculated resulting in an average experimental value for θ_{EP} of 73.4 degrees. However, the resulting moment capacity contribution from the remaining elastic part of the cross-section is small in comparison to the moment capacity contribution from the plastic part of the cross-section. With the assumption that the entire cross-section is subject to plastic deformation ($\theta_{EP}=90$ degrees), the ultimate moment

capacity simplifies to the following revised formula:

$$M_U = \frac{4\sigma_{YL}tr}{\sin\phi} \left[K_0 \left(R\phi + \frac{L_T}{6} \right) \cos\phi + \frac{tr}{2L_T} \right] \quad (26)$$

6.3 Theoretical CMP EI Factor

To calculate CMP vertical deflections, an EI term is needed. Where E is the modulus of elasticity (E) of steel and I is the moment of inertia which is a function of the CMP geometry. However, calculation of I becomes complex because the CMP transverse cross-section is not constant in the longitudinal direction. The moment of inertia, I, for CMP is considerably smaller than the I for smooth-wall pipe ($I = \pi r^3 t$), because the smooth wall has a constant transverse cross-section which is much stiffer due to the differing CMP wall geometries as shown in Figure 6.8. To develop an expression for I, an energy approach known as the unit load method is used to relate the applied load and the CMP mid-span vertical deflection. This relationship applies to simple-span beams under uniform distributed load:

$$\Delta_v = \frac{5wL^4}{384EI} + \frac{k_z wL^2}{8GA} \quad (27)$$

where Δ_v is the vertical mid-span deflection, w is the uniformly distributed load on the CMP, L is the length of the CMP between support points, k_z is a factor to account for variation of transverse shear stresses over the cross-section, A is the steel

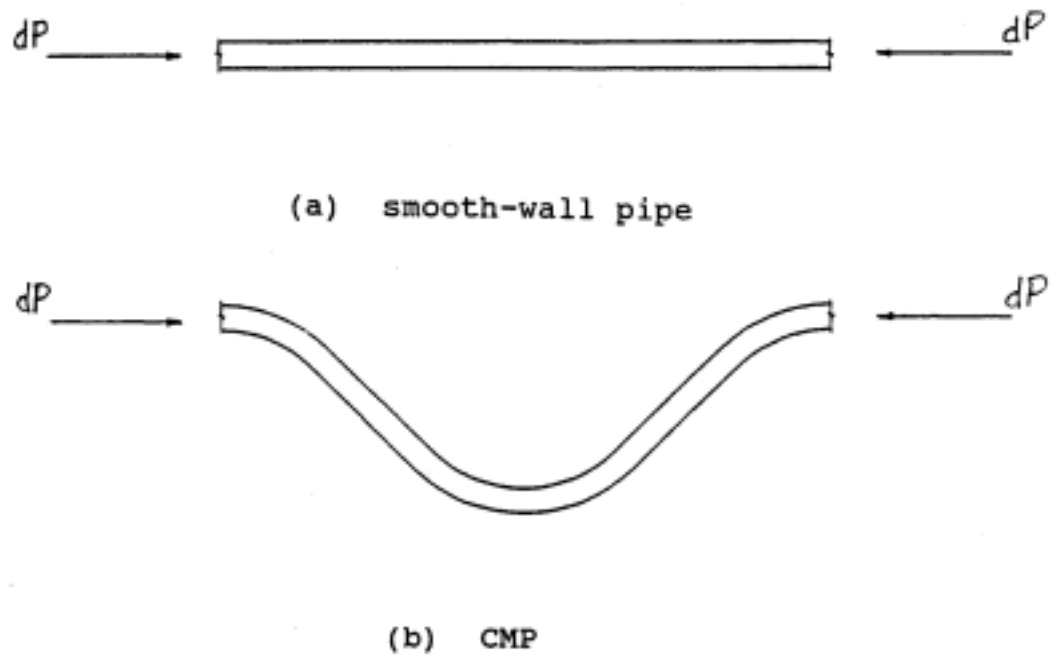


Figure 6.8 Comparison between smooth-wall pipe and CMP.

cross-sectional area, and G is the modulus of rigidity for steel. However, the deflection term due to shear ($k_s w L^2 / 8GA$) is small in comparison to the deflection term due to moment ($5wL^4 / 384EI$) and is not considered in the analysis. Exclusion of the deflection due to shear term introduced a maximum error of approximately 0.3% for Test 3 and smaller errors for the other two tests.

Before quantifying the energy in the CMP, assumptions need to be made about the distribution of stresses throughout the pipe. The loading produces a moment on the CMP such that the critically stressed element on the compression side of the CMP is at a specified limiting stress within the elastic range. It is assumed that all other elements in the CMP wall are at stress levels lower than the aforementioned limiting stress. Stress at these locations is quantified by four factors (K_1 through K_4) which are multipliers for the limiting stress. Each factor is a ratio of the distance from a location of assumed zero stress to the element divided by the distance from a location of assumed zero stress to the highest stressed element. The four factors are:

- 1) $K_1 = M / M_{MAX}$ where $M=0$ at the end supports, $M=M_{MAX}$ at the mid-span, and M varies as a second order curve between these

locations (see Figure 6.9a):

$$M = \frac{WLX}{2} - \frac{WX^2}{2} \quad (28)$$

where the x-axis runs longitudinally.

2) $K_2 = d_{CNA} / (1/2 d_c)$ where $d_{CNA} = 0$ at the inflection point (on the corrugation neutral axis), $d_{CNA} = 1/2 d_c$ at corrugation crests and valleys, and d_{CNA} varies linearly with the vertical distance from the CNA (see Figure 6.9b)

3) $K_3 = r \cos \theta / r = \cos \theta$ where $K_3 = 1$ at the CMP neutral axis ($\cos \theta = 0$), $K_3 = 0$ at the top and bottom longitudinal centerline of the CMP ($\cos \theta = 1$), and K_3 varies linearly between the two limits (see Figure 6.10a)

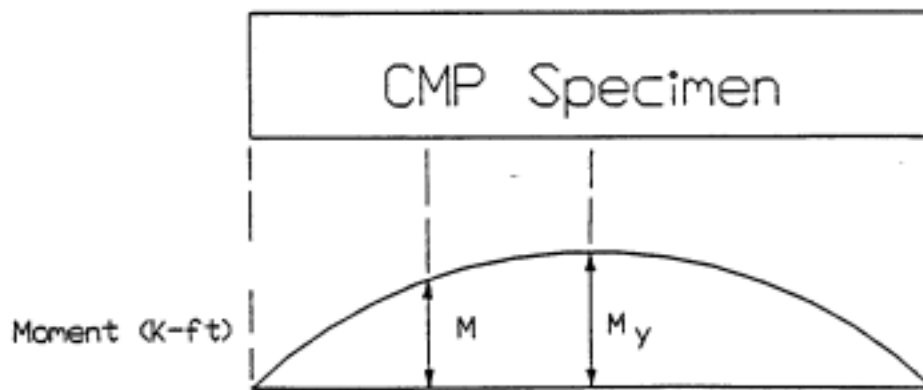
4a) $K_4 = y / (1/2)t$ where $y = 0$ at the steel mid-thickness, $y = (1/2)t$ at the steel surface, and y varies linearly between the two limits (applied to longitudinal stresses; see Figure 6.10b)

4b) $K_4 = t/t = 1$ where the stress is constant throughout the steel thickness (applied to hoop stresses)

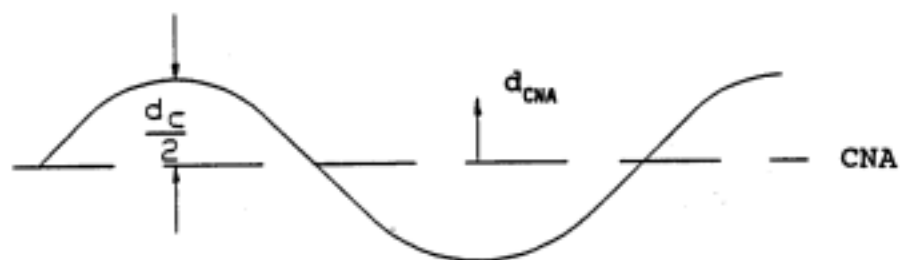
Stress at any location can now be quantified:

$$\sigma = \sigma_{MAX} K_1 K_2 K_3 K_4 \quad (29)$$

Referring to assumption 4a, longitudinal stress is assumed to vary throughout the steel thickness due to localized

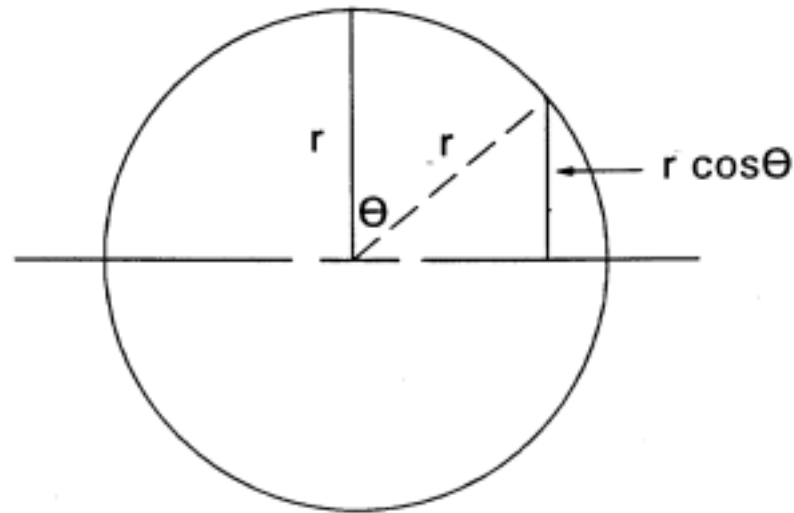


(a) ratio of moment at any section to mid-span moment

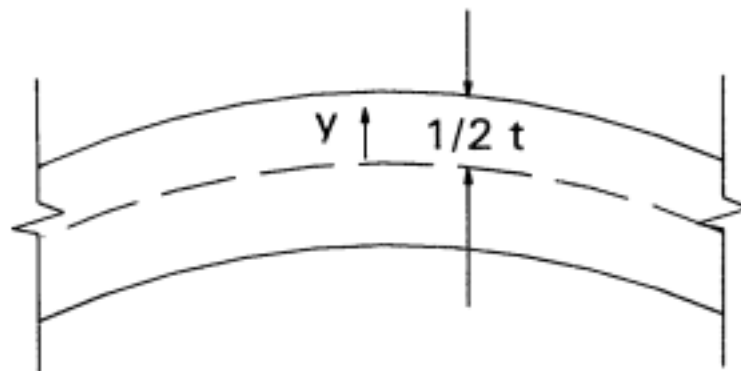


(b) ratio of the distance outward from the corrugation neutral axis to the maximum distance of $1/2$ of the corrugation depth

Figure 6.9 EI factor assumptions.



(a) ratio of lever arm for any element to maximum lever arm



(b) ratio of the distance outward from the steel mid-thickness to $1/2$ of the steel thickness

Figure 6.10 EI factor assumptions.

bending. The longitudinal stress on any element is:

$$\sigma_L = \sigma_{MAX} \left(\frac{M}{M_{MAX}} \right) \left(\frac{d_{CNA}}{\frac{1}{2}d_c} \right) \left(\frac{r \cos \theta}{r} \right) \left(\frac{y}{\frac{1}{2}t} \right) \quad (30)$$

where σ_{MAX} is oriented in the longitudinal direction.

Referring to assumption 4b, hoop stress is assumed constant throughout the steel thickness. This assumption was determined after developing the EI formula for both linearly variable and constant stress within the steel thickness. The resulting formula from both derivations were used to calculate theoretical EI factors which were compared with experimental EI factors. This comparison supported the assumption of constant hoop stress throughout the steel thickness. The resulting expression for hoop stress is:

$$\sigma = \sigma_{MAX} \left(\frac{M}{M_{MAX}} \right) \left(\frac{d_{CNA}}{\frac{1}{2}d_c} \right) \left(\frac{r \cos \theta}{r} \right) \left(\frac{t}{t} \right) \quad (31)$$

where σ_{MAX} is oriented in the hoop direction.

The principal stresses acting on each CMP element (σ_{p1} and σ_{p2}) are assumed to be the longitudinal and hoop stresses. Although this assumption is not rigorously correct for all elements, in this derivation it is used to characterize the stress distribution. It is evident that shear stresses exist on many elements oriented in the hoop and longitudinal directions, but these stresses are significantly smaller than normal stresses

due to flexure.

The generalized formulas for major and minor principal stresses (longitudinal and hoop stresses) are now used to calculate the strain energy per unit volume, U_o :

$$U_o = \frac{\sigma_{P1}^2}{2E} + \frac{\sigma_{P2}^2}{2E} = \frac{\sigma_L^2}{2E} + \frac{\sigma_H^2}{2E} \quad (32)$$

Due to the complex nature of the corrugation geometry, the strain energy per unit volume is integrated over the volume of a generic longitudinal segment of the CMP as shown in Figure 6.11. The segment has a length of 1/4 cycle in the longitudinal direction. The strain energy from all segments is then summed to calculate the strain energy (U) in the entire CMP. This equation is:

$$U = 2 \sum_{n=1}^{N_R} \int \left(\frac{\sigma_{P1}^2}{2E} + \frac{\sigma_{P2}^2}{2E} \right) dV \quad (33)$$

where $ds=rd\theta$, $dV=rd\theta dtdx$, N_R is the number of quarter cycle segments in one half of the CMP length, and n is the quarter cycle segment count number used in the summation. After

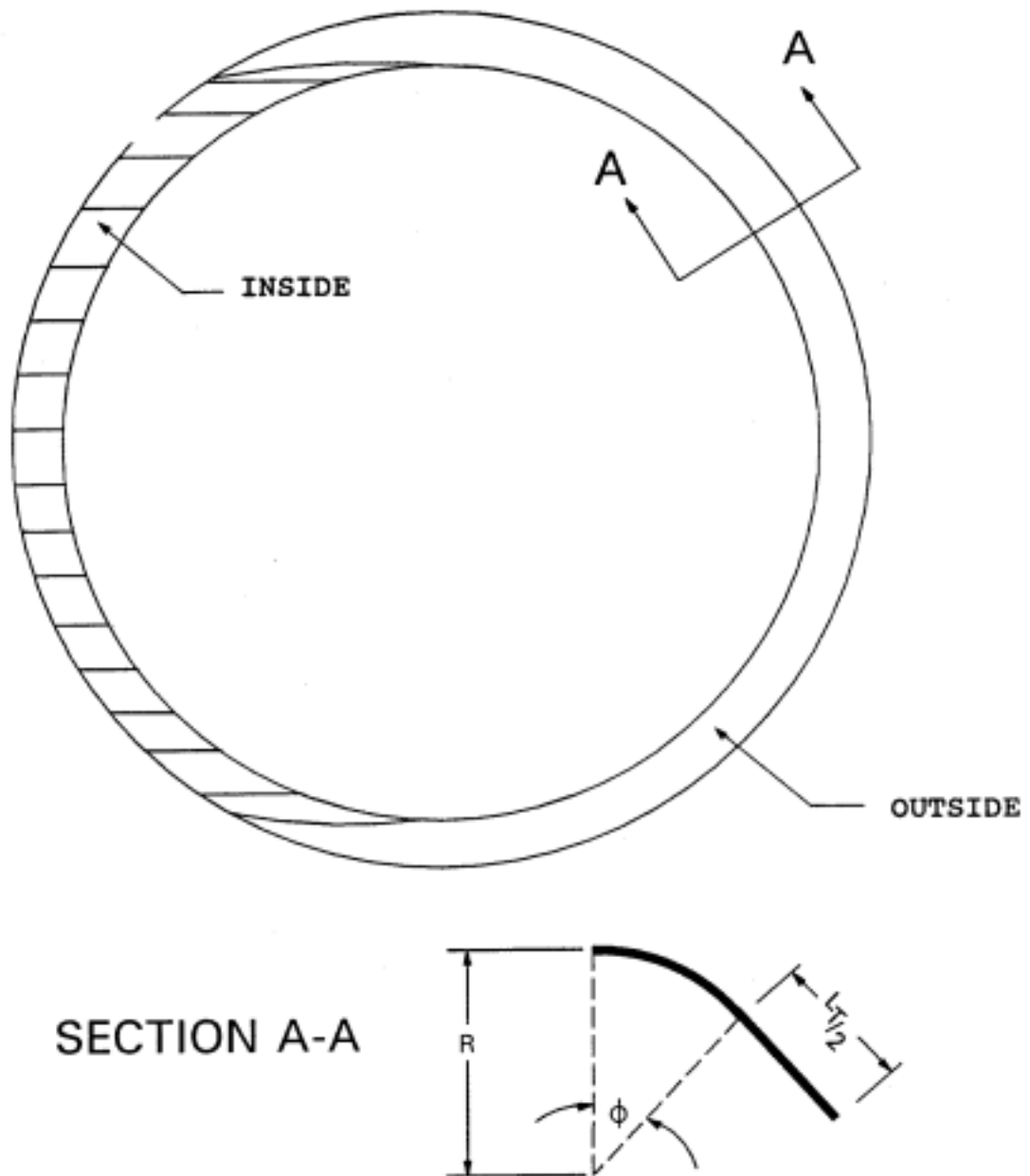


Figure 6.11 1/4 cycle length of CMP.

performing the integration:

$$U = \left[\frac{4 \sigma_{MAX}^2 K_G \pi t}{E M_{MAX}^2 d_c^2} \right] \left[\frac{1}{3} + K_G^2 \right] \int M_X^2 dx \quad (34)$$

$$\text{let } K_\psi = \left[\frac{4 \sigma_{MAX}^2 K_G \pi t}{E M_{MAX}^2 d_c^2} \right] \left[\frac{1}{3} + K_G^2 \right] \quad (35)$$

K_G is a derived geometrical parameter resulting from the energy integration and is shown:

$$K_G = (2R^2 - Rd_c + \frac{1}{4}d_c^2) R \sin \phi - \frac{1}{3}R^3 \sin^3 \phi - (R - \frac{1}{2}d_c) (\sin \phi \cos \phi + \phi) R^2 \\ + \frac{L_T^3}{24} \sin^2 \phi \cos \phi \quad (36)$$

Numerical values of K_G for CMP with 3x1 corrugations are shown in Table 6.2 with an average value of 0.09215.

Table 6.2 Numerical values of K_g for 3x1 CMP.

| Gage | K_g |
|------|---------|
| 20 | 0.09333 |
| 18 | 0.09306 |
| 16 | 0.09276 |
| 14 | 0.09243 |
| 12 | 0.09176 |
| 10 | 0.09115 |
| 8 | 0.09054 |

To find the deflection resulting from strain energy in the CMP:

$$\frac{\partial U}{\partial P} = \Delta_v = K_\psi \sum_{n=1}^{N_R} 2M_n \frac{\partial M_n}{\partial P} \quad (37)$$

A general expression for the applied moment on the CMP is:

$$M_x = \left(\frac{P+WL}{2} \right) x - \left(\frac{W}{2} \right) x^2 \quad (38)$$

where P is a fictitious concentrated load at the CMP mid-span and M_x is the moment at any distance x along the longitudinal axis.

After performing the previous summation and letting P go to zero:

$$\Delta = K_\psi \left[\frac{5WL^4}{96S_c} + \frac{WL^3}{32} + \frac{WL^2S_c}{384} \right] \quad (39)$$

From standard beam theory for a simple-span beam under uniform distributed load:

$$\Delta = \frac{5WL^4}{384EI} \quad (40)$$

Substituting:

$$\frac{5WL^4}{384EI} = K_v \left[\frac{5WL^4}{96s_c} + \frac{WL^3}{32} + \frac{WL^2s_c}{384} \right] \quad (41)$$

$$K_v EI = \left(\frac{5L^2s_c}{20L^3 + 12Ls_c + s_c^2} \right) \quad (42)$$

For most CMP specimens:

$$L^2 \gg Ls_c \gg s_c^2$$

Thus, the last two terms in the denominator on the right-hand side of Equation 42 may be assumed to be zero. Considering the lengths of CMP used in the field and corrugation styles, this assumption (ie. $Ls_c=0$ and $s_c^2=0$) introduces an error of less than 1%. Therefore:

$$EI = \frac{s_c}{4} \left[\frac{M_{MAX}^2 E d_c^2}{4\sigma_{MAX}^2 r K_v \pi t} \right] \left[\frac{3}{1+3K_v^2} \right] \quad (43)$$

Recalling Equation 13:

$$\frac{M_{MAX}}{\sigma_{MAX}} = \frac{2\pi r t}{d_c} \left[\frac{r t}{6} + K_v (R_{TP} \frac{L_T^2 \cos \phi}{12} + K_1 R) \right] \quad (44)$$

Substituting $(M_{MAX}/\sigma_{MAX})^2$ to express EI in final form:

$$EI = \frac{E\pi s_c r t}{4K_g} \left[\frac{3}{1+3K_g^2} \right] \left[\frac{rt}{6} + K_g \left(\frac{L_r^3 \sin\phi \cos\phi}{12d_c} + K_A R \right) \right]^2 \quad (45)$$

As discussed previously, E can be divided out to leave the remaining expression for the CMP moment of inertia.

6.4. Large Deflection Considerations

Large corrugation deflections do not seem to occur prior to collapse; thus, most likely they do not have a significant effect on the moment capacity of the CMP. This is evidenced by test data showing changes in corrugation crest spacings at mid-span on the compression side of the CMP as shown in Figure 6.12. These length changes, which are averaged over a nominal gage length of 6 inches, indicate that corrugation movements are small enough so that the repositioning of local compressive forces acting on the corrugation is insignificant. After collapse, the pipe is subject to relatively large corrugation movements.

6.5 Diameter Change Effects

Vertical and horizontal mid-span diameter changes are shown in Figures 6.13 and 6.14. Figure 6.13 includes all tests where the diameters increased; due either to placement of sand on the top (horizontal diameter increase) or placement of water in the CMP (vertical diameter increase). Figure 6.14 includes all tests where the diameters decreased; due either to placement of sand on the top (vertical diameter decrease) or placement of water in the CMP (horizontal diameter decrease). As shown in the figures, the

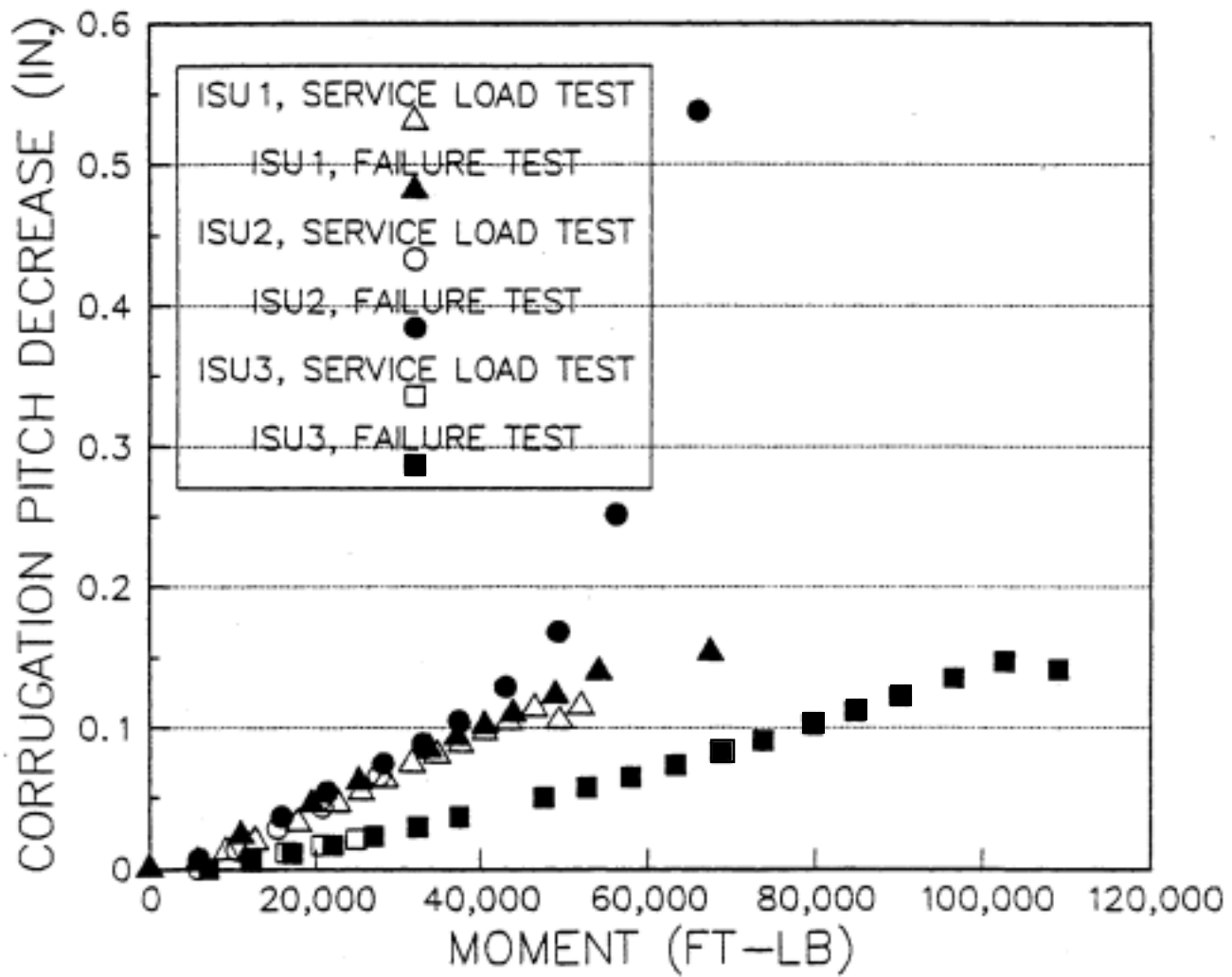


Figure 6.12 Corrugation pitch decrease as measured by DCDT#1 (DCDT is shown in Figure 4.11b).

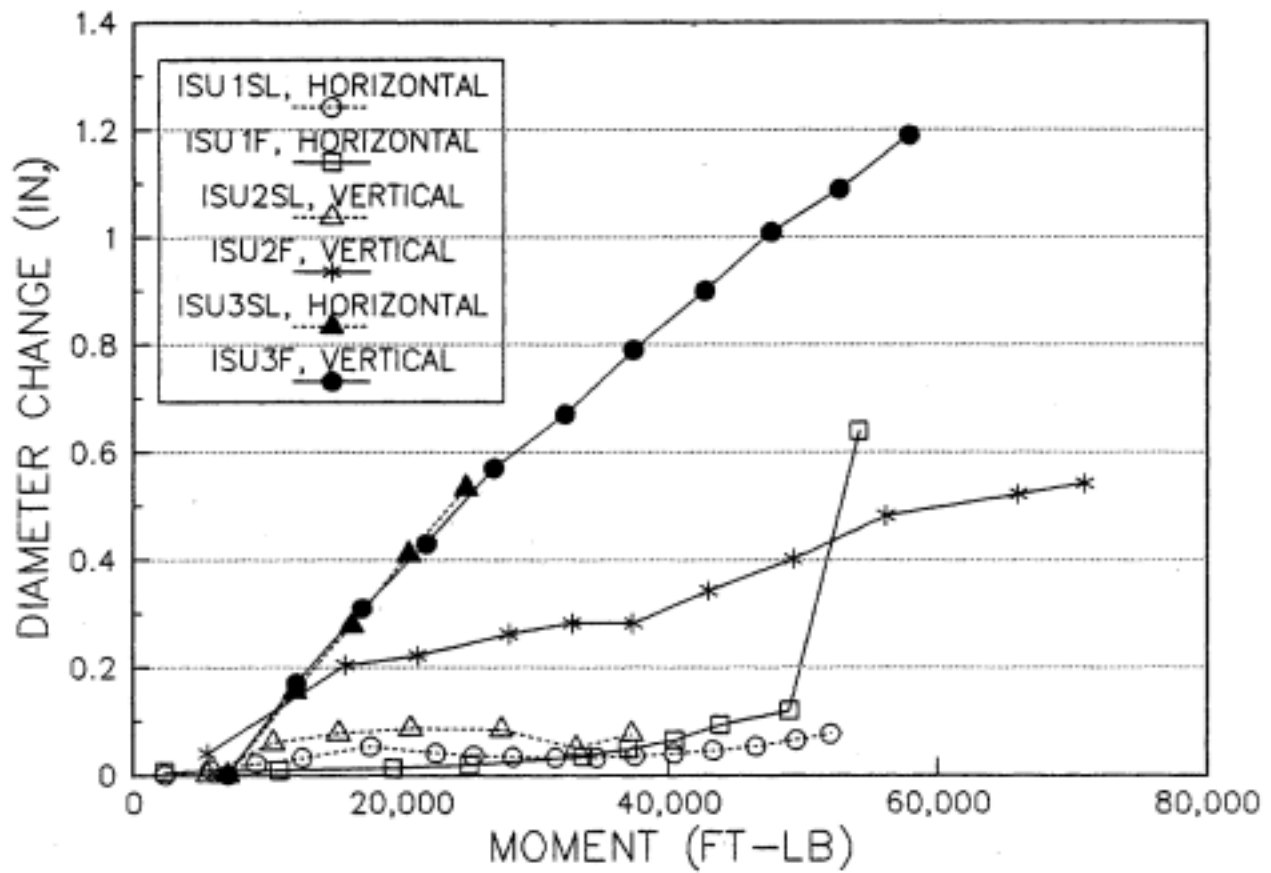


Figure 6.13 Moment vs. CMP diameter increase.

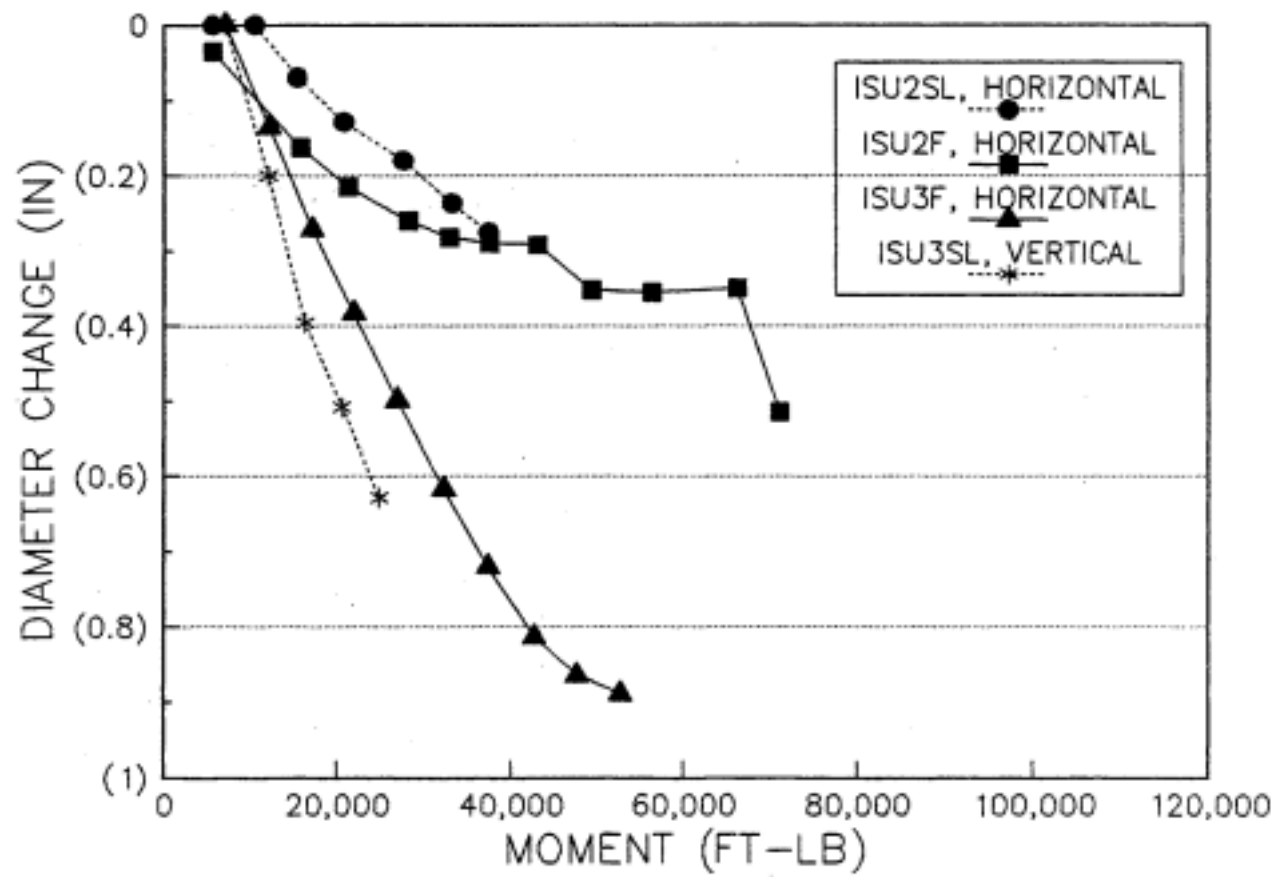


Figure 6.14 Moment vs. CMP diameter decrease.

diameter changes are increasing exponentially with CMP diameter. This is consistent with the general trends shown in Young, 1989, for rings supported by slightly different support methods.

6.6. Helix Angle Effects

The helix angle of CMP varies from approximately 33 degrees for small diameter specimens to 6 degrees for large diameter specimens, with variation due also to corrugation style and manufacturer. It was postulated by Lane (1965) that CMP with helix angles less than 8 degrees will act similar to pipes with annular corrugations. For this reason, test results are not modified for helix angle effects as their helix angle of 10 degrees is not appreciably larger than 8 degrees. Also, the development of formulas for longitudinal moment capacity and stiffness, which is based on the aforementioned tests, assumes circumferential corrugations even though the corrugations were helical. Neglecting the helix angle effects should be conservative, because the beam strength of helical pipe of equal size and gage is greater than that of annular CMP due to the shallower corrugations and the diagonal direction of the corrugations (Armco, 1955).

6.7. Comparison of Experimental and Theoretical Results

The theoretical formula predicted non-conservative yield moments for the three ISU specimens as shown in Table 6.3. Disagreement between experimental and theoretical could be described either as insignificant or important, depending on limit of the range of experimental values. Also, significant variations in yield strength between specimens will affect the agreement with the theoretical yield moments.

Ultimate moment capacity calculated by the theoretical formula is in reasonable agreement with the experimental results as shown in Table 6.4. However, this agreement is somewhat artificial because the assumption of a value for θ_{ep} is a result of knowledge gained from the experimental results.

The EI factor formula provides reasonable agreement with the test data for Tests 1 and 2 as shown in Table 6.5. This formula does not agree well with the laboratory results for the third test. However, there may be some bias in the experimentally determined EI factor due to end effects from the diaphragms and distortion of the CMP cross-section. All EI factors calculated with the theoretical formula are conservative with respect to the actual test results.

Table 6.3 Comparison of yield moment values: theoretical vs. experimental.

| Test | Experimental Yield Moment (k-ft) | Theoretical Yield Moment (k-ft) | Difference from experimental (%) |
|------|----------------------------------------|---------------------------------------|-------------------------------------------|
| ISU1 | 22.6 | 25.4 | +12.4 |
| ISU2 | 20.7-27.5 | 28.7 | +4.4 to +38.6 |
| ISU3 | 32.3-42.7 | 47.7 | +11.7 to +47.7 |

Table 6.4 Comparison of ultimate moment values (assuming $\theta_{EP}=90$ degrees): theoretical vs. experimental.

| Test | Experimental Ultimate Moment (k-ft) | Theoretical Ultimate Moment(k-ft) | Difference from experimental (%) |
|------|-------------------------------------------|-----------------------------------------|-------------------------------------------|
| ISU1 | 67.5 | 66.5 | -1.5 |
| ISU2 | 71 | 74.0 | +4.2 |
| ISU3 | 109.1 | 126.4 | +15.9 |

Table 6.5 Comparison of EI factor values: theoretical vs. experimental.

| Test | Experimental EI factor ($\times 10^6$ in ² -lb) | Theoretical EI factor ($\times 10^6$ in ² -lb) | Difference from experimental (%) |
|------|-------------------------------------------------------------------|------------------------------------------------------------------|-------------------------------------------|
| ISU1 | 911 | 840 | -7.8 |
| ISU2 | 1060 | 994 | -17.2 |
| ISU3 | 3443 | 2062 | -40.1 |

7. FIELD TEST

7.1 Objective

In the previous phases of this investigation, analytical models were developed to estimate the longitudinal bending strength of CMP of any diameter, gage, or corrugation style. These models were based upon experimental data gathered from the load testing of three CMP. Obviously, in a typical field situation, the pipe behavior is dictated not only by its own strength characteristics but also its interaction with the surrounding soil as well. Investigation of this soil-structure interaction was the primary objective of this phase of the project. A full scale field test was conducted to obtain preliminary data and to gain insight into this interaction.

7.2 Description of Test Specimen

The CMP used for the field test was galvanized steel, 10 feet in diameter with 3 by 1 helical corrugations. Two separate sections of pipe with this corrugation style were used in constructing the 52 feet long test specimen. A section 27 feet long at the upstream end was connected to a section 25 feet long with a 10 inch wide band as shown in Figure 7.1. Each section of the pipe was 10 gage with the exception of the last 5 feet at the downstream end which was 8 gage.

7.3 Excavation and Bedding Preparation

An existing embankment of undisturbed glacial till at the ISU Spangler Geotechnical Laboratory site was excavated. The base of the trench was approximately 14 feet wide and the sides

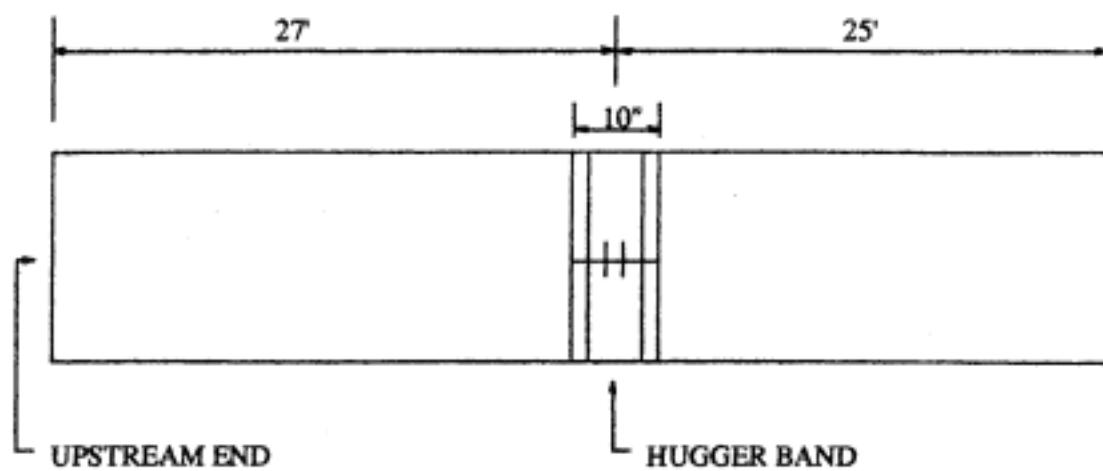


Figure 7.1 Longitudinal profile of test specimen.

of the trench were sloped at 1 horizontal to 1 vertical. Details for a Class "C" bedding were followed in preparing the base. Specifications require 10% of the pipe height to rest in a saddle cut from compacted soil or natural ground. Accordingly, after a 1 foot layer of compacted soil was constructed, a template was used to shape and check the concave saddle cut from the compacted bedding (see Figure 7.2).

7.4 Placing Pipe Sections

Each section of pipe was carefully placed in the trench with the use of a 25 ton crane. Prior to placing the pipe sections, a loose lift of soil was placed within the cradle to ensure the voids between corrugations were filled with soil. The two sections of pipe were aligned longitudinally with the aid of the concave saddle. An acceptable match between the transverse cross sections where the sections were to be connected was obtained and the three piece "Hugger Band" was placed around the two pipe ends and tightened to firmly join the two sections of pipe. Considering the loads the joint would be subjected to during the uplift test, a decision was made to strengthen the connection to prevent a premature joint failure. It was thought that without strengthening, the pipes would simply rotate at the joint with no bending stresses being transferred between the two sections of pipe. Thirty-four, 1/4 inch thick, 2.5 inch wide by 18 inch long steel plates were welded around the inside circumference of the joint. The plates were concentrated at the top and bottom of the connection because higher stresses were expected at these

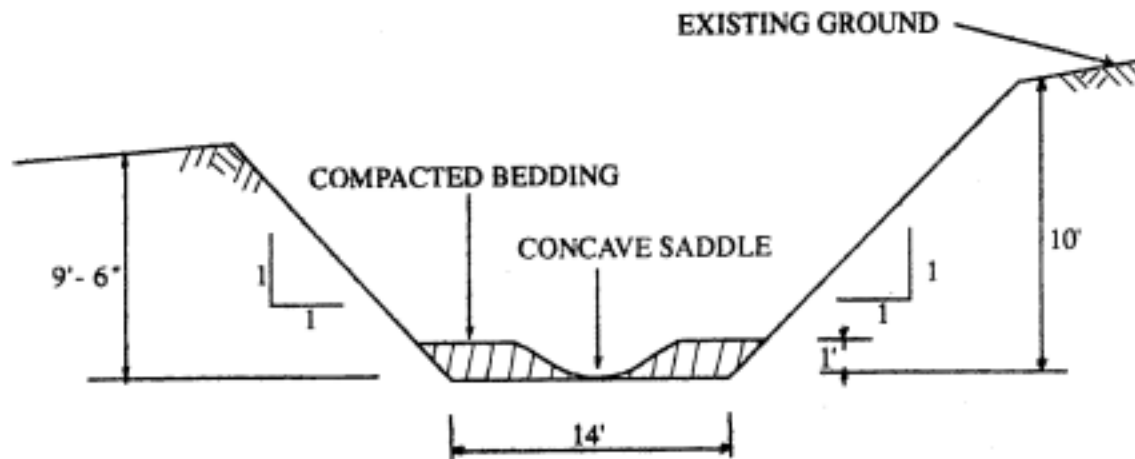


Figure 7.2 Excavation-bedding preparation (Class "C").

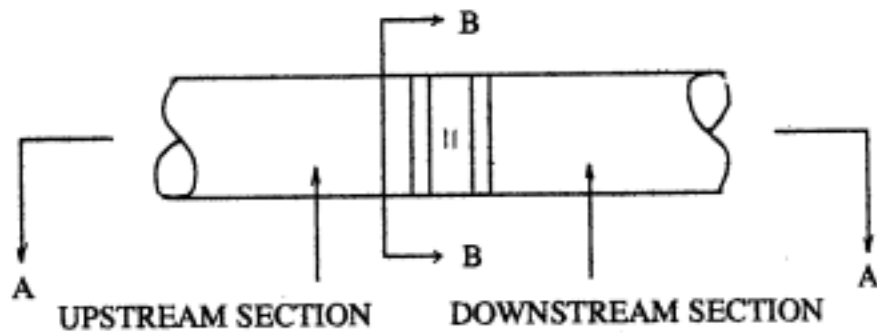
locations. A detailed illustration of the joint is shown in Figure 7.3.

7.5 Instrumentation

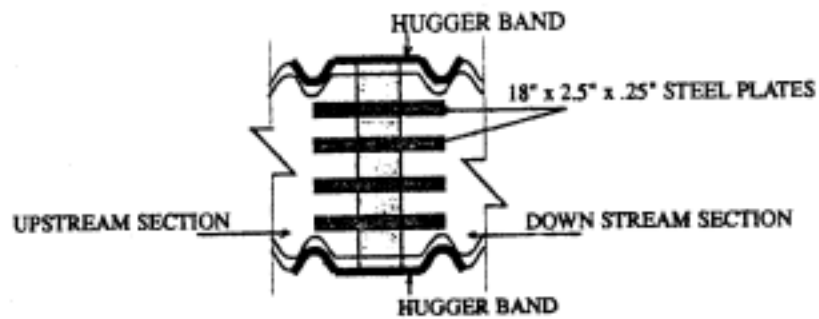
Data collected for this test included strains on the inner surface of the pipe, deformations of the pipe cross section, and pressures within the soil surrounding the pipe. Each measurement was read and recorded using a computer controlled data acquisition system (DAS) placed inside the Spangler Geotechnical Laboratory building. Data was obtained during the actual uplift test as well as during the soil backfilling. Also, vertical deflection measurements were manually monitored during the uplift portion of the test.

Six longitudinal sections (shown in Figure 7.4a) were instrumented with strain gages. Gages to measure longitudinal and hoop strains at the peaks of corrugations were placed at the top, bottom, and at both ends of the horizontal diameter at all six locations as illustrated in Figures 7.4b and 7.4c. Thus, at each instrumented section there were 8 strain gages.

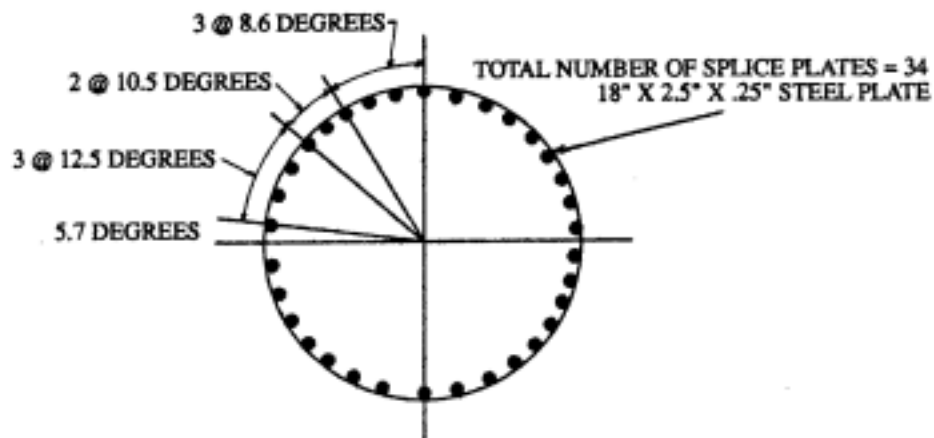
Lightweight rods with DCDT's appropriately attached were connected to the inside walls of the CMP near the same six sections that were instrumented with strain gages (see Figure 7.4a). It was necessary to slightly offset the deformation instrumentation from the strain gages to avoid introducing stress concentrations. However, for the remainder of this report, the deformation rods will be referenced according to the corresponding strain gaged sections. Horizontal deformation rods



(a) Profile of test specimen

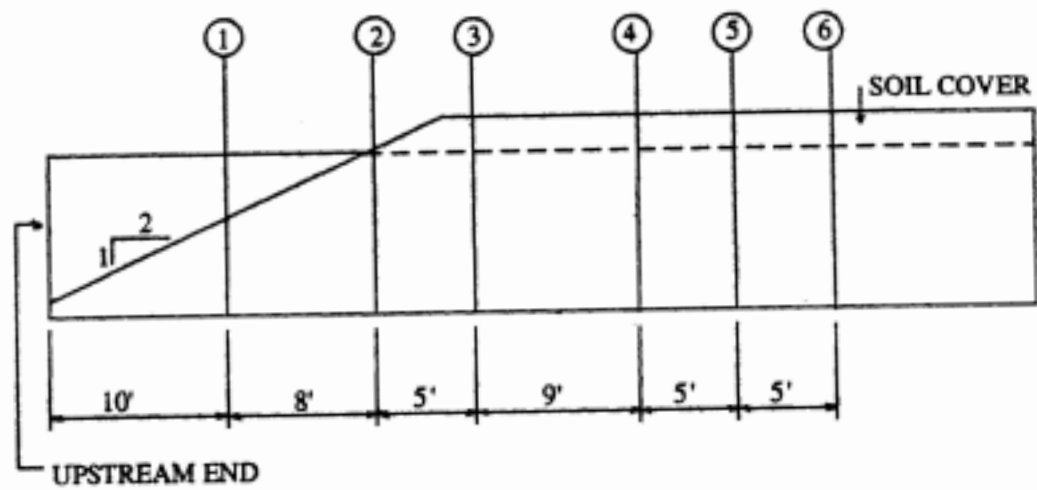


(b) Section A-A Joint detail

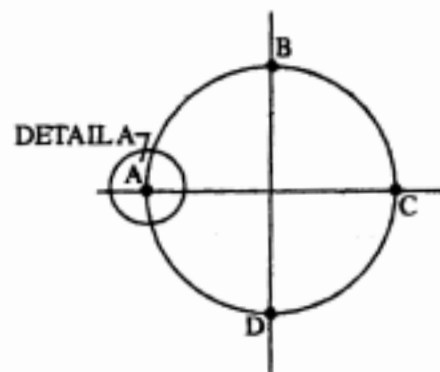


(c) Section B-B Placement of steel plates at joint

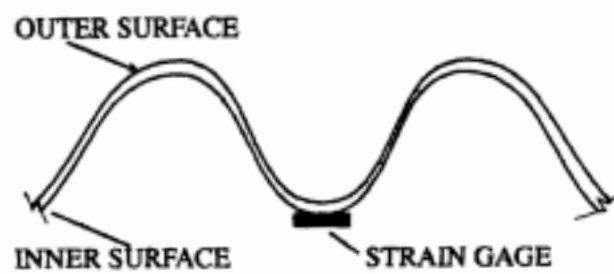
Figure 7.3 Joint details.



(a) Location of strain gaged sections



(b) Location of strain gages at each section



(c) Detail A

Figure 7.4 Placement of strain gages.

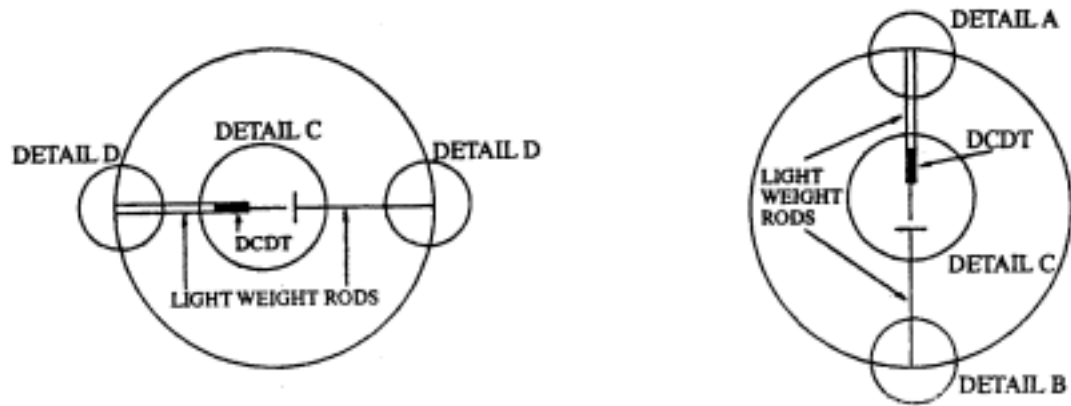
were located 6 inches downstream of the strain gaged sections while vertical diameter changes were monitored at locations 6 inches upstream of the strain gaged sections. Details of this instrumentation are shown in Figure 7.5. This instrumentation is similar to that used in the load tests of the three CMP's described in Section 4.5 and Figure 4.12 of this report.

Soil pressure cells were installed within the backfill adjacent to the pipe's horizontal diameter, directly above the CMP and adjacent to the prism of soil defined by the pipe diameter. The pressure cells were placed at Sections A, B and C as shown in Figure 7.6a. Note, Sections A and B are 2 feet beyond strain gaged Sections 2 and 3 respectively while Section C is coincident with Section 4. Specific placement of the cells at each of these sections is illustrated in Figures 7.6b, c and d.

Vertical deflections of the pipe were measured with vertical steel rods which were attached to the top of the CMP and extended above the fill at the seven locations shown in Figure 7.7a. With respect to strain gaged Section 1, Section a is 6 feet upstream, Section b is 1 foot downstream, and Section c is 5 feet downstream. Section d is 1 foot upstream of strain gaged Section 3 while Sections e, f, and g are analogous to Sections 4, 5, and 6 respectively. As detailed in Figure 7.7b, scales were attached to the rods and their movements were monitored with a transit.

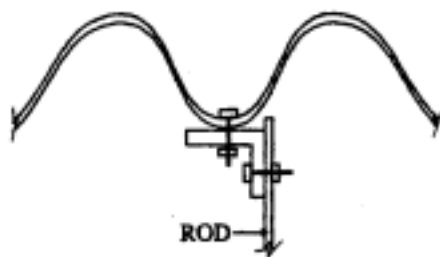
7.6 Load Frame Description

The pore pressures resulting from steady state seepage beneath the pipe, believed to be the cause of many inlet uplift

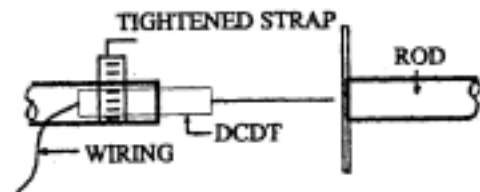


(a) Horizontal deformation bars

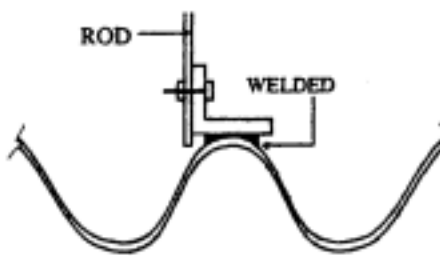
(b) Vertical deformation bars



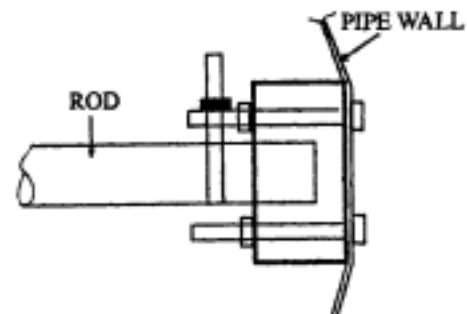
(c) Detail A



(e) Detail C

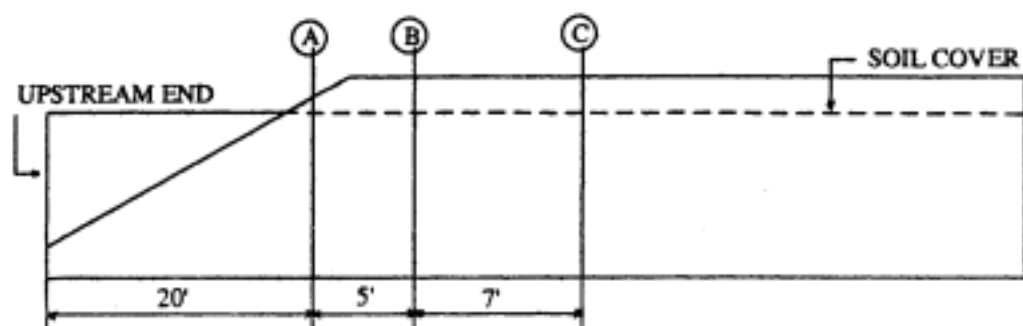


(d) Detail B

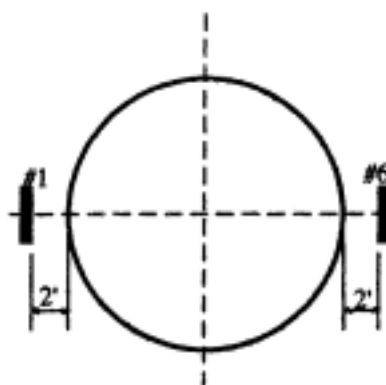


(f) Detail D

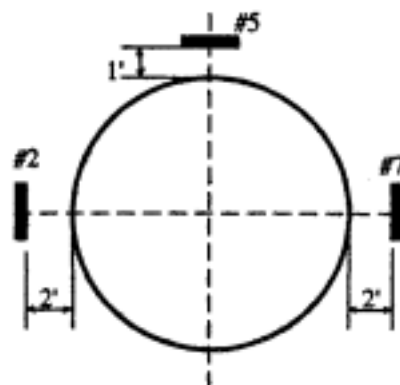
Figure 7.5 Instrumentation to measure diameter changes.



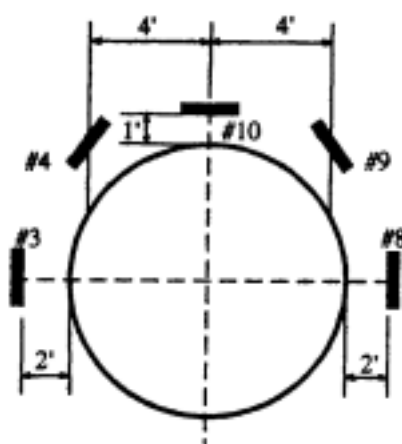
(a) Location of soil pressure cells.



(b) Section A.

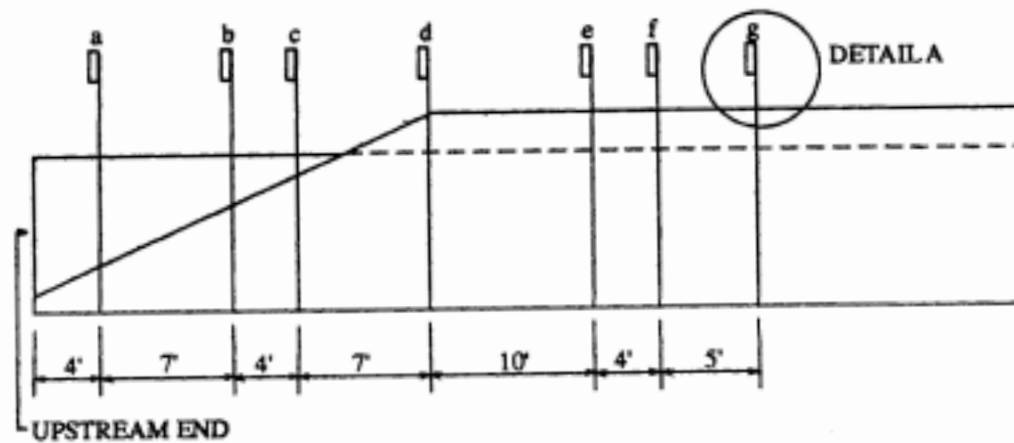


(c) Section B.

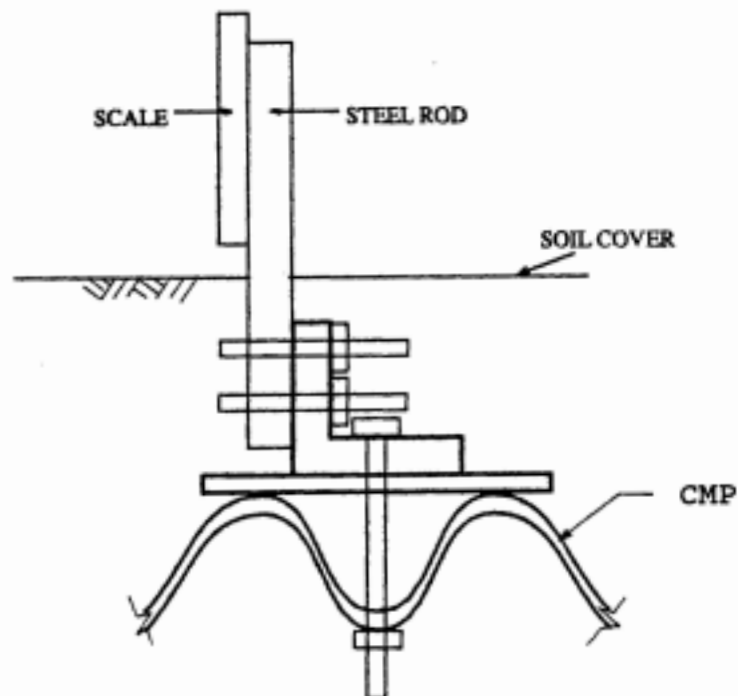


(d) Section C.

Figure 7.6 Soil pressure cell locations.



(a) Longitudinal placement of deflection rods



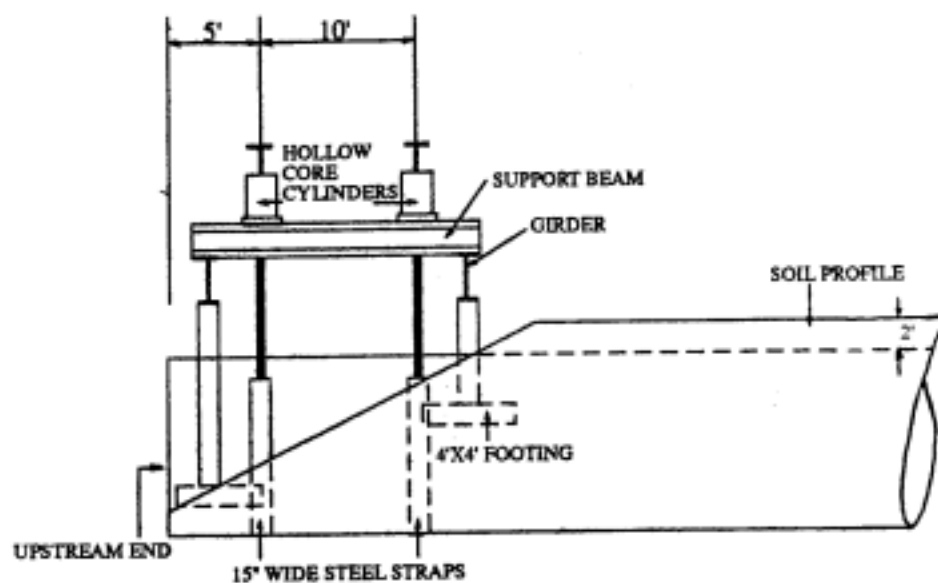
(b) Detail A

Figure 7.7 Vertical deflection rods.

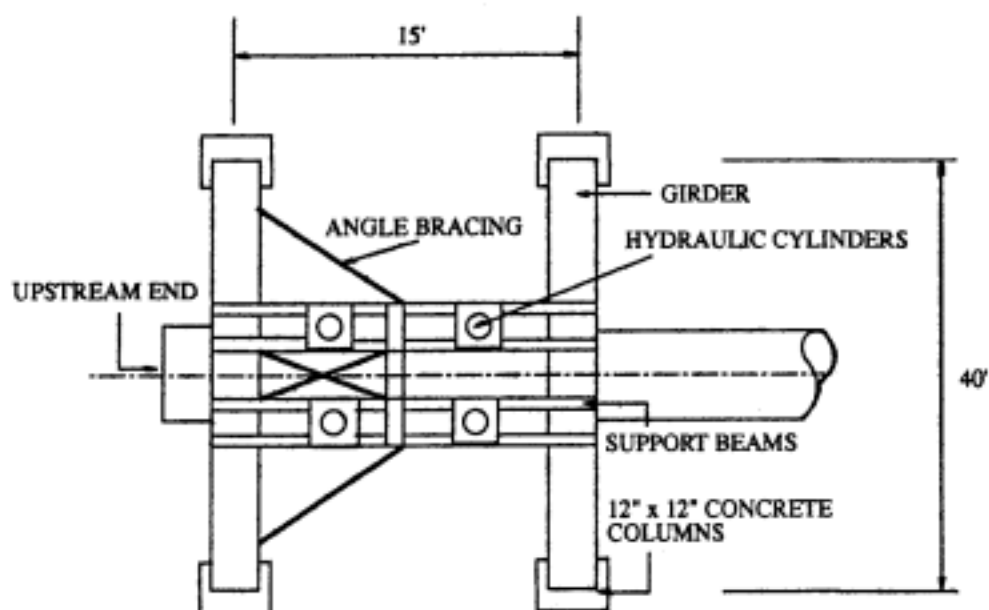
failures, were simulated with the use of two load points located 5 feet and 15 feet from the upstream end of the pipe. Uplift was provided by a set of hollow core hydraulic cylinders supported on an overhead load frame. The loads from the hydraulic cylinders were transmitted through a system of high strength rods to 15 inch wide steel straps that passed under the bottom half of the pipe. A grout mix was pumped between the straps and the pipe corrugations to ensure that the load would be distributed over the full 15 inch width thus deterring any local failures. A beam-girder system was used to transmit the hydraulic cylinder forces to four supporting columns. For stability, structural steel angles were used to brace the beam-girder system and 3/8 inch wire rope, between the girders and ground anchors, prevented lateral movement of the load frame. A detailed drawing of the load frame is shown in Figures 7.8a and 7.8b; Photographs of the test set-up are shown in Figures 7.8c and 7.8d.

7.7 Backfilling

Proper backfilling techniques require knowledge of the type of soil used as fill material and the type of structure that is being backfilled. Specifications required fill around culvert pipes to be compacted to 90% of the maximum dry density obtained from a standard proctor density test. To reach this level of compaction, the backfill material must be at or near the moisture content associated with the maximum density. Standard proctor density tests were run on two soil samples obtained from the site to determine the compaction characteristics. The test revealed a

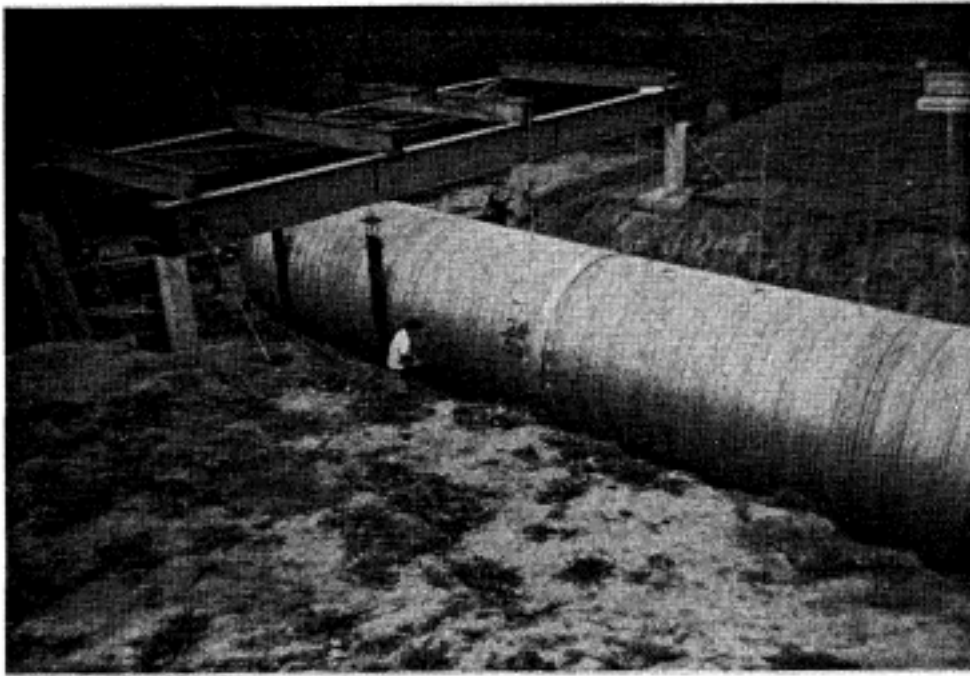


(a) Profile of load frame



(b) Plan view of load frame

Figure 7.8 Load frame description.



(c) Test setup before backfilling



(d) Test setup after backfilling

Figure 7.8 Continued.

maximum dry density of 120 pcf at a 12% moisture level.

In the beginning stages of the backfilling process, the haunch areas located near the base of the pipe were so confined that mechanical compaction equipment could not be utilized. These areas were therefore compacted by hand using 2 inch x 4 inch "studs". As the fill depth exceeded the haunch region, adequate space was available for the use of mechanical tampers. Loose lifts approximately 8 inches deep were placed and evenly spread prior to compaction. After compaction, moisture and compaction levels were checked by the sand cone method to confirm compliance with specifications. Backfilling alternated from side to side so that the two fills were kept at approximately the same elevation at all times. A typical cross section detailing the backfill process is shown in Figure 7.9. As shown in Figure 7.10, an embankment with a slope 2 horizontal to 1 vertical was formed during the backfill. This embankment started approximately 1 foot above the bottom of the pipe at the upstream end and sloped upward until a cover of 2 feet was obtained. This profile was constructed to simulate a highway embankment with minimum cover and typical foreslope.

7.8 Backfill Data

Data was recorded at six different stages of the soil backfilling process. An initial reading was taken after the haunch areas on each side of the pipe had been adequately compacted. This corresponded to a layer of soil 2 feet above the bottom of the pipe. Additional readings were taken as soil

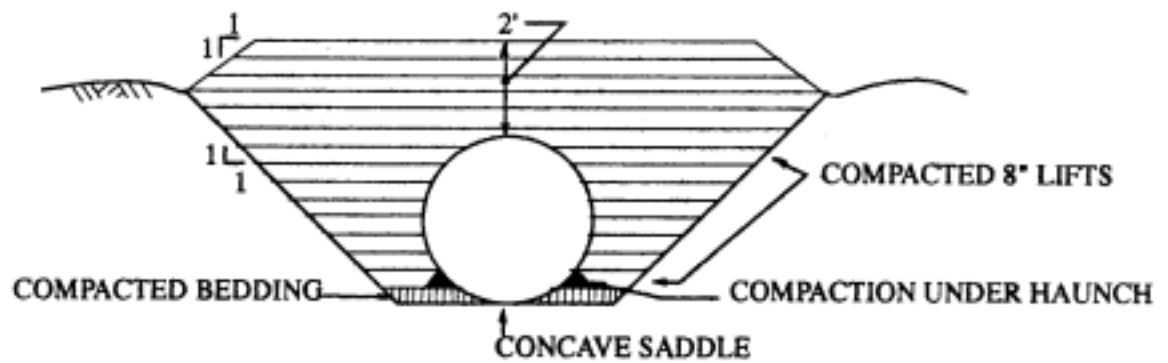
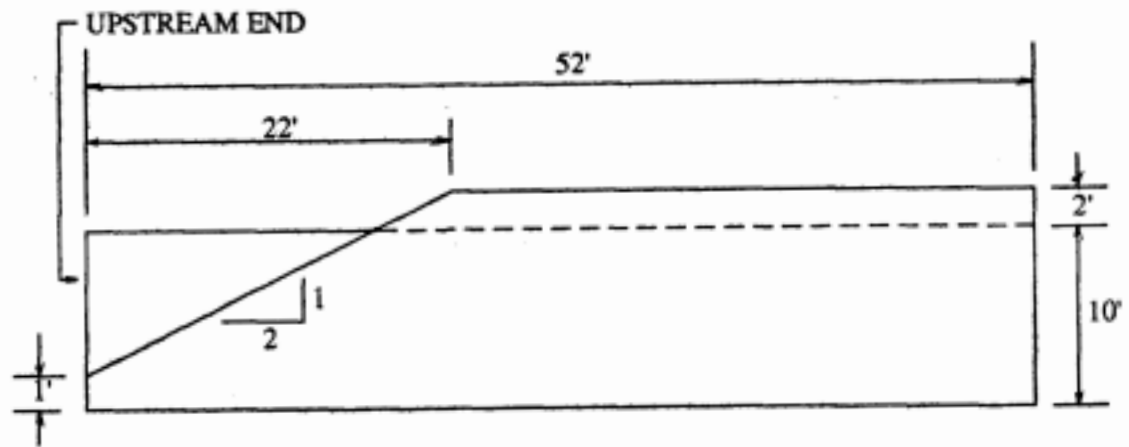
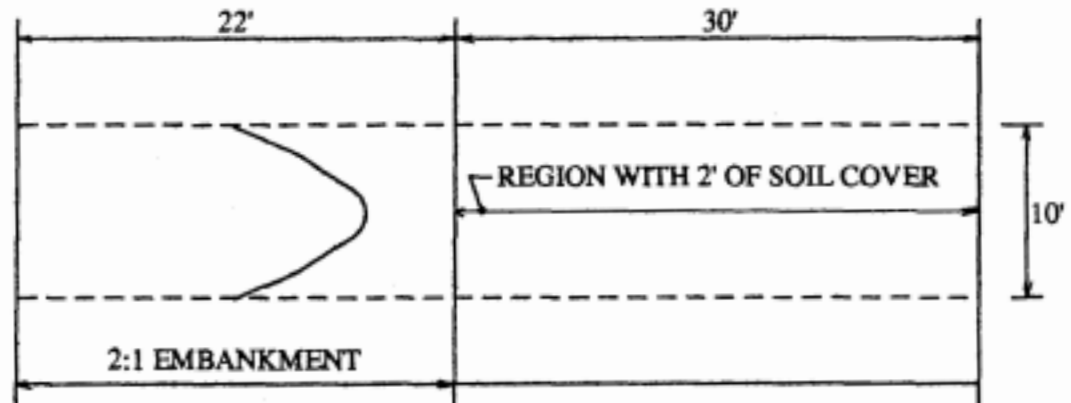


Figure 7.9 Backfill details: cross section.



(a) Profile of pipe installation



(b) Plan view of pipe installation

Figure 7.10 Backfill details: longitudinal.

levels reached 5 feet, 7 feet, 8 feet, 10 feet, and 12 feet as shown in Figure 7.11.

7.9 Backfill Results

Representative samples of data from the instrumentation used during the soil backfilling process are presented in this section. Measurements included strains on the inner surface of the pipe, horizontal and vertical diameter changes and pressures within the soil backfill. The change in values between measurements were in response to the increase in depth of fill.

Both horizontal and vertical diameter changes were monitored during the backfilling. Although some sections previously noted were not equipped with instrumentation due to the lack of available DCDT's, the majority of the sections were fully instrumented, which provided a sufficient amount of data to determine the behavior of the CMP during the backfilling process.

As the level of fill increased, changes in the CMP's cross sectional shape were evident. The compacted soil was exerting enough lateral pressure on the CMP to cause horizontal inward movements. Consequently, the top of the pipe also responded by deflecting upward. Figure 7.12 graphically illustrates these deformation patterns. Horizontal and vertical measurements are shown for Sections 2, 3 and 4 while an additional data set representing the horizontal movement at Section 6 is also shown. Observation of these particular data suggest that nearly all the deflection at a specific section occurred within the first 7 to 8 feet of fill. After reaching this level, the plots show that

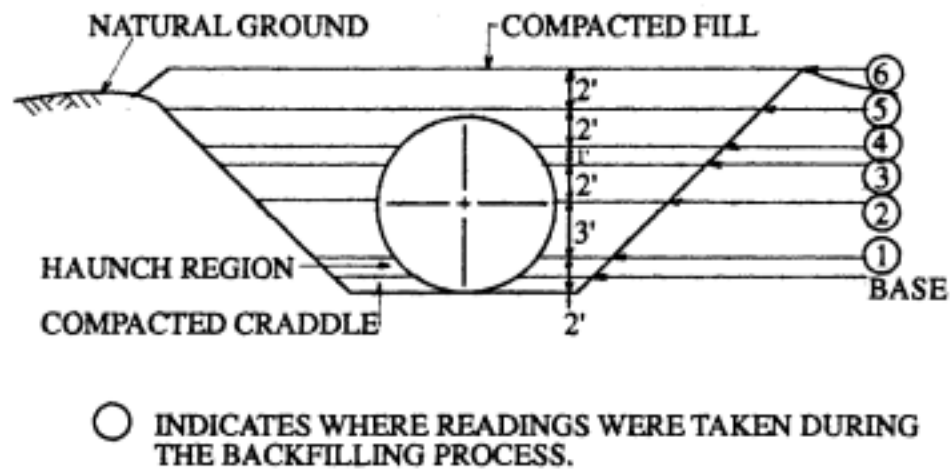
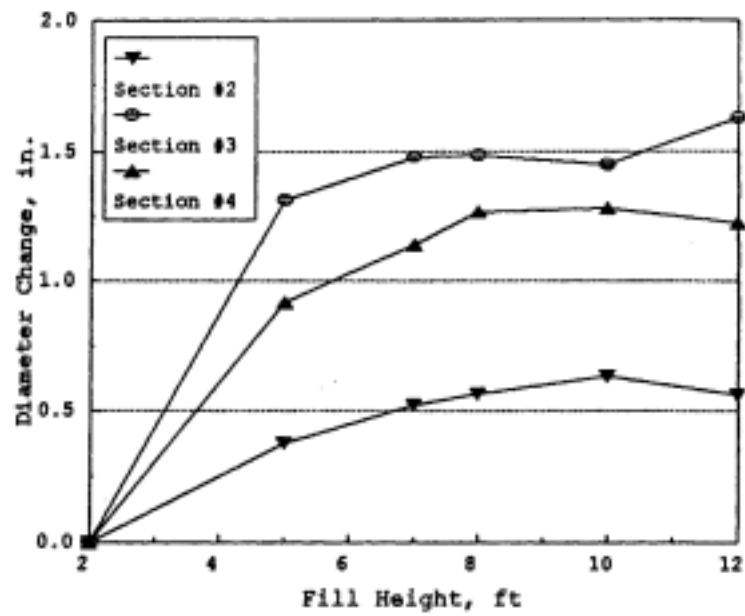
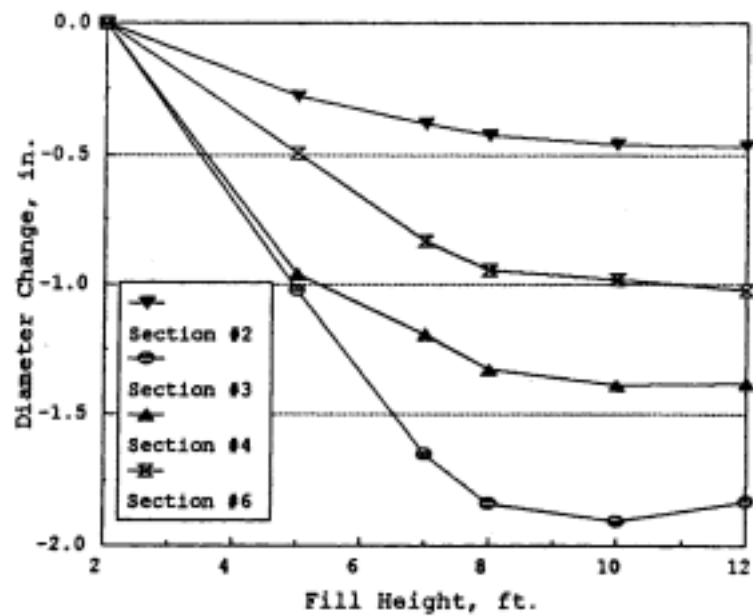


Figure 7.11 Stages of backfill where instrumentation readings were taken.



(a) Vertical diameter changes



(b) Horizontal diameter changes

Figure 7.12 Cross sectional deformations during backfilling.

additional layers of soil had little affect on the CMP's cross sectional shape. This may be attributed to the fact that a majority of the added pressure in this region of fill was acting downward on the CMP's upper surface but did not cause significant deformations because of the confinement provided by the compacted soil around the CMP.

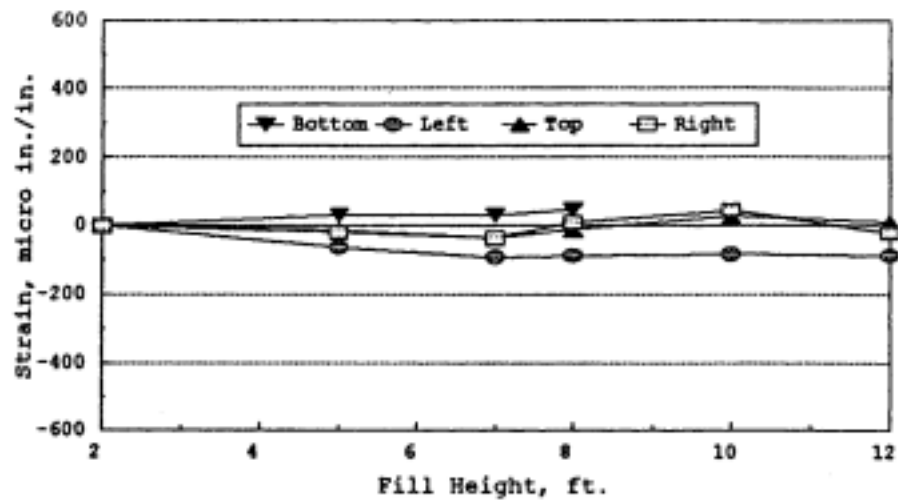
The addition of backfill material beyond the top of the CMP was expected to cause some vertical downward movement. In fact, in high fill situations, the deformation pattern discussed above is actually reversed; the pipe's crown is deflected downward while the sides of the pipe tend to move outward. In this particular case, the relatively shallow fill did not provide enough pressure to cause a complete reversal. However, observation of Figure 7.12a suggests that the onset of this behavior, marked by a slight decrease in the pipes vertical diameter, was occurring at Sections 2 and 4 during the last 2 feet of fill (10 to 12 feet).

The data show that the deformations, horizontally and vertically, for a particular section were very comparable. It was noted that the horizontal deflections at Sections 3 and 4 were slightly greater than the corresponding vertical deflections. Also, the deflections at Sections 2 and 6 appear to be significantly smaller than those at Sections 3 and 4. The smaller deflections measured at Section 2 may be attributed to the fact that Section 2 was located in the embankment region of the soil profile where the level of fill was less than that at

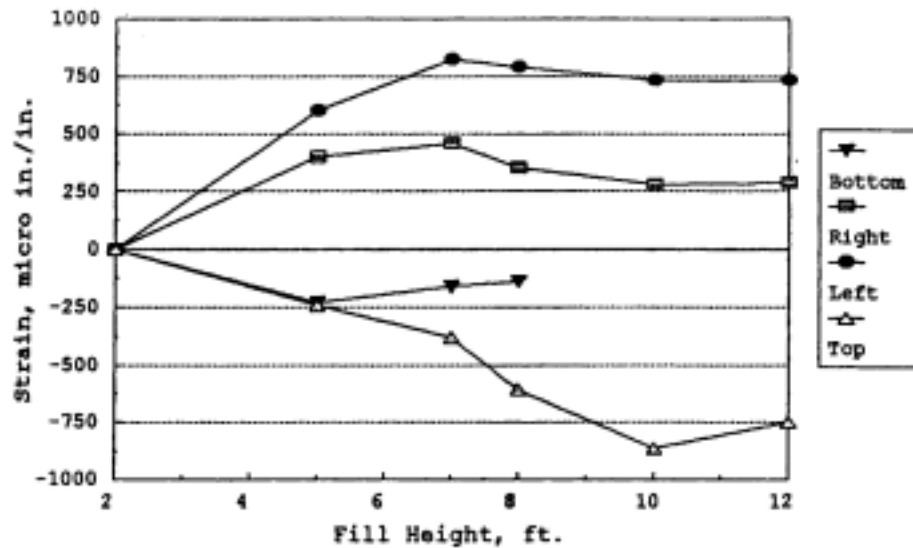
sections downstream such as at Sections 3 and 4. Also, Section 6 is located at the end of the downstream portion of the test specimen where the 8 gage steel section was located. Because of the additional stiffness in this region (due to the thicker steel walls), deformations for similar magnitudes of loads would be smaller.

Longitudinal and hoop strains present on the inner surface of the CMP at the peaks of the corrugations (see Figure 7.4) were recorded during the backfill process. Representative strain data from Sections 2, 3, 4 and 6 are presented in Figures 7.13 and 7.14. From Figure 7.13, it is apparent that very little strain was present in the longitudinal direction while significantly higher strains were acting in the hoop direction.

A comparison of the cross sectional deformation data and the strain data further explains the behavior of the CMP during backfilling. As shown in Figures 7.13b and 7.14, hoop strains on the sides of the pipe at mid-height (indicated by left and right) were positive indicating tension. Inward movements of the pipe walls, consistent with the deformation data presented earlier, would cause tensile strains on the corresponding inner surface. Conversely, hoop strains on the top of the pipe (indicated by top) were negative signifying compressive behavior. Outward movements of the walls at the top of the pipe, evident from the data introduced earlier, would cause compressive forces to develop on the inner surface. Also, a majority of the strain in these regions appeared to develop within the first 7 to 8 feet of

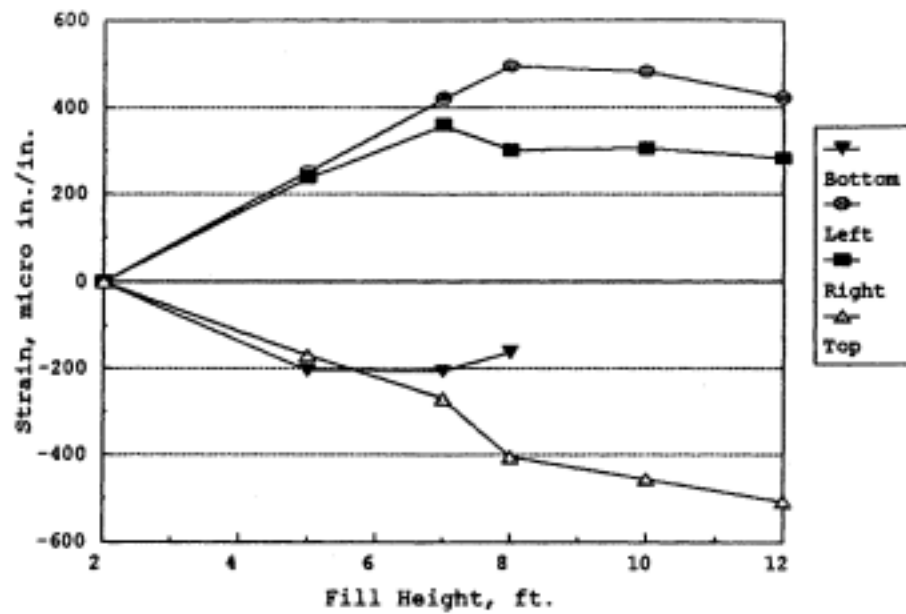


(a) Longitudinal strains

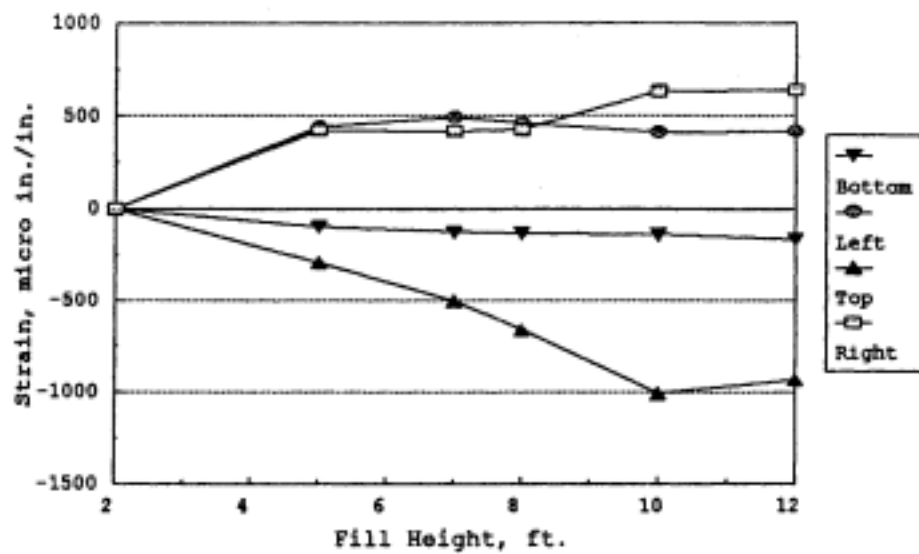


(b) Hoop strains

Figure 7.13 Backfill strain data: Section 3.

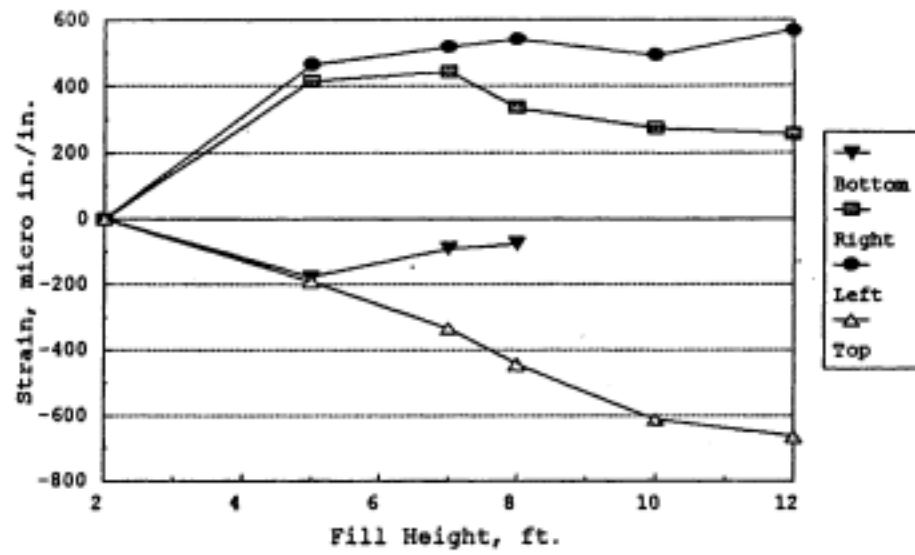


(a) Hoop strains - Section 2



(b) Hoop strains - Section 4

Figure 7.14 Backfill strain data.



(c) Hoop strains - Section 6

fill similar to the cross sectional deformations. The two sets of data - strains and deformations are indicating the same behavior.

Variations in the magnitudes of strain on the top and bottom, as well as the left and right sides of the pipe at certain sections were noticeably different. The variations between the top and bottom strains can be partially attributed to the fact that the bottom of the pipe was firmly setting on a compacted bed of soil and was essentially prevented from deforming vertically while the top of the CMP had no external constraints resisting deformations vertically. These boundary conditions may have forced all vertical deformations to take place in the upper regions of the pipe. Assuming this deformation pattern took place, the top of the CMP would have developed larger strains than the bottom which is consistent with the strain data. Variations in strain between the right and left sides of the pipe may be due to a number of things. The most obvious reason would be one side of the pipe deflected inward more than the other, resulting in different strains at the two locations.

Soil pressure cells placed within the soil backfill monitored the changes in pressure around the CMP. Lateral soil pressures at the mid-height of the CMP were measured with Cells 1 through 3 and Cells 6 through 8 as shown in Figure 7.6. Figure 7.15 shows the lateral soil pressure recorded at these locations versus the level of fill. As the level of fill increased, the

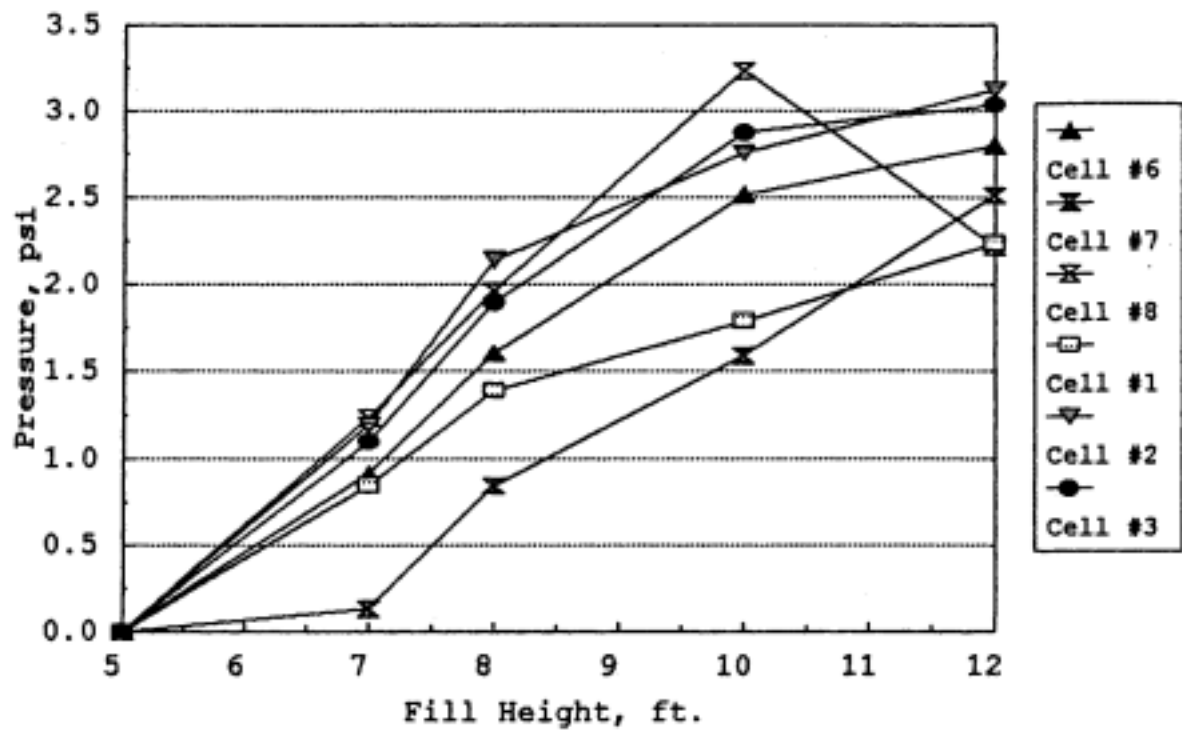


Figure 7.15 Backfill soil pressure cell data.

lateral pressures also increased. If a best fit line were drawn through the data it would extend from 0 psi pressure at the fill height of 5 feet to approximately 2.75 psi at the fill height of 12 feet. If the backfill responded along this ideal loading path, the lateral earth pressure coefficient (K) would be constant. Assuming a soil density of 120 pcf, the vertical stress is 5.83 psi or K is 0.5. However, the coefficient at different stages of the backfill is likely different because the soil-structure response was changing as the fill progressed upward. It was shown earlier that the walls of the CMP were moving inward from a fill height of 5 to 8 feet which would cause the adjacent soil mass to be in an active state. However, from a fill height of 8 to 12 feet insignificant movement of the CMP walls was recorded suggesting that the soil mass was at rest. Although the lateral earth pressure coefficient for an active case is lower than that of an at rest case, the plot shows a more rapid increase in pressure, and therefore a larger lateral earth pressure coefficient, from 5 to 8 feet of fill than from 8 to 12 feet of fill. The effects of the compaction equipment on the cells early in the backfill was probably more pronounced than later in the backfill which may explain the more rapid increase in pressure from a fill height of 5 to 8 feet.

7.10 Uplift Data

The loads applied during the uplift portion of the test were to simulate the pore pressure distribution resulting from steady state seepage beneath the pipe. A load ratio of 2 between the

load on the front lift straps and the back lift straps closely approximates this situation. Load cells were placed beneath the hydraulic cylinders and monitored with the DAS for accurate force measurement. A remote computer was linked to the DAS which allowed the data collection process to be computer controlled. This permitted recording all data practically simultaneously.

Before loads were applied, initial readings were read and recorded for each instrument. The first portion of the program continuously updated the forces being applied at each load point and quickly displayed this information. This information was constantly monitored and communicated to the individuals applying the force until the desired combination of loads was obtained. After obtaining the desired magnitude of uplift, applied loads, strains, and deformations were read and recorded. This sequence of events was repeated for several load increments until a 3 inch upward deflection occurred at the upstream end of the pipe at which time the test was terminated.

7.11 Uplift Results

Representative samples of data recorded during the uplift test are presented in this section. The same type of measurements recorded during the backfilling process were recorded during the uplift test. In addition, load cells placed beneath the hydraulic cylinders were monitored during the test, and vertical deflections along the top of the pipe were determined and recorded after each load increment.

The two load points were closely monitored to obtain the

desired combination of uplift. As noted previously, a ratio of 2 between the forces in the front straps (furthest upstream) and the back straps (furthest downstream) was intended to be maintained throughout the test. Figure 7.16 displays the loads that were applied at the different load increments. As indicated in the figure, the desired loading ratio was essentially maintained throughout the entire test.

Vertical deflections at seven locations (see Figure 7.7) along the top of the pipe were monitored throughout the test. The deflections at each section were plotted against the corresponding load increment as shown in Figure 7.17a. Very little movement was observed at Section d while no activity was observed at Sections e, f and g. It appears that some bending was occurring due to the interaction of the pipe and soil within certain regions of the system. The bending action of the pipe is better illustrated in Figure 7.17b. This plot presents a profile of the CMP during different stages (load increments) of the test. The specimen is undoubtedly undergoing bending, particularly in the region 15 to 30 feet. from the inlet. The presence of the steel load straps provided some support at the upstream end of the pipe and essentially limited excessive bending in the first 15 feet of the CMP.

As previously noted, longitudinal and hoop strains were measured on the inner surface at the top, bottom and sides of the pipe at the six sections shown in Figure 7.4. As expected, very noticeable changes in strain were observed as the CMP began to

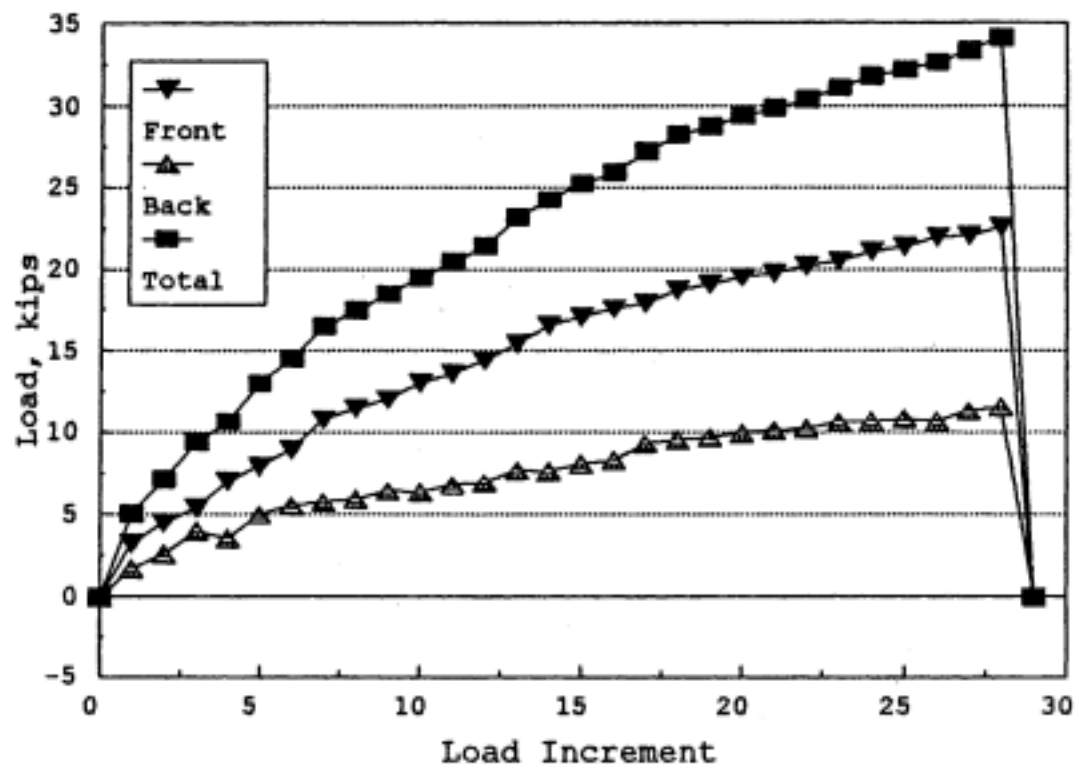
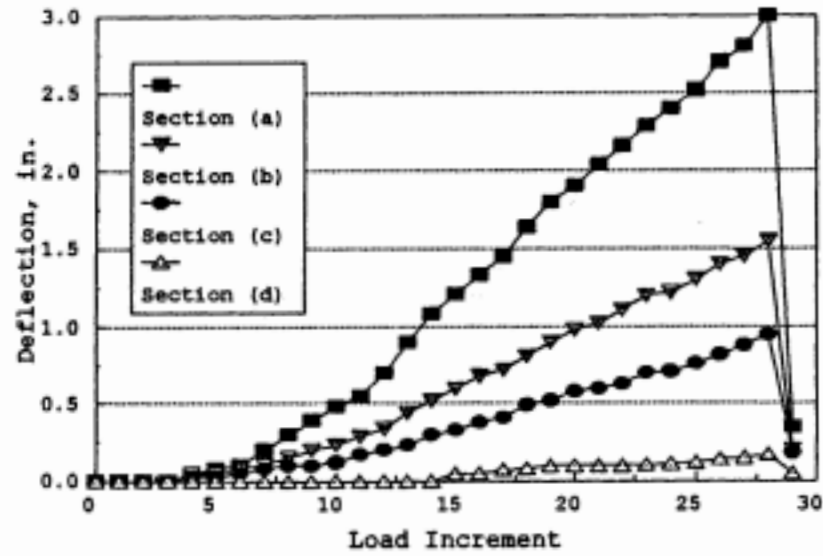
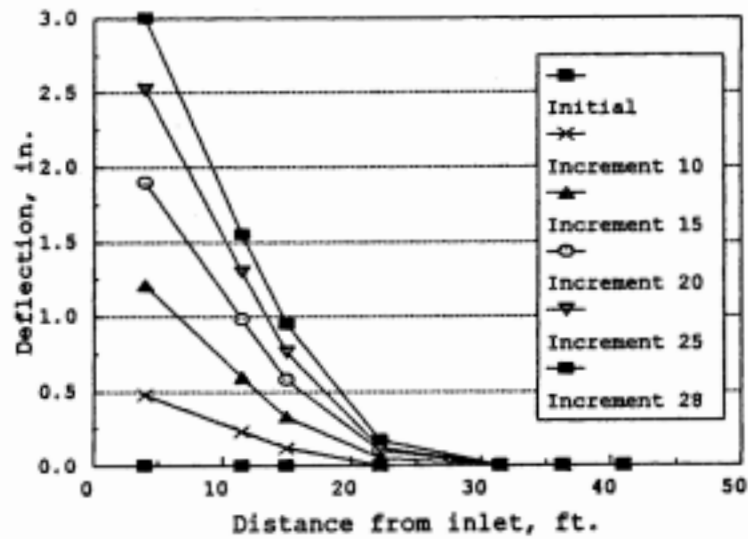


Figure 7.16 Uplift - loading sequence.



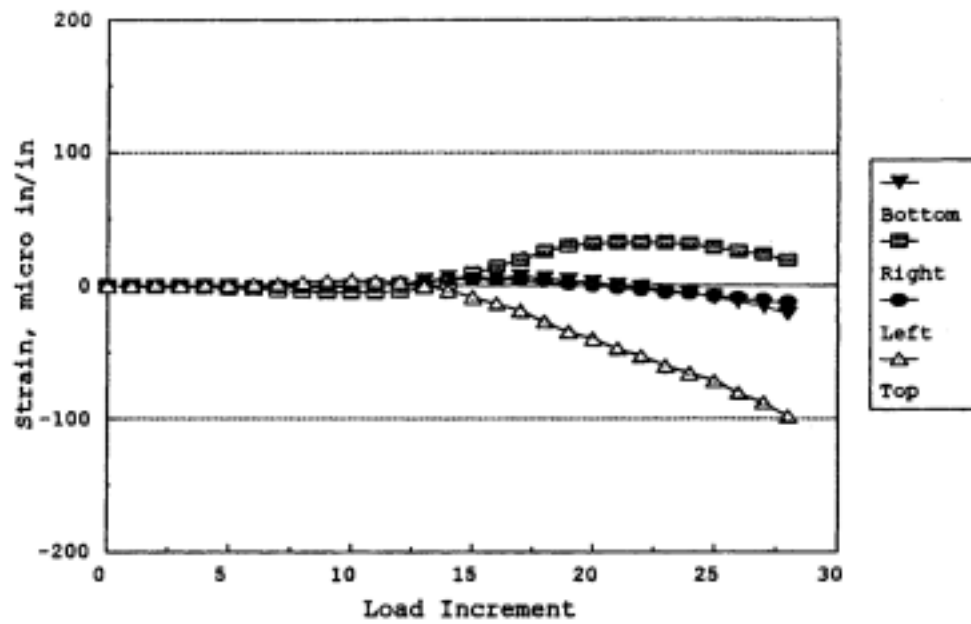
(a) Deflections at each section versus load increment



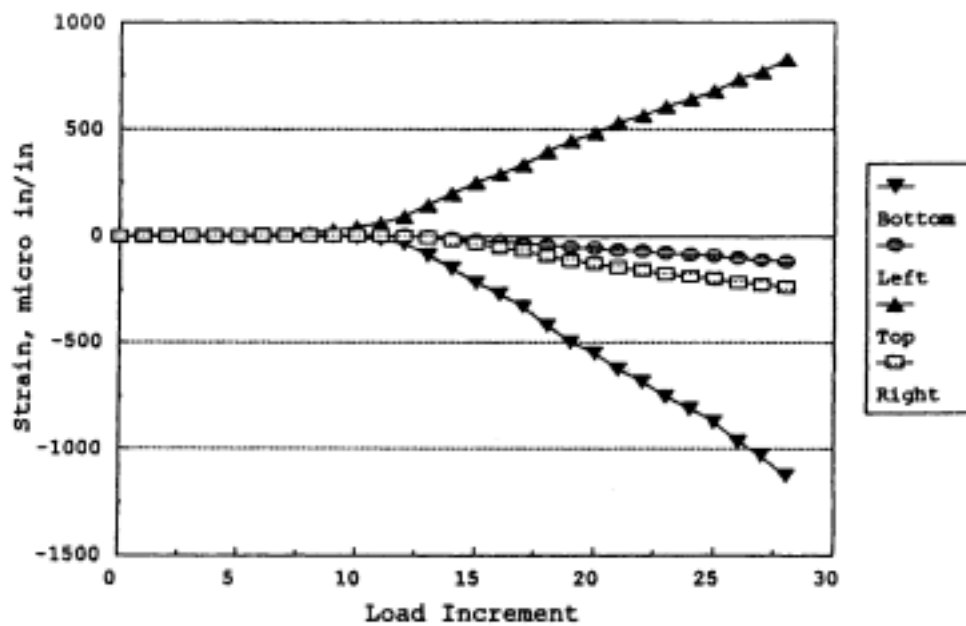
(b) Profile of deflected pipe at selected intervals during uplift

Figure 7.17 Vertical deflections along top of pipe during uplift test.

bend. Unlike the backfill data, the longitudinal strains were significantly larger than those in the hoop direction. This behavior can be observed when reviewing typical strain data taken from Section 3 and comparing the longitudinal and hoop strains (see Figure 7.18). Additional longitudinal strain data from Sections 1 and 4 are shown in Figure 7.19. The longitudinal strains on the sides of the pipe at mid-height (indicated by left and right) were very small relative to those at the top and bottom. This implies that the CMP's neutral axis remained near the mid-height of the pipe despite the addition of the soil to the system. Because the strain gages were placed on the inside of the pipe, tensile (positive) strains were measured on the top while compressive (negative) strains were recorded on the bottom. Top and bottom longitudinal strains at Section 1 (see Figure 7.19a) were relatively equal in magnitude throughout the entire test. However, moving further upstream to Section 3 where the entire pipe was covered with soil, the strain on the top was less than the corresponding strain on the bottom (see Figure 7.18b). Recall, the base of the pipe at this particular section was beginning to separate from the soil as was indicated by the deflection data discussed earlier (see Figure 7.17a; Section d). This separation along with the expanding action of the corrugations on the bottom of the pipe may have prevented the interlocking soil from providing any additional resistance to local deformations. In contrast, the top regions of the pipe were being compressed into the soil. The additional pressure

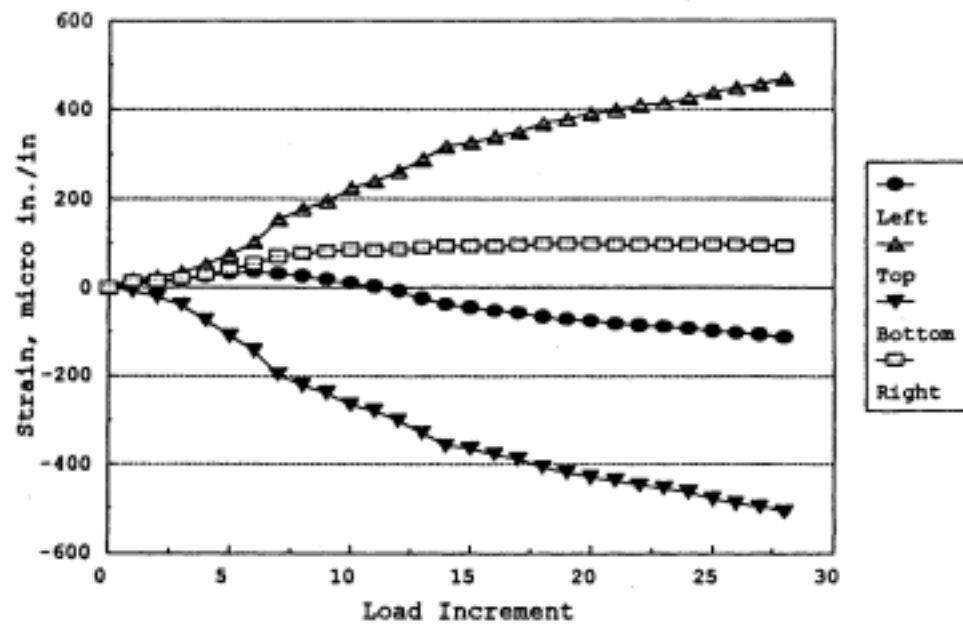


(a) Hoop strains versus load increment

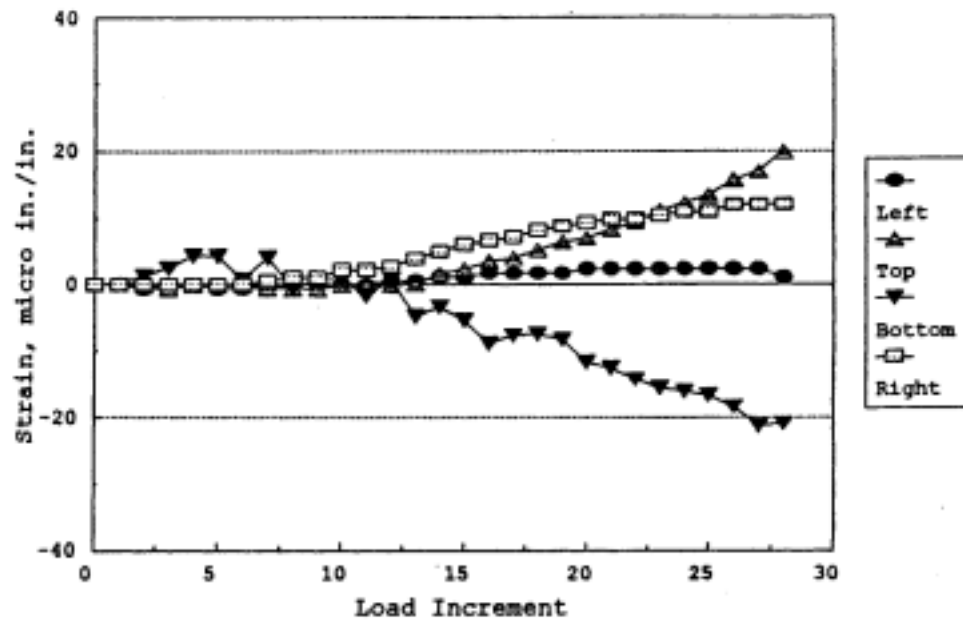


(b) Longitudinal strains versus load increment

Figure 7.18 Uplift strain data: Section 3.



(a) Longitudinal strains versus load increment - Section 1



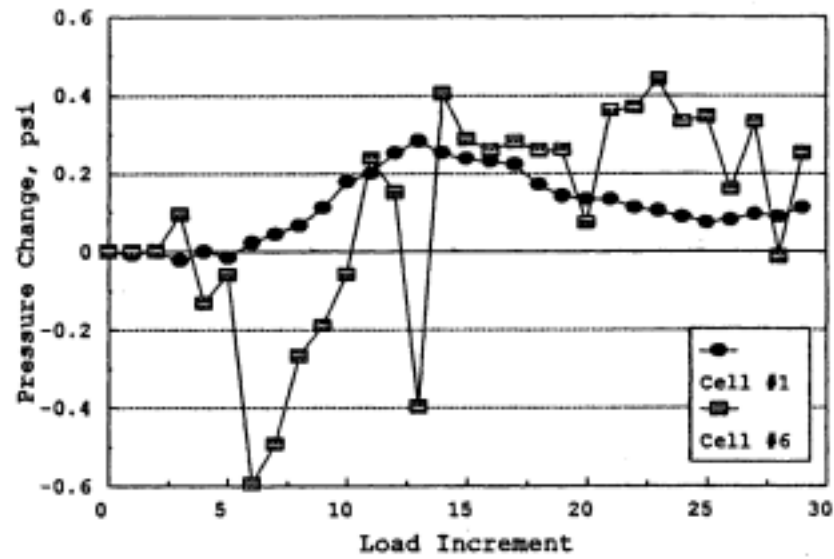
(b) Longitudinal strains versus load increment - Section 4

Figure 7.19 Uplift strain data: Sections 1 and 4.

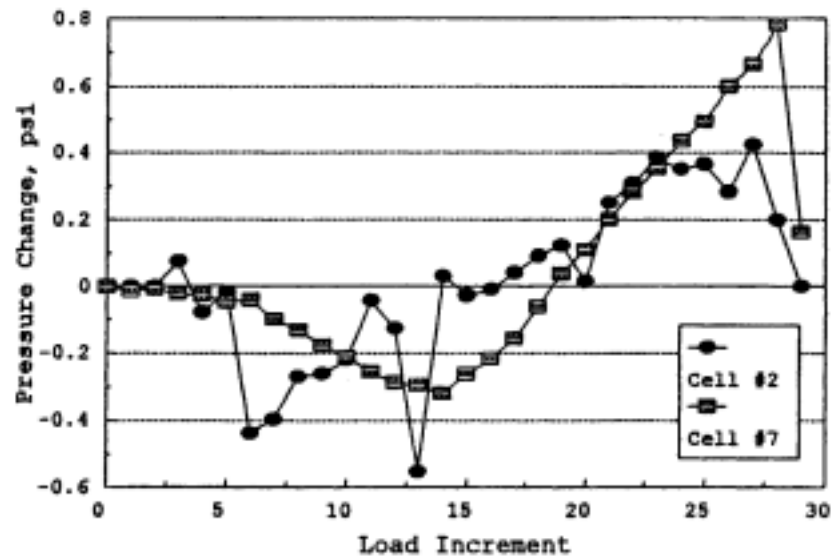
provided by the soil above was monitored with soil pressure cells located directly above the top of the pipe (see Figure 7.6). A more detailed discussion of the soil pressure cells is covered later in this report. The anticipated compressive action of the corrugations due to bending may have been partially restricted with the soil in the corrugations being confined by the additional pressure developed during uplift. The above discussion suggests that the top portion of the pipe may have gained additional stiffness from the interacting soil while the bottom portion of the pipe received little benefit from the soil.

Ten soil pressure cells were placed in different regions of the backfill (see Figure 7.6) for determining the portions of the surrounding soil that contributed to uplift resistance. At this time, interpretation of the soil data is limited to observations; and a more complete analysis is presently being developed to better understand the role of the surrounding soil.

The pressure cells placed at the mid-height of the pipe were positioned to measure the lateral pressure acting near the pipe's sides. Cells 1 through 3 were positioned on the left side of the pipe, looking downstream, at Sections 20 feet, 25 feet and 32 feet from the upstream end of the pipe. Cells 6 through 8 were located at the same sections but on the right side of the pipe. These six particular cells did not respond in a consistent manner. As shown in Figure 7.20a, Cell 1 detected an increase in pressure from load increment 5 to 13 but slowly decreased in pressure for the remainder of the test. Just 5 feet downstream



(a) Soil pressure changes at midheight - Section A

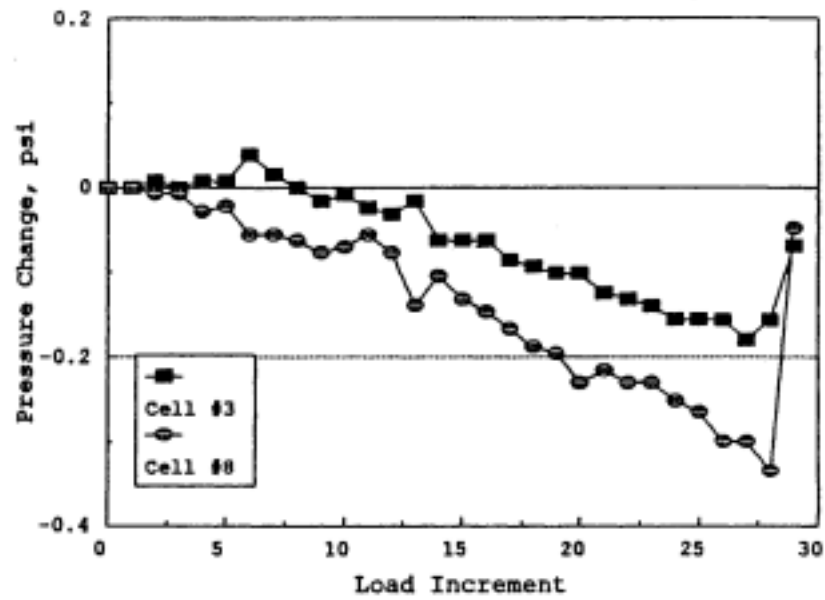


(b) Soil pressure changes at midheight - Section B

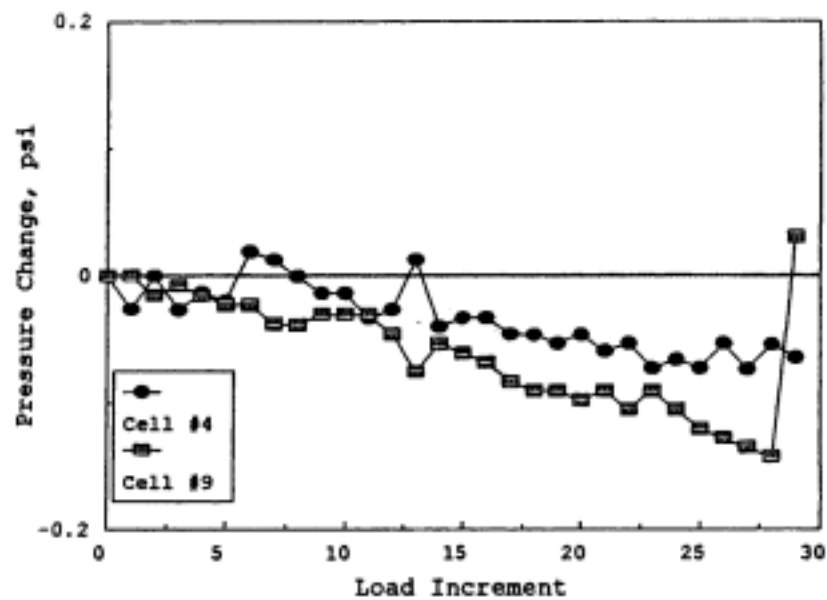
Figure 7.20 Pressures developed within soil during uplift test: Sections A and B.

on the other side of the pipe, Cell 7 showed a decrease in pressure from load increment 5 to 13 and then experienced a steady increase in pressure for the remainder of the test as shown in Figure 7.20b. Lateral movements of the pipe during uplift is one possible explanation for this response. If the CMP initially moved slightly to the left during uplift, Cell 1 would detect an increase in pressure while Cell 7 would experience a decrease in pressure. If later the pipe shifted its lateral motion to the right, the opposite behavior would occur; with pressure measured by Cell 1 decreasing while pressures measured by Cell 2 would increase. As shown in Figure 7.21a, Cells 3 and 8, located 32 feet from the upstream end, showed a steady decrease in pressure for the entire test. Pressure Cells 4 and 9 located at the same section but placed further up in the backfill experienced this same behavior as shown in Figure 7.21b. This particular section experienced little activity during the test; no uplift occurred and very small longitudinal strains were recorded.

Soil pressure Cells 5 and 10 placed 1 foot directly above the top of the pipe experienced consistent, expected results. At nearly the same time longitudinal strains were beginning to develop on top of the CMP at Section 3, Cell 5, located just 2 feet downstream of this section, began showing an increase in pressure as shown in Figure 7.22a. This pattern of increasing pressure continued for a short period until reaching a level of pressure of about 0.17 psi which was steadily maintained for the

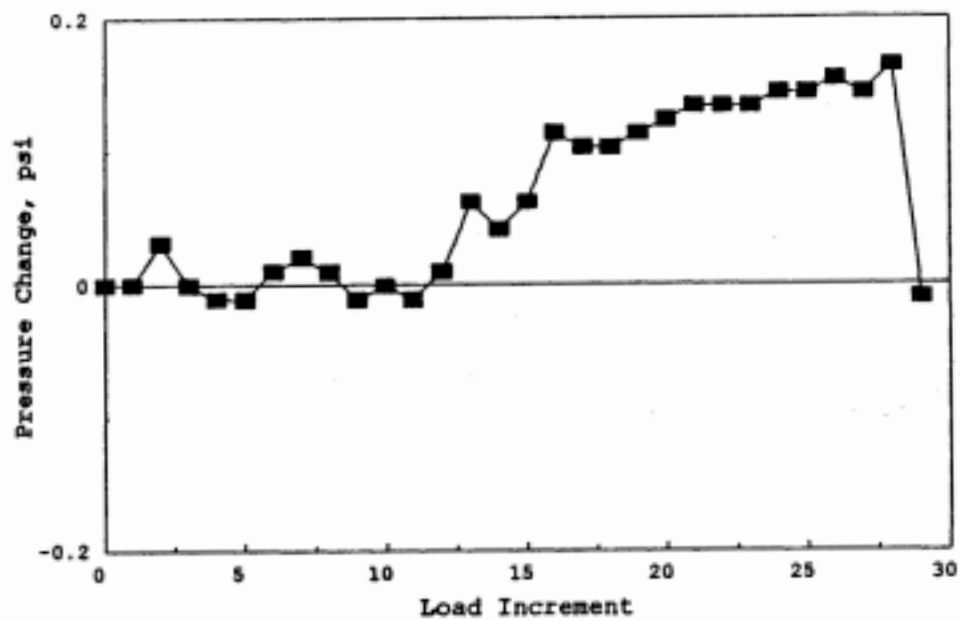


(a) Soil pressure changes at midheight

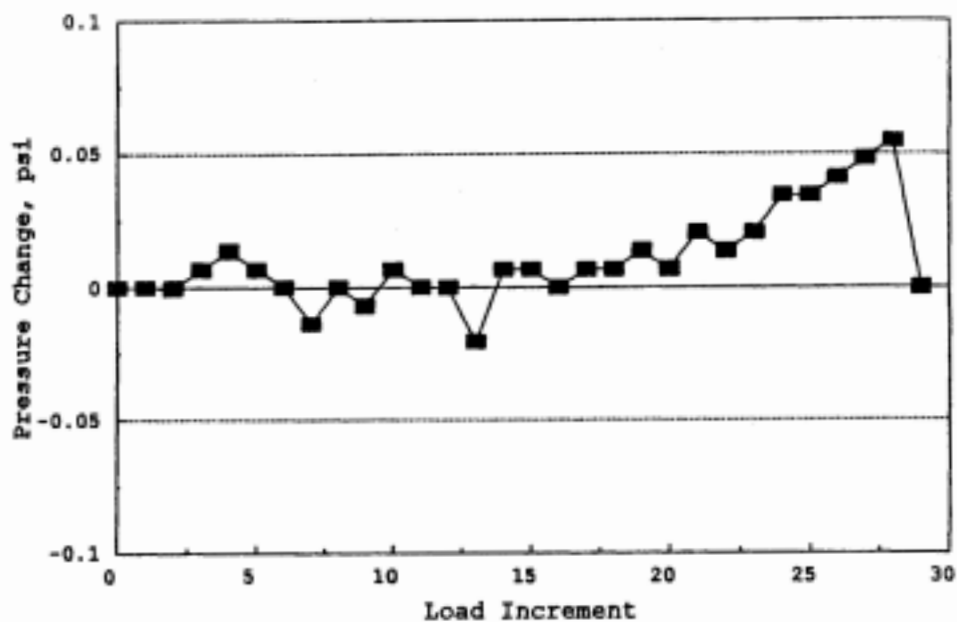


(b) Soil pressure changes in upper region

Figure 7.21 Pressures developed within soil during uplift test: Section C.



(a) Soil pressure changes above pipe - Section B

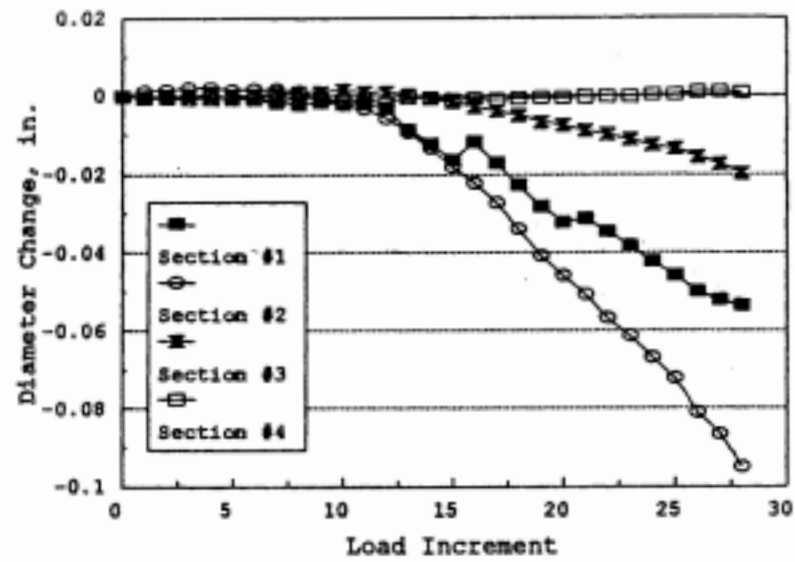


(b) Soil pressure changes above pipe - Section C

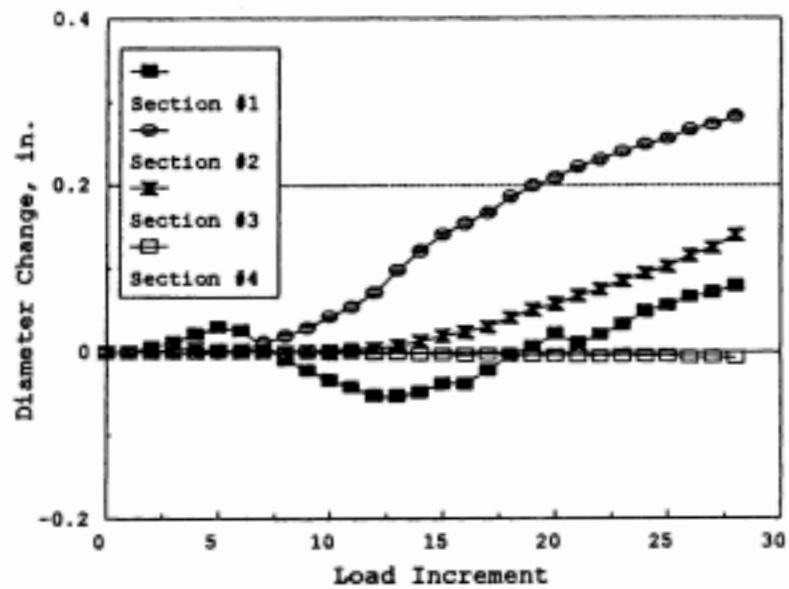
Figure 7.22 Pressures developed within soil above CMP during uplift test.

remainder of the test. The pipe deflection data indicates that the CMP at this particular section (see Figure 7.17a; Section d) began experiencing uplift at Load Increment 15 while pressure Cell 5 experienced an increase in pressure. These data suggest that, prior to uplift occurring, a slight build up of pressure occurred on top of the CMP. However, after uplift was initiated and the soil mass above was mobilized, the pressure leveled off and remained constant. Pressure Cell 10 which is located 7 feet downstream of Cell 5 experienced a continuous pressure increase as shown in Figure 7.22b; and deflection data shows that this region of the pipe did not experience uplift. The increasing pressure detected by this particular cell suggests the soil was in the pressure build up stage prior to uplift.

Changes in the pipes cross sectional shape were monitored as the CMP was subjected to the uplift. As shown in Figure 23, very little change was observed throughout the entire test. Sections 1, 2 and 3 were the only sections where deformations were detected. The sides of the pipe moved slightly inward while the top portion of the pipe deflected upward. The opposite behavior is normally associated with bending action but the load straps may have restrained the sides of the CMP during uplift causing this response. Recall that the lateral pressures acting at the pipes mid-height were greater than the corresponding pressures on top of the CMP. Thus, very little force was necessary to initiate more inward movement of the sides of the pipe.



(a) Horizontal diameter changes.



(b) Vertical diameter changes.

Figure 7.23 Cross sectional deformations during uplift test.

7.12 Methods of Analysis

Note many of the parameters discussed in this document have been plotted against the load increment. This approach was used because the soil-CMP system is highly statically indeterminate and conventional methods of analysis were not suitable for computing the forces at different sections of the pipe. At the present time, a finite element method of analysis is being developed to determine the loads and forces in the pipe during uplift. Data obtained from the experiment are being used to calibrate the finite element model. After this task is completed, a more rational comparison of all relevant parameters at a particular section can be made.

8. CONCLUSIONS

The following conclusions were formulated from the responses to the questionnaire and from the results obtained from the laboratory and field tests. In reviewing the conclusions from the field test, one should remember these are based on one test: one fill depth, one type of soil, one CMP size etc. Generalizing these conclusions for other situations in most cases would not be valid.

1. Although only nine agencies responding to the questionnaire had had CMP uplift problems in the past five years, 26 of the 52 respondents use some type of uplift restraint. Eighteen of the 26 agencies developed the restraints in response to earlier problems.
2. Of those agencies that provided data on the hold-down restraint forces, there was a wide variation.
3. Three CMP's (ISU1), (ISU2), and (ISU3) were loaded to failure to determine experimental values for the "stiffness" EI, yield moments, and ultimate moments. Values for these quantities have been tabulated in Table 6.3, 6.4 and 6.5 respectively.
4. For determining "stiffness" EI, yield moments, and ultimate moments for other CMP's (different diameter, gages, corrugation geometry etc.) theoretical relationships for these quantities were derived. The relationships for "stiffness" EI (Equation 45) provides

conservative estimates. Except for Specimen ISU3, there is good agreement between theoretical and experimental "stiffness" EI's. The relationship for yield moments (Equation 13) provides non-conservative yield moments. Primarily the difference is the result of variations in the steel yield strengths. The theoretical formula for ultimate moment capacity (Equation 26) provides values that are in good agreement with the experimental values.

5. Changes in the pipe's cross sectional shape are evident during backfilling as a result of the lateral soil pressure acting on the sides of the CMP. A majority of the deformations take place when backfilling the middle half of the pipe height.
6. The primary strains developed during backfilling are those in the hoop direction; a direct result of the cross sectional deformations that occur during backfilling. The longitudinal strains during backfilling were insignificant in comparison to the hoop strains.
7. The hoop strains developed on top of the pipe during backfilling are greater than those on the bottom as the bottom of the pipe is firmly set in a compacted saddle and is prevented from deforming while the upper portion of the pipe is free of any external restraints during the early stages of the backfill.

8. The soil-structure interaction developed during uplift with minimum cover requirements (2 feet) is significant enough to cause longitudinal bending of the CMP.
9. Longitudinal strains are the primary strains during uplift. Hoop strains are insignificant in comparison to the longitudinal strains during uplift.
10. In regions where the soil covers the entire pipe, the top regions receive additional stiffness from the interacting soil during uplift. On the other hand, the bottom of the pipe is separated from the soil and receives no benefit from the surrounding soil. This behavior results in smaller strains being developed on top of the pipe than on the bottom.
11. Cross sectional deformations during uplift are very small in comparison to the deformations experienced during backfilling.

9. RECOMMENDED RESEARCH

As noted in the proposal, completion of this phase of the investigation is one of the necessary steps in the development of a design methodology and design standards for CMP tiedowns.

As was previously noted, additional field tests are required to obtain an adequate knowledge of the soil-CMP interaction. Using data from the additional field tests coupled with the results from this phase of the study (Phase I) and the pore pressure analysis from the initial phase of this investigation, a finite element model (FEM) can be developed and calibrated. With the theoretical FEM results and experimental data, the desired design methodology and design standards can be developed.

10. ACKNOWLEDGEMENTS

The study presented in this report was conducted by the Engineering Research Institute of Iowa State University. The research was sponsored by the Iowa Department of Transportation and the Highway Research Board under Research Project HR-332.

The authors wish to thank various engineers from the Iowa Department of Transportation, especially Darrel D. Coy for his support, encouragement, and counseling.

Appreciation is also extended to Robert L. Meinzer of Contech Construction Products, Inc., Topeka, Kansas whose company donated the numerous sections of corrugated metal pipe used in the various tests. The assistance of Construct, Inc., Ames, Iowa in excavating the trench for the field test is also gratefully acknowledged.

Special thanks are accorded the following undergraduate students for their assistance in various aspects of the project: Jay A. Buroker, Theresa A. Connor, Thomas S. Duff, Scott E. Foster, Jim A. Jahnke, and Brian C. Schaller.

11. REFERENCES

Abdel-Sayed, George. "Stability of Flexible Conduits Embedded in Soil," *Canadian Journal of Civil Engineering*, Vol. 5, 1978, pp. 324-366.

Ahlvin, R.G. "Effects of Heavy-Load Traffic on a Shallow-Buried Flexible Pipe," *Proceedings, Highway Research Board*, Vol. 39, 1960, pp. 372-384.

American Iron and Steel Institute, Handbook of Steel Drainage & Highway Construction Products, AISI, New York, NY, 1st Edition, 1967.

American Society of Testing and Materials, Standard Test Method of Tension Testing of Metallic Materials (ASTM E8-90a), Annual Book of ASTM Standards, Vol. 3.01, Philadelphia, PA, 1991.

Armco Drainage and Metal Products. "Handbook of Drainage and Construction Products," Armco, Middletown, Ohio, 1955.

Austin, T. Al, Lohnes, Robert A., Klaiber, F. Wayne. "Investigation of Uplift Failures in Flexible Pipe Culverts," Final Report to the Iowa Department of Transportation, March, 1990.

Austin, T. Al, Lohnes, Robert A., Klaiber, F. Wayne. "Investigation of Uplift Failures in Flexible Pipe Culverts," Abridgment of Final Report to the Iowa Department of Transportation, October, 1990.

Bakht, Baidar. Structures in Distress, Chapter 10, book in progress.

Brown, C.B., Green, D.R., Pawsey, S. "Flexible Culverts Under High Fills," *Journal of the Structural Division, ASCE*, Vol. 94, ST4, April, 1968, pp. 905-917.

Chelapati, C.V., and Allgood, J.R. "Buckling of Cylinders in a Confining Medium," *Highway Research Record No. 413*, Highway Research Board, Washington, D.C., 1972, pp. 77-88.

Duncan, J.M., Byrne, P., Wong, K.S., and Mabry, P. "Strength, Stress-Strain, and Bulk Modulus Parameters for Finite Element Analysis of Stresses and Movements in Soil Masses," University of California at Berkeley, Rept. UCB/GT/80-01, August, 1980.

Duncan, J.M. "Soil Culvert Interaction Method for Design of Metal Culverts," *Transportation Research Record 678*, 1978, pp. 53-59.

Duncan, J.M. "Behavior and Design of Long-Span Metal Culverts," Journal of the Geotechnical Engineering Division, ASCE, Vol. 105, No. GT3, March, 1979, pp. 319-418.

Edgerton, Roy C. "Culvert Inlet Failures-A Case History," Highway Research Board Bulletin 286, 1960, pp. 13-21.

Katona, M.G., et. al. "CANDE-A Modern Approach for Structural Design and Analysis of Buried Culverts," FHWA-RD-77-5, October, 1976.

Kay, J.N. and Flint, R.C.L. "Heavy Vehicle Loading of Arch Structures of Corrugated Metal and Soil," Transportation Research Record 878, 1982, pp. 34-37.

Kennedy, John, Laba, Jan T., Shaheen, H. "Reinforced Soil-Metal Structures," Journal of Structural Engineering, ASCE, Vol. 114, June, 1988, pp. 1372-1389.

Kennedy, John, and Laba, Jan T. "Suggested Improvements in Designing Soil-Steel Structures," Transportation Research Record 1231, 1989, pp. 96-104.

Krizek, Raymond J., Parmelee, Richard A., Kay, Neil J., Elnaggar, Hameed A. "Structural Analysis and Design of Pipe Culverts," National Cooperative Highway Research Program Report 116, 1971.

Lane, William W. "Comparative Studies on Corrugated Metal Culvert Pipes," Report No. EES-236, Engineering Experiment Station, Ohio State University, February, 1965.

Lefebvre, G., Laliberte, M., Lefebvre, L.M., Lafleur, J., and Fisher, C.L. "Measurement of Soil Arching Above a Large Diameter Flexible Culvert," Canadian Geotechnical Journal, Vol. 13, No. 1, Feb., 1976, pp. 58-71.

Luscher, Ulrich. "Buckling of Soil-Surrounded Tubes," Journal of the Soil Mechanics and Foundations Division, ASCE, Vol. 92, No. SM6, Proc. Paper 4990, Nov., 1966, pp. 211-228.

Marston, Anson. "The Theory of External Loads on Closed Conduits," Bulletin No. 96, 1930, Iowa Engineering Experimental Station, Ames, IA, pp. 5-8.

Mayberry, Earle W. and Goodman, Mark A. "Performance of Yielding Seam Structural Plate Pipe Culvert," Transportation Research Record 1231, 1989, pp. 36-48.

McVay, M.C. and Selig, E.T. "Performance and Analysis of a Long-Span Culvert," Transportation Research Record No. 878, January, 1982, pp. 23-29.

McVay, M. and Papadopoulos, P. "Long-Term Behavior of Buried Large-Span Culverts," *Journal of Geotechnical Engineering, ASCE*, Vol. 114, No. 3, April, 1986, pp. 424-440.

Meyerhof, G.G., and Baikie, L.D. "Strength of Steel Culvert Sheets Bearing Against Compacted Sand Backfill," presented at the 42nd Highway Research Board Meeting, Washington, D.C., January 9, 1963.

Moser, A.P. Buried Pipe Design, McGraw-Hill, New York, 1990, 219 pp.

Nielson, F. Dwayne and Statish, N.D. "Design of Circular Soil-Culvert Systems," *Highway Research Record*, No. 413, 1972, pp. 67-76.

Nielson, F. Dwayne. "Experimental Studies in Soil-Culvert Interaction," *Highway Research Record*, No. 413, 1972, pp. 30-44.

Potter, J.C. and Ulery, H.H. Jr. "Heavy-Load Traffic Tests for Minimum Pipe Cover," *Transportation Research Record* 1231, 1989, pp. 56-69.

Poulos, Harry G. "Analysis of Longitudinal Behavior of Buried Pipes," *Proceedings of the Conference on Analysis and Design in Geotechnical Engineering, ASCE*, June, 1974, pp. 199-223.

Selig, E.T. "Instrumentation of Large Buried Culverts," *ASTM Symposium on Performance Criteria and Monitoring for Geotechnical Construction, American Society for Testing and Materials*, June, 1974.

Selig, E.T., Abel, J.F., Kulhawy, F.H., and Falby, W.E. "Long-Span Buried Structure Design and Construction," *Journal of the Geotechnical Engineering Division, ASCE*, Vol. 104, No. GT7, Proc. Paper 13865, July, 1978, pp. 953-966.

Selig, E.T., Loackhart, C.W. and Lautensleger, R.W. "Measured Performance of Newtown Creek Culvert," *Journal of the Geotechnical Engineering Division, ASCE*, September, 1979, pp. 1067-1087.

Spangler, M.G. "The Structural Design of Flexible Pipe Culverts," *Engineering Experiment Station, Iowa State University, Bulletin* 153, 1941.

Spangler, M.G. Soil Engineering, The International Textbook Company, Scranton, 1st Edition, 1951.

Spangler, M.G. and Handy, R.L. Soil Engineering, Harper and Row, New York, NY, 4th Edition, 1982.

Spannagel, D.W., Davis, R.E. and Bacher, A.E. "Effects of Methods A and B Backfill on Flexible Culverts Under High Fills," Transportation Research Record No. 510, 1974.

Trautmann, Charles H., O'Rourke, Thomas D., Kulhawy, Fred H. "Uplift Force-Displacement Response of Buried Pipe," Journal of Geotechnical Engineering, ASCE, Vol. 111, No. 9, September, 1985, pp. 1061-1076.

Valentine, H.E. "Structural Performance and Load Reaction Patterns of Flexible Aluminum Culvert," Highway Research Board, No. 56, 1964, pp. 47-70.

Watkins, R.K. and Spangler, M.G. "Some Characteristics of the Modulus of Passive Resistance of Soil: A Study in Similitude," Proceedings, Highway Research Board, 1958, Vol. 37, p. 576.

Watkins, R.K. "Failure Conditions of Flexible Culverts Embedded in Soil," Highway Research Board Proceedings, Vol. 39, 1960, pp. 361-371.

Watkins, R.K. and Moser, A.P. "Response of Corrugated Steel Pipe to External Soil Pressures," Highway Research Record No. 373, Highway Research Board, 1971, pp. 86-112.

White, H.L., and Layer, J.P. "The Corrugated Metal Conduit as Compression Ring," Proceedings, Highway Research Board, Vol. 39, 1960, pp. 389-397.

Young, D.F. and Murphy, Glenn. "Similarity Requirements for Underground Structures," Proceedings of the Symposium on Soil-Structure Interaction, University of Arizona, Tucson, 1964.

Young, W.C. Roark's Formulas for Stress and Strain, McGraw-Hill Book Company, New York, 6th Edition, 1989.

APPENDIX A

Method to Account for Non-Uniform Loading of CMP

Method to Account for Non-Uniform Loading of CMP

Vertical deflections (measured on the bottom of the CMP at the mid-span and quarter-span points) are used to develop a curve which approximates the deflected shape of the CMP under load as shown in Figure A.1. After observing photographs of each CMP in flexure, it is assumed that curvature on the bottom of the CMP profile between the supports and quarter-span points is minimal. Thus, the profile is approximated as linear in this region to simplify the computations. The slope of the bottom of the CMP between the quarter-span points is then quantified as the vertical deflection at the quarter-span divided by one-fourth of the CMP length. To model the deflected shape of each interior quarter-span, an exponential curve is fit through two deflections at mid-span and at each quarter-span point. The slope values are known at each quarter-span point based on assumptions stated above, and the slope at mid-span is assumed to be zero. Thus, the actual exponent of the curve for each side of the span will be calculated from the deflections and the quarter-point slope. The curve equation is shown:

$$y = \omega x^i \quad (1)$$

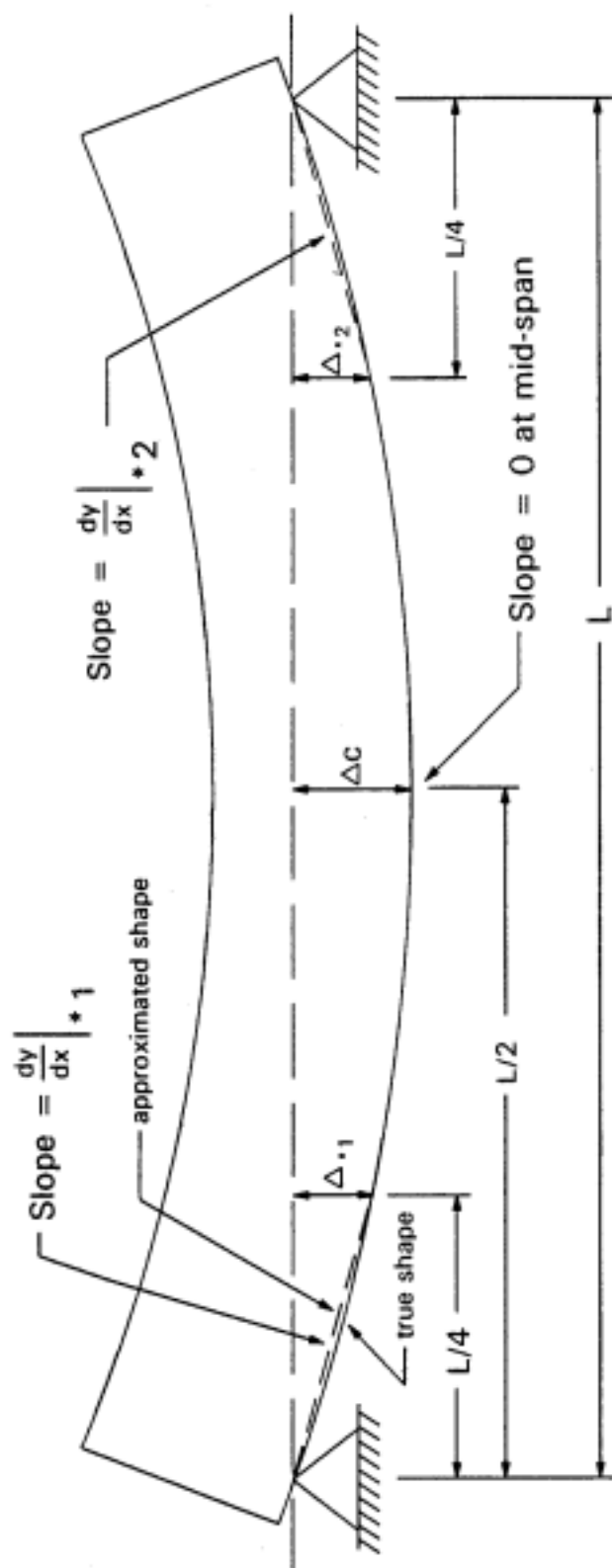


Figure A.1 Assumptions used to model CMP deflected shape under load.

Slope of the curve is calculated as:

$$\frac{dy}{dx} = \omega i x^{i-1} \quad (2)$$

The coefficient ω and exponent i are constant values for each half of the span. To solve for i , Equation 1 and Equation 2 are combined, eliminating ω . The exponent, i , can be calculated as:

$$i = \frac{x}{y} \frac{dy}{dx} \quad (3)$$

Because i is constant along the entire quarter-span curve, it can be evaluated using any value of x and y on the curve. It is assumed that the end of the curve with zero slope has coordinates of $x=0$ and $y=0$. Division by zero prohibits solving for i at this end of the curve. The coordinates at the other end of the curve are designated as $x=x_{qp}$ and $y=y_{qp}$. Solving for i :

$$i = \frac{x_{qp}}{y_{qp}} \frac{dy}{dx} \quad (4)$$

The coordinates x_{qp} and y_{qp} are substituted into Equation 1 to create an expression for ω :

$$\omega = \frac{y_{QP}}{x_{QP}^i}$$

Expressions for ω and i are substituted into Equation 1:

$$y = \frac{y_{QP}}{\frac{\frac{dy}{dx}(\frac{x_{QP}}{y_{QP}})}{x_{QP}}} x \frac{dy}{dx}(\frac{x_{QP}}{y_{QP}}) \quad (6)$$

Simplifying:

$$y = y_{QP} \left(\frac{x}{x_{QP}} \right) \frac{dy}{dx}(\frac{x_{QP}}{y_{QP}}) \quad (7)$$

Equation 7 is the general expression for the curve which is used to model the deflected interior quarter-spans.

To apply measured vertical deflections (shown in Figure A.1) to the expression for a deflected curve, the following relationships are used:

$$(\text{"*1" half of span}) \quad y_{QP} = y_{.1} - \Delta_c - \Delta_{.1} \quad (8)$$

$$(\text{"*2" half of span}) \quad y_{QP} = y_{.2} - \Delta_c - \Delta_{.2}$$

$$X_{OP} = X_{.1} = X_{.2} = \frac{L}{4} \quad (10)$$

$$\frac{dy}{dx} = \frac{\Delta_{.1}}{\frac{L}{4}} = \frac{4\Delta_{.1}}{L} \quad (11)$$

$$\frac{dy}{dx} = \frac{4\Delta_{.2}}{L} \quad (12)$$

Substituting equations 11 and 12 into equation 7, the following equations allow for calculation of y over each half of the span; y is thus denoted as y_{hs1} and y_{hs2} .

$$y_{hs1} = (\Delta_c - \Delta_{.1}) \left(\frac{4X}{L} \right)^{\left(\frac{\Delta_{.1}}{\Delta_c - \Delta_{.1}} \right)} \quad (13)$$

$$y_{hs2} = (\Delta_c - \Delta_{.2}) \left(\frac{4X}{L} \right)^{\left(\frac{\Delta_{.2}}{\Delta_c - \Delta_{.2}} \right)} \quad (14)$$

The following relationships equate the x value (measured from the "*1" end of the CMP) to a "local" x value in each quarter-span.

Quarter-span 1:

$$x_{Q1} = x \quad (15)$$

Quarter-span 2:

$$x_{Q2} = \frac{L}{2} - x \quad (16)$$

Quarter-span 3:

$$x_{Q3} = x - \frac{L}{2} \quad (17)$$

Quarter-span 4:

$$x_{Q4} = L - x \quad (18)$$

The following equations will allow the deflections in each quarter-span to be computed as a function of x (measured from the east end).

Quarter-span 1:

$$\Delta = \frac{4\Delta_{s1} x}{L} \quad (19)$$

Quarter-span 2:

$$\Delta = \Delta_{s1} + (\Delta_c - \Delta_{s1}) \left(2 - \left(\frac{4}{L} \right) x \right)^{\left(\frac{\Delta_{s1}}{\Delta_c - \Delta_{s1}} \right)} \quad (20)$$

Quarter-span 3:

$$\Delta = \Delta_c - (\Delta_c - \Delta_{.2}) \left(\left(\frac{4}{L} \right) X - 2 \right)^{\left(\frac{\Delta_{.2}}{\Delta_c - \Delta_{.2}} \right)} \quad (21)$$

Quarter-span 4:

$$\Delta = \frac{4\Delta_{.1}(L-X)}{L} \quad (22)$$

With general expressions to calculate deflections at any point along the bottom of the CMP, the deflections are added to the measured depth of water in the CMP to determine the actual water depth at any point. The water in the CMP is divided into longitudinal sections (2 in long). The area, A, of each slice of water can be determined by relating the area of a circle sector to its radial dimension (see Figure A.2). This relationship is shown below.

$$A = \frac{\pi}{2} r^2 - \frac{a}{2} \left(r^2 - \frac{a^2}{4} \right)^{\frac{1}{2}} - r^2 \sin^{-1} \left(\frac{a}{2r} \right) \quad (23)$$

where:

- A = area of sector
- r = radius of circle
- a = distance from center of circle to line defining sector (assuming that a is less than r)

The sector area is multiplied by the slice width and the unit weight of water to obtain the weight of the slice. With each

slice weight and the weight from the uniform load on each slice, end reactions are calculated for the CMP. A shear diagram is developed for the entire CMP as shown in Figure A.3. By summing the area under one half of the shear diagram, the mid-span moment on the CMP is estimated for each load step during the tests. A further refinement used to calculate revised moment values involves calculation of the moment caused by the diaphragms rotating inward as the CMP deflects. This is estimated with expressions which are shown here:

$$M_{.1} = \frac{WD \sin(\tan^{-1}(\frac{4\Delta_{.1}}{L}))}{2} \quad (24)$$

$$M_{.2} = \frac{WD \sin(\tan^{-1}(\frac{4\Delta_{.2}}{L}))}{2} \quad (25)$$

where:

- $M_{.1}, M_{.2}$ = additional moment caused by weight of diaphragm
- W = weight of diaphragm
- D = diameter of diaphragm
- L = effective length of CMP between supports
- $\Delta_{.1}, \Delta_{.2}$ = deflections of CMP at quarter-span points

The revised mid-span moment is calculated based on uniform sand loading and non-uniform water loading as discussed in this appendix. The moments due to tilting of both diaphragms are then added to arrive at a final corrected mid-span moment

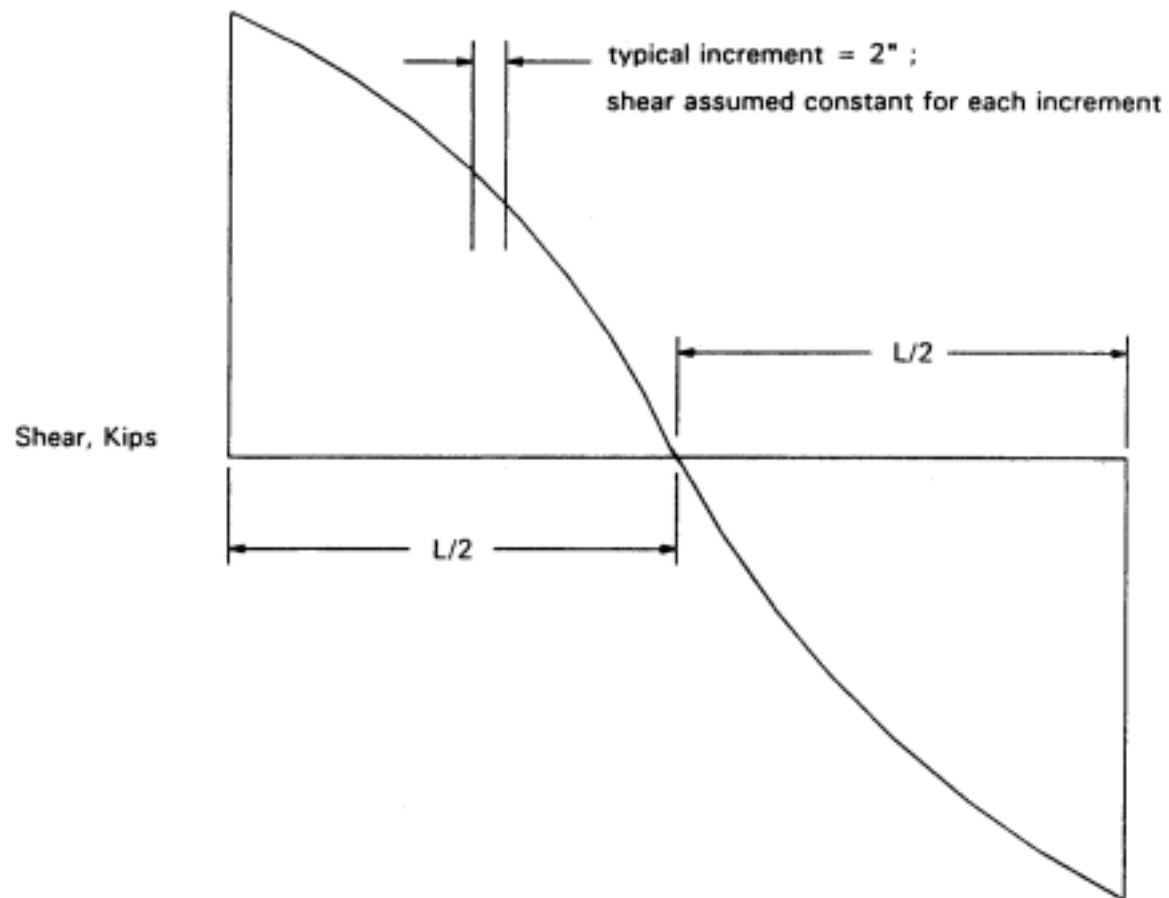


Figure A.3 Shear diagram for CMP specimens.

for each load stage during each flexural test.